Lancaster University

Distinguishing between Direct and Parametric Driving in Nanomechanics using a Vibrating CNT.

by

Sam Dicker, MPhys.

This thesis is submitted in partial fulfilment of the requirements for the degree of Doctor of Philosophy

in the

Faculty of Science and Technology
Department of Physics

November 26, 2025

Abstract

Distinguishing between Direct and Parametric Driving in Nanomechanics using a Vibrating Carbon Nanotube

Sam Dicker

Carbon nanotubes (CNTs) were discovered in 1952 by L. V. Radushkevich and V.M. Lukyanovich. CNTs have extraordinary mechanical properties being incredibly stiff but lightweight having a tensile strength greater than that of steel. Their electronic properties are also extraordinary allowing measurements in the quantum regime such as quantum blockade and single electron transistors (SETs). CNTs have high quality factors which when paired with their electronic and mechanical properties allows us to view CNT motion in the quantum regime. This can be used for detecting miniscule forces on the CNT possibly allowing the CNT to be used for magnetic resonance force microscopy. CNT motion is usually detected by looking at the change in current through a CNT on resonance, known as the rectification technique. The CNT is prone to unexpected resonances due to parametric motion which can obscure actual harmonics of the CNT, which cannot be differentiated using the rectification technique. In this thesis we show a new technique using a CNT device as an up-conversion RF mixer, which is shown to be able to distinguish between parametrically and directly driven motion. We do this by looking for signals at half the drive frequency which we are able to do using the time dependence on this new mixer technique. We show that the suspected parametric motion in the CNT turns on at a drive power of ~ -34 dBm and the signal peak exponentially increases with drive power which agrees with theory on parametric motion. We also show that the directly driven motion follows a linear dependence with drive power. We show that not only is this technique able to tell the difference between parametric and directly driven motion, but is also far more sensitive to CNT motion than the rectification technique. We were able to identify the other resonances seen around the first harmonic of the CNT, but we were unable to identify all harmonics around the 2nd harmonic of the CNT.

Acknowledgements

All of this work wouldn't have been possible without the help and support of those around me. I would like to thank my supervisor, Prof Edward Laird for offering me the opportunity to undertake this PhD at Lancaster university, and for constantly providing me with support for any questions I might have had. Having come from doing a master's in astrophysics, his knowledge and inspiration helped me through CNT mechanics, cleanroom fabrication, operating and maintaining a dilution refrigerator, and parametric oscillators.

I would also like to thank Patrick, who without our non-official official weekly Tuesday question sessions, would have left me working on incorrect theories. I can't thank him enough for his support in all lab-related issues, CNT theory, and cleanroom work especially when diagnosing the EBL who without him, I wouldn't have noticed the alignment coordinates matching the marker coordinates which enabled us to fabricate our entire device in house. A huge thank to Deepanjan and George whose friendship was a constant source of encouragement especially on those days when nothing seems to be working. I will always remember and cherish working with you two. Thanks to Matt, Niam, and Flo for looking after me at home while writing my thesis. They always provided a reminder that that's a lot of things going on outside the lab to give my mind a rest. A huge thanks to Emma and Jono for encouraging my creativity and hobbies. Sometimes the stress of work was a bit much but they always knew how to get me to relax. Thanks to my family for their support during my PhD, I missed them dearly the whole time. A final thanks to Bean and Mouse (my cats). I needed those cuddles.

Declaration

I hereby declare that the work presented in this thesis is solely the authors own work, and has not been submitted either partially or fully for an award of a higher degree elsewhere. The work presented is the authors unless referenced or with acknowledgement. I can confirm that the total length of this thesis is approximately 20,615 words and does not exceed the 80,000 word limit of a PhD thesis.

The author has made no publications.

Sam Dicker M.Phys

November 2025

Contents

List of Figures

List of Tables

Chapter 1

Introduction

Since the discovery of carbon nanotubes (CNTs) by L. V. Radushkevich and V.M. Lukyanovich in 1952 [1] (and popularised later by Sumio Iijima in 1991 [2]), their extraordinary mechanical and electrical characteristics have proposed many applications of CNTs. Applications include composite materials such as in roads [3], medical devices and applications such as in tissue engineering [4], ministration of electronics such as in wearable devices [5], and energy storage [6].

CNTs mechanical properties are extraordinary as they are incredibly stiff but lightweight, and have a tensile strength greater than that of steel [7]. Their electronic properties allow measurements in the quantum regime such as transport in few dimensions, single electron transistors (SETs), Coulomb blockade, and cotunneling effects or the Kondo Effect. CNTs also have high quality factors which when paired with their mechanical and electrical properties allows us to study the CNT mechanics in the quantum regime [8], which can be used for detecting minuscule forces on the CNT [9].

However, on this road of discovery, there are a few obstacles we need to overcome. Generally, CNT devices are a CNT suspended between a source and drain electrode over one or more gate electrodes [10] [11] [12]. When cooled to temperatures lower than 1K, the CNT exhibits Coulomb blockade where current through the device is blocked or allowed depending on the gate and bias voltage. By attaching a ac drive signal to the gate electrode, the nanotube can be driven, and by measuring

the average current through the device we can look for mechanical resonances of the CNT. This method is known as the rectification technique [11]. CNT resonances are distinguishable from electrical resonances as the resonance has a dependence on gate voltage and spring softening around the Coulomb peak. However, CNTs are prone to a phenomenon called parametric resonance [13].

Parametric resonances were first recorded by Michael Faraday in 1831 when he noticed that the fundamental frequency of standing waves of water in a wine glass was being excited by forces from double that frequency [14]. In the modern age parametric oscillators can be used for parametrically amplifying signals by varying some parameter of the resonator rather than through a noise producing external drive [15]. Parametric resonances in a CNT however produce resonances at similar frequencies as harmonics of the CNT, and show a gate dependence and spring softening exactly like the harmonics. This can obscure or confuse the user about which resonances are true directly driven harmonics of the CNT and which are parametrically driven resonances [11]. As the rectification technique has no time dependence, it is difficult to separate the directly driven resonances from parametrically driven resonances.

In this thesis we show a new technique by using the CNT as an up-converting electromechanical mixer and a state-of-the-art low temperature amplifier (travelling wave parametric amplifier (TWPA)) which is capable of providing high sensitivity time dependent measurements which is able to detect directly driven resonances of the CNT from parametrically driven ones.

This thesis describes a new technique for detecting CNT mechanical motion in a doubly clamped setup. It then goes onto described how we can use this new technique to distinguish parametric motion from directly driven motion, and then proves that the motion we are seeing is without a doubt parametric motion.

Chapter 2 gives an in-depth literature review of a CNT electrical and molecular structure, CNTs as a mechanical resonator, the rectification technique, and parametric resonances. In the structure section, we describe how the molecular structure of a CNT can be derived from a graphene sheet, and how the electrical structure of graphene can be applied to CNTs. We also discuss how quantized transport works in a CNT. In the mechanical resonator section, we explain how a nanotube can be

approximated as a beam and work out its harmonics. We also discuss how static forces and charges on the nanotube affect its resonance frequencies, as well as how a nanotube is driven and measured using the rectification technique.

Chapter 4 describes the cryogenic setup, fabrication of the device, and the TWPA used in the experiments described in the following chapters.

Chapter 5 describes the new electromechanical mixer technique with TWPA. It describes how we can use the CNT as a mixer for up-converting two signals and how this is detected in a spectrum analyser. It also describes the circuitry needed to perform a measurement with this technique and how the optimal parameters were found.

Chapter 6 describes how we distinguish parametric motion in the CNT from directly driven motion, and how we prove that the motion we are seeing is in fact parametric by looking at how the resonance peaks respond to drive power. The chapter is made up of two analyses, the first harmonic and the second harmonic. The first harmonic is used to show how this new technique can be used to distinguish parametric motion from directly driven motion and then proves it is parametric motion. The second harmonic uses these results to try and distinguish the resonances seen around the second harmonic to decipher which ones are parametric and which ones are directly driven.

Chapter 7 describes the conclusions of this work, how measurements could be improved in the future, and future experiments we could do.

Go to Contents

Chapter 2

CNT Electromechanics

2.1 CNT Molecular Structure

The molecular structure of a CNT can best be described by imagining a rolled up sheet of graphene. Ideal graphene is a two-dimensional sheet entirely compromised of carbon atoms. The carbon atoms in the plane are bonded together through the hybridisation of the $2s$, $2p_x$, and $2p_y$ orbitals producing strong σ-bonds between three of its neighbours. The $2p_z$ orbital, which is oriented perpendicular to the plane, hybridises with its neighbouring $2p_z$ orbitals to produce π-bonds above and below the plane. The π-bonds produce half filled bands of delocalised electrons which are responsible for most of graphenes interesting electrical properties.

The three σ-bonds produces a hexagonal arrangement of carbon atoms (See Figure 2.1(a)) giving graphenes a hexagonal (sometimes called triangular) Bravais lattice. The unit cell, S_{G}, containing 2 carbon atoms separated by one C-C bond length (1.42Å), and is defined by the vectors, $\boldsymbol{a}_1$ and $\boldsymbol{a}_2$ which are equal to:

$$\boldsymbol{a}_1 = a_0\left(\frac{\sqrt{3}}{2}, \frac{1}{2}\right) \quad \boldsymbol{a}_2 = a_0\left(\frac{\sqrt{3}}{2}, -\frac{1}{2}\right) \tag{2.1}$$

where a_0 is a lattice constant equal to $\sqrt{3}b = |\mathrm{a}_1| = |\mathrm{a}_2| \simeq 2.46$Å [16].

To create our CNT, we can imagine a 'ribbon cut' across the graphene sheet (See Figure 2.2) which would produce a range of different nanotubes configurations dependent on the angle of the cut. There are three types of configurations of nanotube:

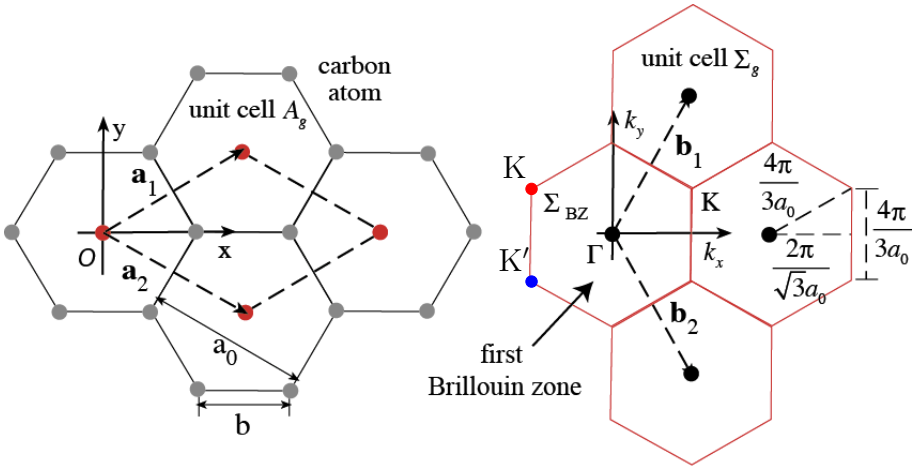

(a) Bravais lattice (b) Reciprocal lattice

Figure 2.1: The molecular structure of graphene. (a) Bravais Lattice; The unit cell S_{G} contains 2 carbon atoms and is made up of two vectors,$\boldsymbol{a}_1$ and $\boldsymbol{a}_2$, where $\boldsymbol{a}_1 = a_0(\frac{\sqrt{3}}{2}, \frac{1}{2})$ and $\boldsymbol{a}_2 = a_0(\frac{\sqrt{3}}{2}, -\frac{1}{2})$. The vectors have the same length of $a_0 = \sqrt{3}b$ where b is the atomic distance between 2 carbon atoms, $b = 1.42$Å. The area of the unit cell, A_{G} is equal to $\frac{\sqrt{3}a_0^2}{2}$. (b) Reciprocal lattice; The unit cell Σ_{G} is made up of two vectors, $\boldsymbol{b}_1$ and $\boldsymbol{b}_2$, where $\boldsymbol{b}_1 = \frac{2\pi}{a_0}(\frac{1}{\sqrt{3}}, 1)$ and $\boldsymbol{b}_2 = \frac{2\pi}{a_0}(\frac{1}{\sqrt{3}}, -1)$. The vectors have the same length of $b_0 = 4\pi\sqrt{3}a_0$. The area of the unit cell, B_{G}, is equal to $8\pi^2\sqrt{3}a_0^2$. The real basis vectors, $\boldsymbol{a}_1$ and $\boldsymbol{a}_2$ are related to the reciprocal basis vectors, $\boldsymbol{b}_1$ and $\boldsymbol{b}_2$, by $\boldsymbol{a}_i \cdot \boldsymbol{b}_j = 2\pi\delta_{ij}$ where $i, j = 1, 2$. Reproduced from [16]

.

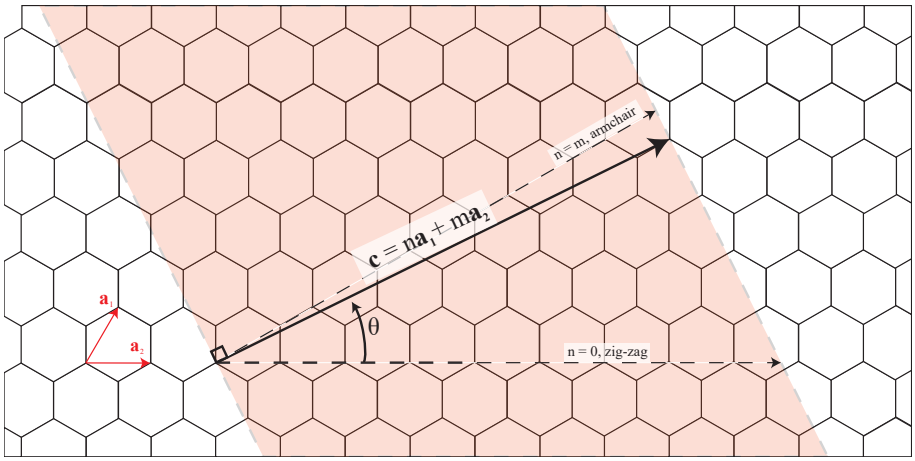

Figure 2.2: By performing a ribbon cut on a graphene sheet and rolling it perpendicular to the chiral vector, $\boldsymbol{c}$, you can create a CNT. The chirality of the CNT can be completely defined by its n and m indices. CNTs can be either armchair ($n = m$, $\theta = 30°$), zig-zag ($n = 0$, $\theta = 0°$), or chiral ($0° < \theta < 30°$).

Go to Contents

armchair, zig-zag, and chiral. The cut by a chiral vector $\boldsymbol{c}$ has the form:

$$\boldsymbol{c} = n\boldsymbol{a}_1 + m\boldsymbol{a}_2 \tag{2.2}$$

where n and m are constants. The ribbon cut is done perpendicular to the chiral vector, and can be rolled up into a cylinder forming a single walled CNT (SWCNT). Rolling multiple ribbons on top of each other produces multi-walled CNTs (MWCNT). The diameter, d_{SWCNT}, of the tube can be found via its chiral vector $\boldsymbol{c}$, given by:

$$d_{SWCNT} = \frac{|\boldsymbol{c}|}{\pi} = \frac{a_0}{\pi}\sqrt{n^2 + nm + m^2} \tag{2.3}$$

Depending on the catalyst, growth method, and other parameters SWCNTs can have a diameter as low as 0.4nm to around a few nm [17]; MWCNTs have diameters typically between 4 - 100nm [18]. The angle θ between the chiral vector $\boldsymbol{c}$ and the graphene lattice vector $\boldsymbol{a}_2$ is given by:

$$\theta = cos^{-1}\left(\frac{2m + n}{2\sqrt{n^2 + nm + m^2}}\right) \tag{2.4}$$

The three configurations of a CNT can be completely defined by the chiral vector, which often means nanotubes can be described by a pair of indices (n,m). An armchair nanotube is defined by $n = m$ ($\theta = 30°$). A zig-zag nanotube is defined by $n = 0$ ($\theta = 0°$). Chiral nanotubes are defined as having a chiral angle between 0° and 30°. Due to symmetries in the graphene lattice, chiral angles above 30° repeat.

2.2 Electrical Structure of CNTs

2.2.1 Band Structure of Graphene

To describe the band structure of a CNT, we once again can use graphene as the underlying structure performing a ribbon cut on it to transform it into a CNT.

Dispersion relations and band structure are defined momentum space (k) found by transforming the real space lattice to a momentum space lattice in a Fourier series. The real basis vectors, $\boldsymbol{a}_1$ and $\boldsymbol{a}_2$ are related to the reciprocal basis vectors, $\boldsymbol{b}_1$ and

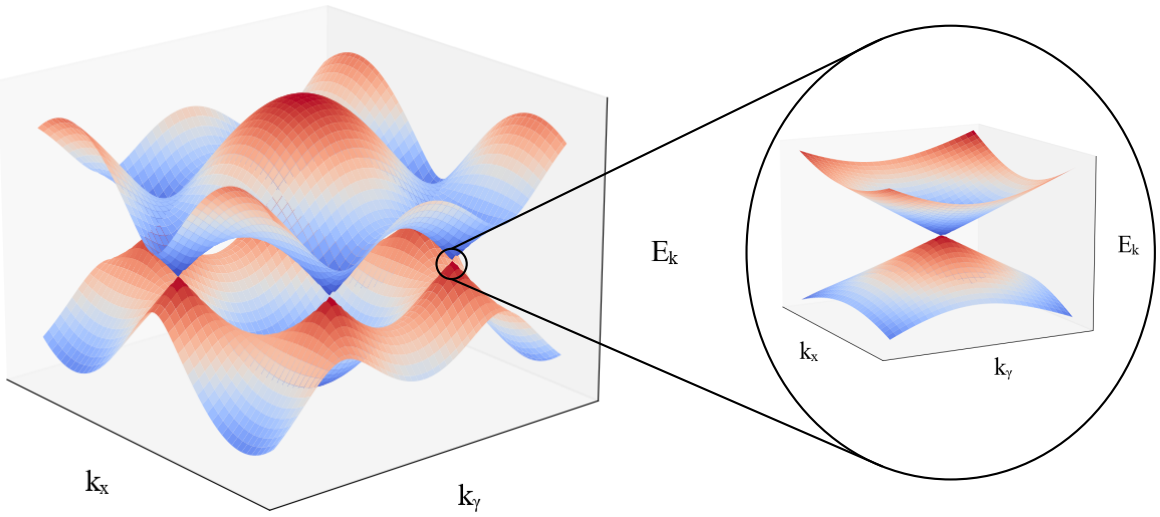

Figure 2.3: The electronic band structure of graphene showing the conduction and valence bands. The bands meet at the six corners of the first Brillouin zone; these points are known as Fermi points. If in the vicinity of a Fermi point, the energy dispersion relation can be approximated by Dirac cones with linear dispersion.

$\boldsymbol{b}_2$, by:

$$\boldsymbol{a}_i \cdot \boldsymbol{b}_j = 2\pi\delta_{ij} \text{ where } i, j = 1, 2 \tag{2.5}$$

which means the reciprocal lattice vectors, $\boldsymbol{b}_1$ and $\boldsymbol{b}_2$, are equal to:

$$\boldsymbol{b}_1 = \frac{2\pi}{a_0}\left(\frac{1}{\sqrt{3}}, 1\right) \quad \boldsymbol{b}_2 = \frac{2\pi}{a_0}\left(\frac{1}{\sqrt{3}}, -1\right) \tag{2.6}$$

The first Brillouin zone, Σ_{BZ}, showing the primitive cell of the reciprocal lattice in momentum space and the constructed Wigner-Seitz cell(s), Σ_{G}, are shown in Figure 2.1b. This gives the first Brillouin zone the same form as the original lattice but rotated 90° with respect to them.

Its clear that of the six corners of the first Brillouin zone we only need to consider the 2 equivalent corners denoted by $\boldsymbol{K}$ and $\boldsymbol{K'}$ as the other corners are symmetrical to this grouping. The corners $\boldsymbol{K}$ and $\boldsymbol{K'}$ can be defined as a function of the $\boldsymbol{b}_1$ and $\boldsymbol{b}_2$ vectors given by:

$$\boldsymbol{K} = \frac{\boldsymbol{b}_1 - \boldsymbol{b}_2}{3} = \frac{4\pi}{3a_0}(0, 1) \quad \boldsymbol{K'} = \frac{\boldsymbol{b}_2 - \boldsymbol{b}_1}{3} = \frac{4\pi}{3a_0}(0, -1) \tag{2.7}$$

In the nearest-neighbours tight-binding approximation, the dispersion relation [19]

is given by:

$$E^{\pm}(\boldsymbol{k}) = \pm\gamma_0\sqrt{1 + 4cos^2\frac{k_y a_0}{2} + 4cos\frac{\sqrt{3}k_x a_0}{2}cos\frac{k_y a_0}{2}} \tag{2.8}$$

where $E^{\pm}$ is the energy, the $+$ sign denotes the conduction band, $-$ sign denotes the valence band, and γ_0 is the carbon-carbon interaction energy which is 2.7 eV. Figure 2.3 shows the electronic band structure of graphene showing the conduction and valence bands. The bands meet at the six corners of the first Brillouin zone; these points are known as Fermi points. If in the vicinity of a Fermi point the energy dispersion relation can be approximated by Dirac cones. This linear dispersion can be found by performing a Taylor expansion of Equation 2.8 [19] which gives :

$$E^{\pm} \approx \pm\hbar v_F|\boldsymbol{k} - \boldsymbol{k}_0| \tag{2.9}$$

where $\boldsymbol{k}_0$ is the wavenumber at a Fermi point, v_F is the Fermi velocity of the π electrons equal to 0.87×10^6 ms^{-1}, and $\hbar$ is the Planck constant. A Fermi point is the point at which the valence band and the conduction band touch the Fermi surface at zero temperature; it is the point at which all electrons are in the valence band and none are in the conduction band. Dirac cones describe the boundaries of the valence and conduction bands. As a result of their shape, the charge carriers can be described by massless fermions which gives rise to ultra high carrier mobility and high electrical conduction [19].

Graphene is often described as a gapless semiconductor as in undoped graphene the bands touch exactly at the Fermi point, but provides a small gap at any other point.

2.2.2 Band Structure of CNTs

Using the band structure of Graphene as a basis, we can estimate the band structure of a CNT. This approach uses the 'ribbon' cut and a zone-folding approximation. This approximation works well for large diameter ($\geq$ 2 nm) and is able to described properties seen in CNTs. However the approximation does not work so well for small-diameter tubes where curvature effects cause re-hybridisation of the σ and π orbitals [19]. Rolling the graphene sheet also causes the carbon-carbon bond to

slightly shorten [19] which together with the curvature effects can cause SWCNTs that would be metallic to actually have a small bang gap causing them to become semiconducting.

Assuming a sufficiently large diameter, cutting and rolling the ribbon from our sheet of graphene leads to a cylinder with a periodic boundary condition along the tubes circumference given by $|\boldsymbol{c}| = d_{SWCNT}\pi$. Suppose a momentum space vector, k, we know that the boundary condition of $\boldsymbol{k} \cdot \boldsymbol{c}$ is equal to $2\pi p$ where p is an integer. The component of $\boldsymbol{k}$ that is parallel to nanotube axis ($k_{\parallel}$) is continuous. The component perpendicular to the nanotube axis however is quantized and must be equal to:

$$k_{\perp} = \frac{2\pi p}{|\boldsymbol{c}|} = \frac{2p}{d} \tag{2.10}$$

where p is an integer. Thus the spacing between the allowed states of $k_{\perp}$ are given by:

$$dk_{\perp} = \frac{2\pi}{|\boldsymbol{c}|} = \frac{2}{d} \tag{2.11}$$

If we plot these vectors onto the first Brillouin zone of graphene, we will find a series of parallel lines at running at an angle of $\pi/3 + \theta$ from the k_x axis defined by Equation 2.10 shown in Figure 2.4(a,c). The spacing of a single branch, $|d\kappa_{\perp}|$, to its nearest Dirac point to the vector $\boldsymbol{k}$ is found by taking the perpendicular component of the vector $\boldsymbol{\kappa}$ where $\boldsymbol{\kappa} = \boldsymbol{k} - \boldsymbol{K}$. We only look at one branch which is closest to E_F as this branch determines the transport properties of the nanotube. There are 2 possible situations: either the quantized line runs through the Dirac point and $|d\kappa_{\perp}| = 0$ (i.e there is no bandgap) resulting in a metallic nanotube; or the quantized lines do not run through the Dirac point and $|d\kappa_{\perp}| \neq 0$ (i.e there is a bandgap).

By combining Equations 2.2, 2.7, and 2.11, we can show that the condition for a metallic nanotube is given by:

$$\boldsymbol{K} \cdot \boldsymbol{c} = \frac{2\pi}{3}(n - m) = 2\pi p \tag{2.12}$$

therefore:

$$n - m = 3p \tag{2.13}$$

Go to Contents

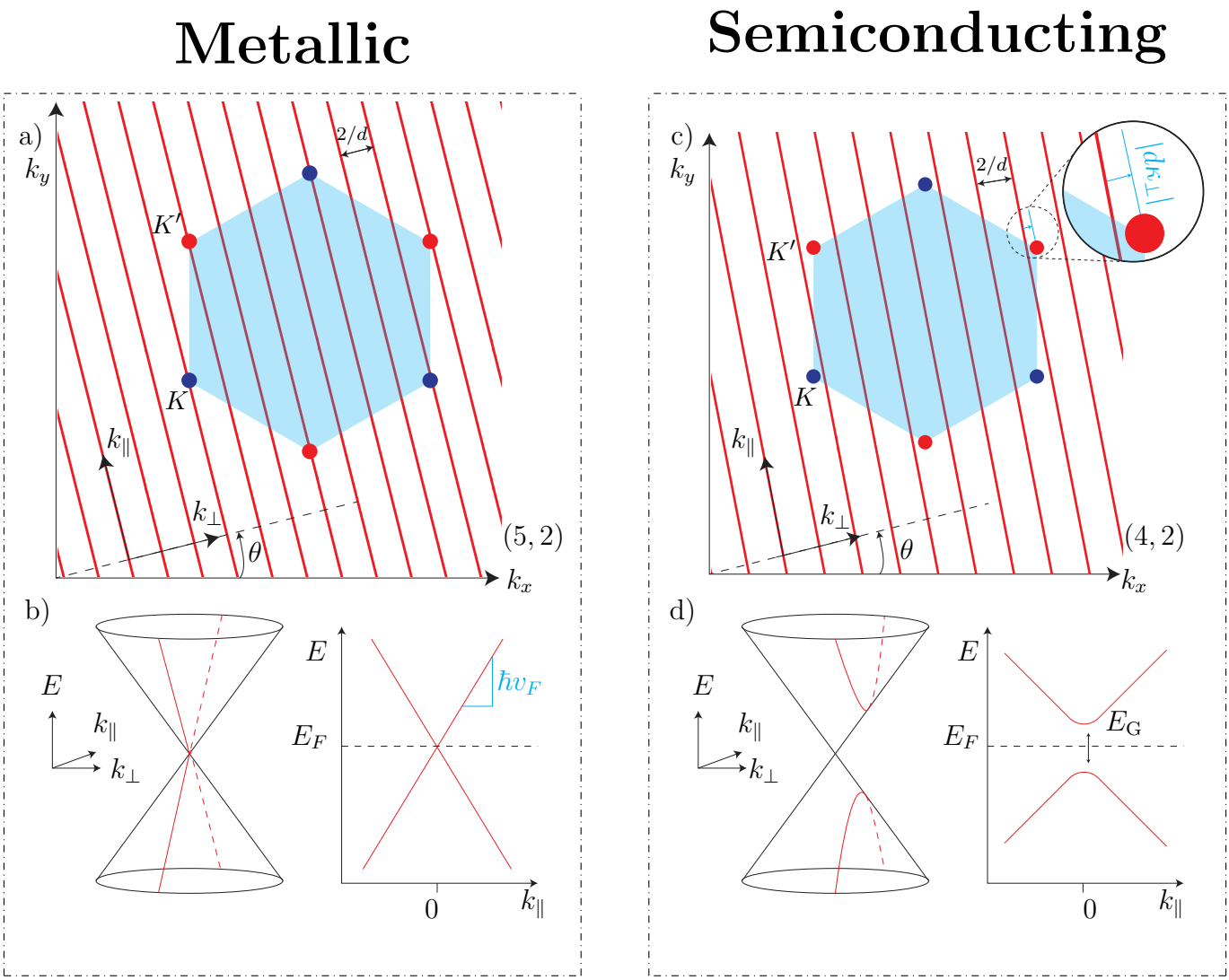

Figure 2.4: Bandstructure of SWCNTs from zone folding approximation. (a,c) The allowed k-states using the boundary conditions of the CNT applied as coloured lines to the first Brillouin zone of graphene. (a) depicts a metallic CNT as the quantization lines exactly intersect the Dirac points; (c) depicts a semiconducting CNT as the quantization lines do not intersect the Dirac points and therefore $d\kappa_\perp$ is nonzero. (b,d) The dispersion relations of lowest energy one dimensional band of a metallic (b) and semiconducting (d) CNT. The dispersion relations show how the nonzero $dk_\perp$ leads to a band gap shown in (d). Adapted from [20].

Go to Contents

If $n - m$ is a multiple of three, then the nanotube is nominally metallic [21]. This means that all armchair nanotubes are metallic (as m=n, so n-m=0) and every third zigzag nanotube is metallic (when m=0, n-m=n). Otherwise all other nanotubes are semiconducting (which implies that semiconducting nanotubes outweigh metallic ones 2:1), and their $|d\kappa_\perp|$ is nonzero. The bandgap, E_F, of a semiconducting nanotube is equal to $2\hbar v_F|d\kappa_\perp|$. The band gap is inversely proportional to the diameter of the tube [20] and is given by:

$$E_{\mathrm{G}} = \frac{4\hbar v_F}{3d} \simeq 700 \text{ meV}/d \text{ [nm]} \tag{2.14}$$

The electron dispersion hyperbola of a semiconducting nanotube is given by [22]:

$$E^{\pm}(\kappa_\parallel) = \pm\sqrt{\hbar^2 v_F^2 \kappa_\parallel + \frac{E_{\mathrm{G}}^2}{4}} \tag{2.15}$$

The low-energy dispersion relation is electron-hole symmetric unlike other semiconductors [23], but this symmetry can be quickly broken by local charges (either electrons or holes) in the nearby environment. The effective mass is calculated from the curvature of the dispersion relation. Assuming the effective mass of the electrons and holes is the same [24], and for low energies where $|E^{\pm}(\kappa_\parallel)| << E_{\mathrm{G}}$, the effective mass is given by [20]:

$$m_{\mathrm{eff}} = \hbar^2 \left(\frac{d^2 E}{d\kappa_\parallel^2} \right) \simeq \frac{E_{\mathrm{G}}}{7.3eV} * m_e \tag{2.16}$$

where m_e is the free electron mass. This means that a bandgap of 150 meV is equal to an effective mass of $\sim 0.021 m_e$. For a comparison gallium arsenide's effective mass is equal to 0.067 meV which makes CNTs preferable for quantum dot experiments due to their larger longitudinal level spacing [20].

Transport Regimes in SWCNTs

In graphene, the electronic density of states drops to zero around the $\boldsymbol{K}$ point as the conduction and valence bands meet. This is also true for metallic CNTs as the conduction and valence bands also meet at the $\boldsymbol{K}$ point. However the small bandgap exhibited in semiconducting CNTs means we should expect a large density of states above and below the bandgap. The density of states in semiconducting nanotubes

Go to Contents

spikes in maxima and minima for branches that come close to the $\boldsymbol{K}$ point. These large spikes in density of states are known as van Hove singularities [19].

To calculate the electronic density of states we first need to establish what kind of transport regime the nanotube is in. The transport regime depends on the electron mean free path λ_{MFP}, the length of the conductive channel L, and the width of the conductive channel W.

There are 3 different kinds of transport regimes:

- **diffusive**, shown in Figure 2.5 (a)

  In this regime, W and L are much larger than λ_{MFP}. This type of regime of electrical conduction is typical of room temperature metals which is best described by the Drude model. Back scattering events occur at impurities and lattice sites in the crystal. For a 2D dimensional semiconductor in this regime, the drift current of the electrons is given by:

$$I_{\mathrm{D}} = \frac{e^2 n \tau V_{\mathrm{SD}} W}{m^*} \tag{2.17}$$

  where e is the charge of an electron, n is the number of charges, τ is the mean scattering time, V_{SD} is the source/drain bias, W is the width of the channel, and m^* is the effective mass [25].

- **quasi-ballistic**, shown in Figure 2.5 (b)

  In this regime, L and λ_{MFP} are similar in length, and are larger than W. This type of regime of electrical conduction is best described by the Landauer formula. Back scattering events occur at impurities in the crystal and forward scattering events occur at the boundary walls. If bias voltage between the source and drain is small then the transmission T of the electrons is constant, the current I is given by [26]:

$$I = \frac{e^2 T}{h} V_{\mathrm{SD}} \tag{2.18}$$

  where T is the transmission probability, h is Plancks constant, and V_{SD} is a small bias voltage.

Go to Contents

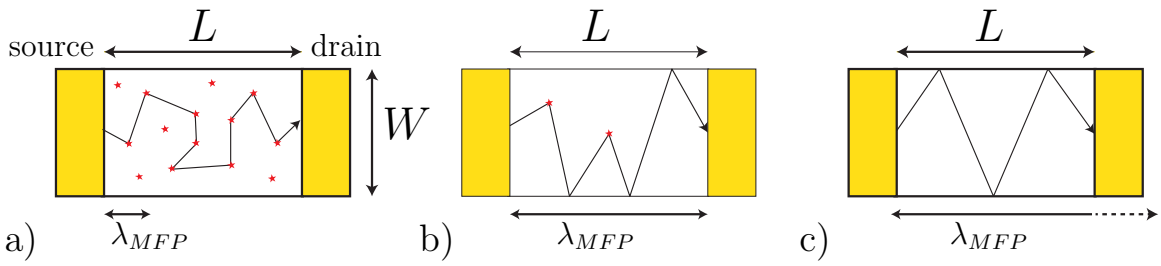

Figure 2.5: The different transport regimes. **a)** shows diffusive transport found in room temperature metals and best described by the Drude model. Electrons are backscattered at impurities in the crystal causing the electron mean free path to be much shorter than the conductors length. **b)** and **c)** shows quasi-ballistic and ballistic transport respectively both of which are described by the Landauer formula. In **b)** the mean free path of the electrons is similar to the conductor length; there is back scattering at small quantities of impurities in the crystal and forward scattering at the boundaries. In **c)** the mean free path of the electrons is far greater than the conductor length; there is only forward scattering at the boundary walls. Adapted from [28]

- **ballistic**, shown in Figure 2.5 (c)

  In this regime, λ_{MFP} is much greater than L and W. This type of regime of electrical conduction is best described by the Landauer formula (or the Meir–Wingreen formula if electron interactions are not neglected [27]). Only forward scattering events occur at the boundaries; there is no back scattering.

Since SWCNTs are nearly free of any impurities, the transport of electrons through the CNT should be quasi-ballistic. The electron mean free path of a CNT on SiO_2 at room temperature is $\sim$ 1 um but this increases with decreasing temperature. At 10 K the mean free path is several microns. As our device design involved a nanotube that was $\sim$ 1.2 um in length, cryogenic temperatures would be needed to get into the ballistic transport regime for our measurement. In a ballistic regime, the current through the CNT can be described by the Landauer formula given by:

$$I_i = \frac{e^2}{h} \sum_j (T_{j,i} V_i - T_{i,j} V_j) \tag{2.19}$$

where I_i is the current at terminal i, $T_{j,i}$ and $T_{i,j}$ is the sum of transmission probabilities from terminal i to terminal j and terminal j to terminal i respectively, and V_i and V_j are the voltages at terminal i and j respectively. In the simplest case, there will only be 2 terminals and therefore T refers to the transmission probability

of every channel contributing one wave mode to the waveguide. Therefore in this case:

$$\sum_{i \neq j} T_{i,j} = \sum_{i \neq j} T_{j,i} \tag{2.20}$$

Therefore:

$$I_i = \frac{e^2}{h} \sum_j T_{j,i}(V_i - V_j) \tag{2.21}$$

where $V_{\mathrm{SD}} = V_i - V_j$. Therefore:

$$I = \frac{e^2}{h} V_{\mathrm{SD}} \sum_j T_j \tag{2.22}$$

Therefore the current will be proportional to the transmission probabilities and the bias voltage.

Quantized Transport in CNTs

A quantum dot is often described as an artificial atom [29]; it is a structure which can be filled with a set amount of electrons (or holes) formed between 2 tunnel barriers formed on source/drain electrodes which it can exchange electrons between, and it is coupled capacitively to one or more gate electrodes.

Figure 2.6 (a) shows a simple configuration of how a quantum dot can be made using a CNT. Figure 2.6 (b) shows the equivalent component breakdown of (a). The tunnel barriers are represented by a capacitor $C_{[\mathrm{S,D}]}$ and resistor $R_{[\mathrm{S,D}]}$ in parallel, where the magnitude of the current passing from the source/drain to/from the quantum dot is dependent on the tunneling rates $\Gamma_{[\mathrm{S,D}]}^{[+,-]}$. The electrochemical potential of the quantum dot is tuned by altering the gate capacitance C_{G} via the gate electrode. All other capacitances from parasitic contributions are encompassed in C_{other}.

A quantum dot works by using the Coulomb repulsion between electrons forcing an energy cost to adding extra electrons on to the quantum dot from the source electrode. This energy is referred to as the charging energy. The charging energy E_C is given by:

$$E_C = \frac{e^2}{C_{\mathrm{dot}}} \tag{2.23}$$

where e is the charge of an electron, and C_{dot} is the total capacitance of the quantum

dot ($C_{\text{dot}} = C_{\text{S}} + C_{\text{D}} + C_{\text{G}} + C_{\text{other}}$). When cooled to cryogenic temperatures, the tunnelling of electrons from the source to the quantum dot is dramatically suppressed as the available thermal energy of the electrons is lower than the charging energy ($k_B T < E_C$ where k_B is the Boltzmann constant and T is the temperature). This phenomena is known as Coulomb blockade. The charges on the quantum dot become constrained to quantized integer multiples of the elementary charge which affect the transport characteristics of the quantum dot.

Low temperature electron transport through a quantum dot is best described by the constant interaction model [30]. The model is based on two assumptions. Firstly, all Coulomb interactions between electrons in the quantum dot, and between electrons in the surrounding environment can be summarised under a single constant capacitance, C_{dot}. Secondly, that the single particle energy levels are independent of these Coulomb interactions and therefore independent of the quantum dots occupation. Using these assumptions, the total energy of a quantum dot $U(N)$ with N electrons in the ground state, while ignoring the capacitance C_{other}, is given by:

$$U(N) = \frac{\Big(-e(N - N_0) + C_{\text{S}}V_{\text{S}} + C_{\text{D}}V_{\text{D}} + C_{\text{G}}V_{\text{G}} \Big)^2}{2C_{dot}} + \sum_{n=1}^{N} E_n \tag{2.24}$$

where e is the electron charge, N_0 is the charge occupancy when no voltage is applied and is set by local charges in the surrounding environment, V_{S}, V_{D}, and V_{G} is the voltages set to the source, drain, and gate, and E_n are the single particle energy levels found in the quantum dot. The electrochemical potential $\mu(N)$ of the quantum dot is given by:

$$\begin{aligned} \mu(N) &= U(N) - U(N-1) \\ &= (N - N_0 - \frac{1}{2})E_C - \frac{E_C}{e}(C_{\text{S}}V_{\text{S}} + C_{\text{D}}V_{\text{D}} + C_{\text{G}}V_{\text{G}}) + E_N \end{aligned} \tag{2.25}$$

where E_N is the occupationally energy at the Nth level. Note that from these equations the electrochemical potential $\mu(N)$ depends linearly on the gate voltage, but the total energy of the quantum dot depends quadratically. This dependence is the same for all of N and allows us to move the 'ladder' of electrochemical potentials

Go to Contents

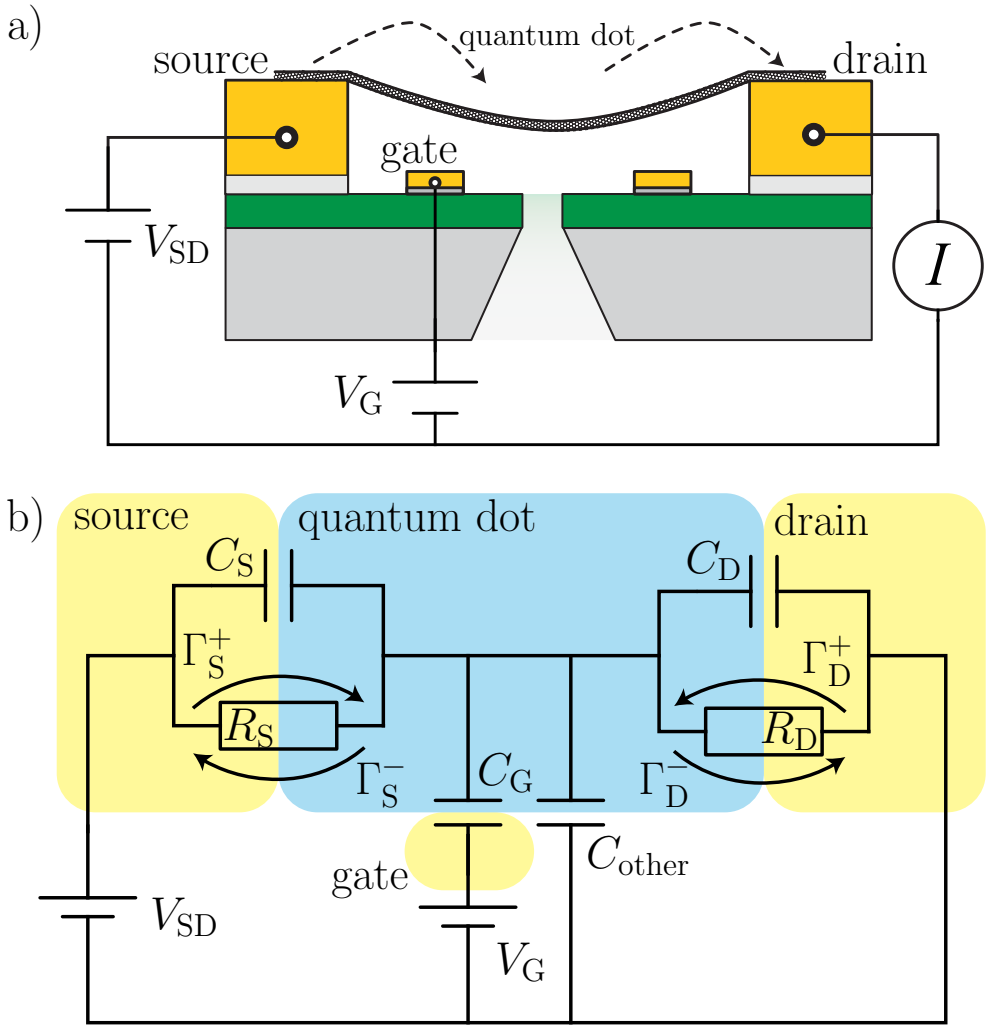

Figure 2.6: Schematics of a quantum dot device using a CNT connected between source and drain electrodes, and a gate electrode. **a)** A basic setup using a CNT to create a quantum dot. The nanotube is suspended between source/drain electrodes above a gate electrode that is capacitively coupled to it. A quantum dot is formed as tunnel barriers form at the source and drain due to a combination of Schottky barriers from the difference in materials and the gate electrodes potential. The number of electrons on the island and its energy levels can be tuned by adjusting V_G which can effect the current passing through the device. The current is also dependent on the bias voltage across the quantum dot. Adapted from [20]. **b)** The equivalent component circuit of (a) breaking the quantum dot down into capacitors and resistors. The blue shaded area represents the quantum dot, and the yellow shaded areas represent the various electrodes. The quantum dot is connected to the electrodes by tunnel contacts with capacitances $C_{[S,D]}$ and tunnel resistances $R_{t[S,D]}$. The tunnel rates of the electrons through the tunnel junctions to the quantum dot are given by $\Gamma^{[+,-]}_{[S,D]}$. A gate electrode is capacitively coupled to the quantum dot by C_G. All other capacitances from the environment around the quantum dot are encompassed in C_{other}.

Go to Contents

by tuning the gate voltage while the spacing between the 'rungs' remains the same. The spacing between the 'rungs' or states is called the addition energy $E_{\text{add}}(N)$ and is given by:

$$\begin{aligned} E_{\text{add}}(N) &= \mu(N+1) - \mu(N) \\ &= E_C + dE \end{aligned} \tag{2.26}$$

The addition energy is formed of a purely electrostatic component E_C and the energy spacing between two levels component dE. In the case of a CNT dE will only be nonzero when N is a multiple of four as the CNT receives a four fold degeneracy of electronic states from graphene; two from spin degeneracy and two fromValley degeneracy. This leads to a arithmetic sequence of spacing of states every 4 states.

The electrochemical potential needed to add an electron to source μ_{S} and the electrochemical potential of the drain μ_{D} is given by:

$$\begin{aligned} \mu_{\text{S}} &= E_F - eV_{\text{SD}} \\ \mu_{\text{D}} &= E_F \end{aligned} \tag{2.27}$$

where E_F is the Fermi level, and V_{SD} is the bias voltage which is the difference in voltage between the source and the drain. The electrochemical potential difference between μ_{S} and μ_{D} opens up an energy window equal to:

$$\mu_{\text{S}} - \mu_{\text{D}} = -eV_{\text{SD}} \tag{2.28}$$

This window is known as the bias window. This means that current will only flow when the source electrochemical potential, drain electrochemical potential, and gate electrochemical potential satisfy this condition:

$$\mu_{\text{S}} > \mu(N) > \mu_{\text{D}} \tag{2.29}$$

When the electrochemical potentials of the quantum dot are not aligned with the electrochemical potentials of the source/drain, as shown in Figure 2.7 (a), current flow is blocked and the device is in Coulomb Blockade. If the electrochemical potentials of the quantum dot are aligned with the electrochemical potentials of the

Go to Contents

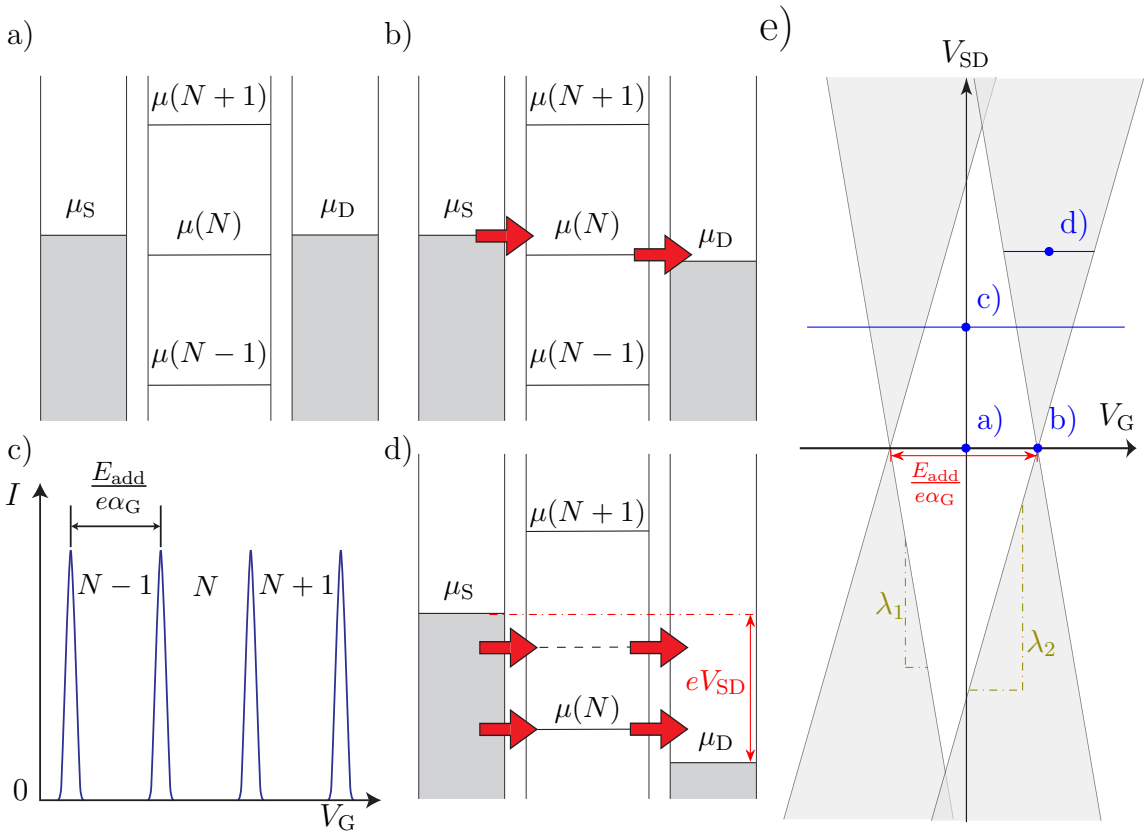

Figure 2.7: (a) (b) (d) show the ladder of electrochemical potentials in the quantum dot and how the position of the ladder affects electron transport. (a) shows a case when no current flows. The energy levels of the quantum dot are not aligned with the electrochemical potential of the source drain, therefore the quantum dot is in Coulomb blockade. (b) shows the opposite to (a), the levels of the quantum dot are aligned with the electrochemical potentials of the source drain and electrons are able to sequentially tunnel through to the drain via the quantum dot causing a current to flow. (d) shows that electrons are able to tunnel through to the drain as long as the quantum dot energy levels are within the bias window. In a high bias regime, electrons are able to move through the dot on a level involving an excited state (dash line). (c) The measured current of a quantum dot device as a function of gate voltage. By sweeping the gate voltage, the dot switches between Coulomb blockade and sequential electron tunneling. (e) Coulomb diamonds can be found by measuring current while sweeping the bias voltage and gate voltage. The resulting figure produces a series of diamonds where current is able to flow through the device (grey) and where it is blocked (white). The letters in blue represent the location of the (a),(b),(c), and (d). The line under (c) shows how the peaks are produced by sweeping gate voltage. The line under (d) shows the bias window. Adapted from [30]

Go to Contents

source/drain such that the quantum dot levels sit in the bias window, as shown in Figure 2.7 (b), then electrons are able to flow from the source to the drain by sequentially tunnelling through the quantum dot. By measuring the current while sweeping the gate voltage, we can tune the quantum dot through series of tunnelling and Coulomb blockade regimes which results in a series of peaks as shown in Figure 2.7 (c). The distance between the peaks is given by:

$$\Delta V_{\mathrm{G}} = \frac{E_{\mathrm{add}}}{e\alpha_{\mathrm{G}}} \tag{2.30}$$

where $\alpha_{\mathrm{G}} = C_{\mathrm{G}}/C_{\mathrm{dot}}$. α_{G} is the coupling strength between the quantum dot and the gate. In a high bias regime, the bias window is larger enough to encompass multiple levels of the electrochemical potentials and excited states which can contribute to the electron transport through the quantum dot, which is shown in Figure 2.7 (d). Coulomb diamonds appear by sweeping gate and bias voltage while measuring current as shown in Figure 2.7 (e). As the quantum dot is tuned between Coulomb blockade and sequential electron transport, the current plot shows a series of repeating diamond patterns, this type of plot is known as a stability diagram (Figure 5.2). The width of the peaks of current shown in Figure 2.7 (c) depend on the width of the bias window, best shown in Figure 2.7 (e) by the blue line under (d).

2.3 CNT Mechanical Resonators

With a CNT suspended between two electrodes above a gate electrode as shown in Figure 2.6 (a), the free hanging section of the CNT can vibrate through several vibrational modes. This includes in decreasing order of energy, radial breathing modes where the CNT circumference expands and contracts, stretching modes where the CNT expands and contracts along the nanotube axis, and lateral bending much like in a guitar string [31]. Since lateral motion of the CNT couples strongly to the quantum dot, we will only focus on these modes. The modelling of lateral vibrations of the CNT depends heavily on the tension and the diameter of the nanotube [31] between the two electrodes, and can either be modelled as a beam or a string under tension. The motion can be best described by the Euler-Bernoulli Theory.

Go to Contents

The lateral vibrations of the CNT has interesting effects on the quantum dot behaviour. Firstly, the displacement of the CNT from its equilibrium position caused by lateral vibrations causes the capacitance between the gate electrode and the CNT to constantly change which gives rise to non-linear conductance; something which we exploit later in this chapter with mixers. Secondly, a mechanical resonator and quantum dot in the same system means the transport properties and mechanical motion are strongly coupled. Two of the consequences of this coupling are frequency tuning of the mechanical resonances as the gate voltage is changed, and spring-softening of the conductance peaks when in sequential electron transport regimes [32, 33].

2.3.1 Euler-Bernoulli Theory of Mechanical Resonators

Euler-Bernoulli's beam theory is a method of calculating the continuum mechanics of beams when subjected to lateral forces. Even though a CNT only consists of a few atoms around its perimeter, the theory describes the mechanics of the CNT very well and is far less arduous than using the more common approach of molecular dynamic simulations [34].

By suspending a CNT of length L between a source and drain electrode we can create a mechanical resonator, as shown in Figure 2.8 (a). The CNTs equilibrium position is at height h_{G} above the gate electrode and the displacement of the CNT from the equilibrium position is given by $u(x)$; the displacement of the nanotube takes place in the z plane. The Euler-Bernoulli theory is a simplification of linear elasticity of solid objects, and shows that the deforming forces per unit length on a beam can be given by [35, 8]:

$$\rho A\frac{d^2u}{dt^2} + \Gamma\frac{du}{dt} + EI\frac{d^4u}{dx^4} - T\frac{d^2u}{dx^2} = 0 \tag{2.31}$$

where t is time, x is the position along the CNT, $u(x,t)$ is the displacement of the nanotube depending on the time and the position, ρ is the density of the CNT, A is the cross sectional area of the CNT, Γ is the damping rate per unit length, E is the CNTs Youngs modulus, I is the CNTs second moment of inertia, and T is the CNTs tension per unit length.

The first term describes the acceleration of the CNT. The second term describes the

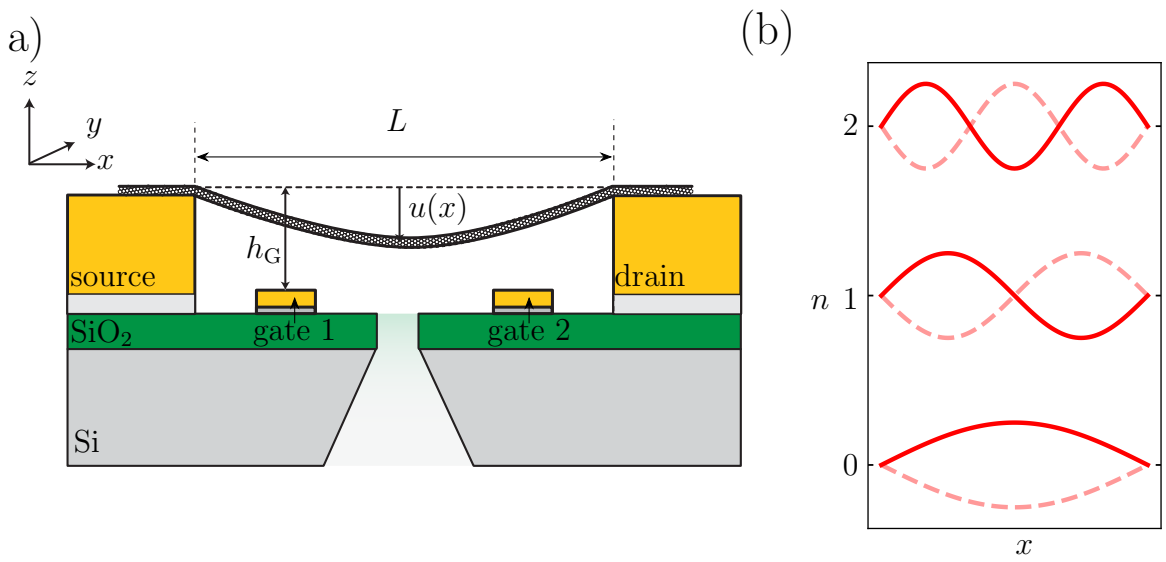

Figure 2.8: (a) A cross section of a CNT of length L suspended between a source and drain over a gate electrode creating a mechanical resonator. The CNTs equilibrium position is at height h_G above the gate electrode and the displacement of the CNT from the equilibrium position is given by $u(x)$. (b) The mode shapes of the first three modes of a mechanical resonator. n is the mode number. A mode number of zero represents the fundamental.

damping of the CNT via the damping coefficient Γ which is equal to:

$$\Gamma = \frac{\rho A \omega_0}{Q} \tag{2.32}$$

where ω_0 is the fundamental frequency, and Q is the quality factor. The quality factor ranges from $\sim 100,000$ [35] all the way up to 5 million [36]). ω_0 is typically on the order of 10^8 Hz [32]. ρ is generally on the order of $\sim 10^3$ kg/m^3 for SWCNT [37]. A is however tiny in comparison, being generally on the order of 10^{-17} m^2 for SWCNT [38] [35]. The third term describes a restoring force due to the rigidity of the CNT, and the fourth term describes a restoring force due to the tension of the CNT. To simplify our calculations of the resonant frequencies, we ignore the second term.

The nanotube is clamped via Van-der-Waals interactions at both source drain electrodes. The change in displacement from the equilibrium position of the nanotube at these two boundaries should also be zero. This means the nanotube mechanics

Go to Contents

must obey these boundary conditions:

$$u(0,t) = u(L,t) = 0 \tag{2.33}$$

$$\frac{du}{dt}(0,t) = \frac{du}{dt}u(L,t) = 0 \tag{2.34}$$

There are two limits we need to consider for finding solutions to Equation 2.31. In the first case, bending rigidity is dominant such that $EI \gg T$, and therefore the suspended nanotube acts like a beam resonator. This means equation 2.31 has eigenmodes u_n and the angular frequencies ω_n that satisfy:

$$\frac{d^4u_n}{dx^4} = \frac{\rho A}{EI}\omega_n^2 u_n \tag{2.35}$$

The general solution to Equation 2.35 is given by:

$$\begin{aligned} u_n =& C_1\Big(\cos(kx) + \cosh(kx)\Big) + C_2\Big(\cos(kx) - \cosh(kx)\Big) \\ &+ C_3\Big(\sin(kx) + \sinh(kx)\Big) + C_4\Big(\sin(kx) - \sinh(kx)\Big) \end{aligned} \tag{2.36}$$

where $C_{1,2,3,4}$ are coefficients, and $k^4 = \omega^2 EI/\rho A$. Using the boundary conditions outlined in Equations 2.34 the eigenfrequencies are given by [8]:

$$f_n = \frac{\omega_n}{2\pi} = \frac{\beta_n^2}{2\pi L^2}\sqrt{\frac{EI}{\rho A}} \tag{2.37}$$

where $\beta_n = k_n L$. As k_n changes depending on the mode number n, β_n is a numerical constant that takes a specific value for each mode.

In the second case, the tension is dominant such that $T \gg EI$, and therefore the suspended nanotube acts like a string under tension. Due to a CNTs high aspect ratio ($l \gg d$), the tension generally overwhelms the bending rigidity meaning nanotubes are generally modelled as strings under tension (growing conditions can also affect the tension). This tension can be further amplified by the gate electrode and by the nanotube deposition method. In a low tension regime, the non-linear effects appear in the CNT as the radius of the nanotube is on the same order as the displacement [8], however in a high tension regime, these effects are negligible [39]. A

string under tension has eigenmodes u_n and the angular frequencies ω_n that satisfy:

$$\frac{d^2u_n}{dx^2} = -\frac{\rho A}{T}\omega_n^2 u_n \tag{2.38}$$

Following similar general solutions to the first case, using the boundary conditions outlined in Equations 2.34 the eigenfrequencies are given by [8]:

$$f_n = \frac{\omega_n}{2\pi} = \frac{n+1}{2L}\sqrt{\frac{T}{\rho A}} \tag{2.39}$$

CNT mechanical resonators typically have a length equal to ~ 1 μm, a density of ~ 1350 kg/m^3, a cross sectional area of ~ 7.1 nm^2 [35], and a tension equal to ~ 3 nN [40]. This means fundamental frequencies of CNTs generally lie in the MHz regime.

2.3.2 Spring Softening and Static Forces

As stated earlier, the tension of the nanotube is tunable with the gate electrode. If we assume that the screening effects from the source and drain electrodes are negligible, then we can view the nanotube as an infinitely long grounded solid cylinder with radius r that is suspended at a height h_G above the conducting gate electrode with an electrostatic potential equal to V_G. Assuming the nanotube is not deflected from its equilibrium position ($u = 0$) and is in a high tension regime, then the potential profile $\phi(y, z)$ is given by [8]:

$$\phi(y,z) = V_G - V_G \frac{1}{\operatorname{arccosh}(\frac{h_G}{r})} ln\left(\frac{\left(z+\sqrt{h_G^2-r^2}\right)^2 + y^2}{\left(z-\sqrt{h_G^2-r^2}\right)^2 + y^2}\right) \tag{2.40}$$

Figure 2.9 shows the field lines of the electrostatic potential between the CNT suspended at height h_G above the gate electrode plane. By dividing the induced charge by the gate voltage, the capacitance per unit length $c_G(x)$ is found to be given by:

$$c_G(x) = \frac{2\pi\epsilon_0}{\operatorname{arccosh}(\frac{h_G - u(x)}{r})} \tag{2.41}$$

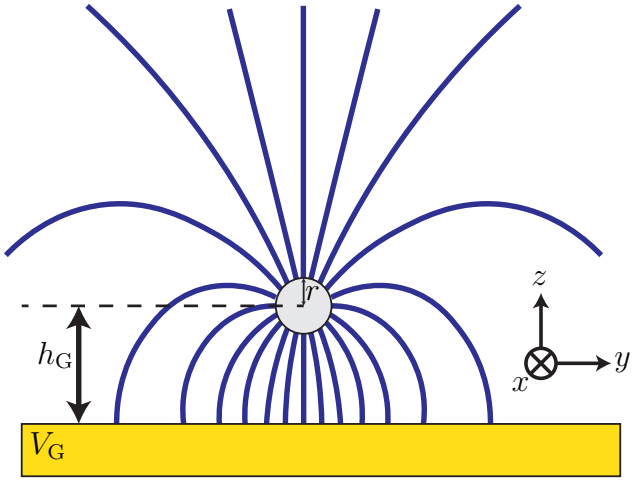

Figure 2.9: The field lines of the electrostatic potential between a CNT of radius, r, suspended a height h_G above a gate electrode. Changing the height causes the capacitance between the CNT and the gate C_G to change. Adapted from [8]

where h_G has been replaced with $h_G - u(x)$ to include the deflection of the CNT. To calculate the total capacitance felt by the nanotube, we need to add another term, l_{eff} the effective electronic length, to account for the curvature of the nanotube over the gate electrode. The effective electronic length is the length of the nanotube that interacts with the gate. The total gate capacitance is given by:

$$C_G = \frac{2\pi\epsilon_0 l_{eff}}{\operatorname{arccosh}(\frac{h_G-u}{r})} \tag{2.42}$$

The change in gate capacitance as the CNT deflection changes is then given by the derivative of C_G with respect to u which is given by:

$$\frac{dC_G}{du} = \frac{2\pi\epsilon_0 l_{eff}}{\sqrt{h_G + r - u}\sqrt{h_G - r - u}\,\operatorname{arccosh}^2\left(\frac{h_G-u}{r}\right)} \tag{2.43}$$

The nanotube therefore feels a force F given by [8]:

$$F_{dc} = -\frac{dU}{du} = \frac{1}{2}\frac{dC_G}{du}V_G^2 \quad \Rightarrow \quad F_{dc} \propto V_G^2 \tag{2.44}$$

where U is the electrostatic potential energy. Therefore increasing the gate voltage, increases the force on the nanotube pulling it towards the gate electrode. This

Go to Contents

increases its tension and therefore also increases its resonance frequency. This allows the CNT mechanical resonator to be tuned much like a guitar string just by altering the gate voltage. For low gate voltages where any intrinsic tension overwhelms any contribution from the gate voltage [8] or high voltages when dCg/du contributions affect the force [41], the relation between the resonance frequency and the gate voltage is more complex, but it is often reasonably well described by the quadratic relation [41] shown below:

$$f_i(V_\mathrm{G}) = a_i(V_\mathrm{G} - V_{0,i})^2 + f_{0,i} \tag{2.45}$$

where f_i is the frequency of the ith resonance, a_i is a constant of the ith resonance, V_G is the gate voltage, $V_{0,i}$ is the voltage offset of the ith resonance, and $f_{0,i}$ is the frequency offset of the ith resonance. The presence of $V_{0,i}$ is due to static charges on the substrate which causes an offset in the gate voltage. This has already been observed by Hüttner, N et al. [42].

In practice, the nanotube is not a grounded object and has some potential on it. If we represent this as V_CNT, Equation 2.44 becomes:

$$F_\mathrm{dc} = \frac{1}{2}\frac{dC_\mathrm{G}}{du}(V_\mathrm{G} - V_\mathrm{CNT})^2 \tag{2.46}$$

where the voltage on the CNT V_CNT is given by:

$$V_\mathrm{CNT} = \frac{C_\mathrm{G}V_\mathrm{G} - eN(q_\mathrm{CNT})}{C_\mathrm{dot}} \tag{2.47}$$

where $N(q_\mathrm{CNT})$ is the number of electrons on the CNT. In a region of Coulomb blockade, the number of electrons on the CNT remains constant and the force only depends on the gate voltage. In the event of a charge transition from a blocking to a sequential transport regime, the change in the number of electrons on the CNT over-screens the gate voltage so that the average voltage felt by the CNT is less. This over-screening gives rise to a reduction in tension and reduces the resonance frequency [35]. From the electrostatic force, we can calculate the change in the

Go to Contents

spring constant Δk of the CNT due to the sequential transport:

$$\Delta k = -\frac{dF_{\rm dc}}{du} \simeq \frac{V_{\rm G}(V_{\rm G} - V_{\rm CNT})}{C_{\rm dot}} \left(\frac{dC_{\rm G}}{du}\right)^2 \left(1 - e\frac{d\langle N\rangle}{dq_{\rm CNT}}\right) \tag{2.48}$$

where $d\langle N\rangle/dq_{\rm CNT}$ is the change in the average occupancy of electrons on the CNT. Using $\Delta k = 2m\omega_n\Delta\omega_n$ where m is the mass and n is the mode number, we can calculate the change in the resonance frequency during sequential transport regions:

$$\Delta\omega_n = \frac{V_{\rm G}(V_{\rm G} - V_{\rm CNT})}{2m\omega_n C_{\rm dot}} \left(\frac{dC_{\rm G}}{du}\right)^2 \left(1 - e\frac{d\langle N\rangle}{dq_{\rm CNT}}\right) \tag{2.49}$$

This means that during Coulomb blockade, where $d\langle N\rangle/dq_{\rm CNT}$ is zero, the resonance frequency depends quadratically on the gate voltage. However at a charge transition, $d\langle N\rangle/dq_{\rm CNT}$ becomes non-zero reducing the voltage 'seen' by the CNT, causing the spring constant to be softened which reduces the resonance frequency. This means stronger charge transitions, where $d\langle N\rangle/dq_{\rm CNT}$ is larger, cause a larger drop in frequency. This process shown in Figure 6.4 is known as spring-softening and results in drops in frequency around Coulomb peaks [32, 33].

2.3.3 Driving and Measuring a CNT

By adding an RF component to the gate electrode we can apply an electrostatic force to the CNT. The force is generated as the CNT and gate electrode form a capacitor as discussed earlier. This circuit is shown in Figure 2.10, and is an adaptation of the quantum spectroscopy circuit shown in Figure 2.6. Using Equation 2.44 and assuming no screening effects ($V_{\rm CNT} = 0$), the driving force $F_{\rm D}$ experienced by the CNT from the static potential $V_{\rm G}$ and the alternating potential $V_{\rm G}^{\rm ac}$ from the gate electrode is given by:

$$\begin{aligned} F_{\rm D} &\propto (V_{\rm G} + V_{\rm G}^{\rm ac}\cos(\omega_{\rm RF}t))^2 \\ &\propto V_{\rm G}^2 + 2V_{\rm G}V_{\rm G}^{\rm ac}\cos(\omega_{\rm RF}t) + \frac{1}{2}(V_{\rm G}^{\rm ac})^2(1 + \cos(2\omega_{\rm RF}t)) \end{aligned} \tag{2.50}$$

where $\omega_{\rm RF}$ is the drive frequency, and t is time. The first term in this equation provides a static deflection of the CNT as discussed earlier in §2.3.2. $V_{\rm G}$ is on the order of a few volts so this term applies a strong force on the nanotube. The second

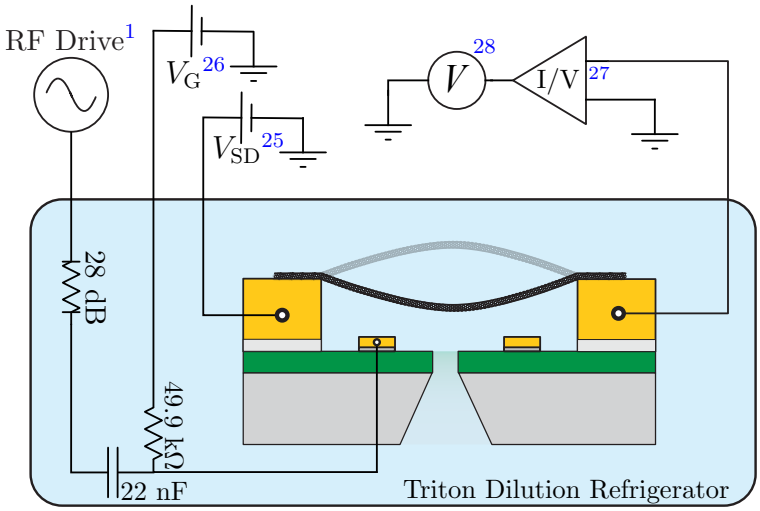

Figure 2.10: The circuit for driving and detecting a CNT vibration. The nanotube is driven by applying a small alternating voltage at a frequency of ω_{RF} to the gate electrode via an RF generator. The circuit is adapted from the setup shown in Figure 2.6.

term provides a periodic force on the CNT at a frequency of ω_{RF}. $V_{\mathrm{G}}^{\mathrm{ac}}$ is usually on the order of a few millivolts or less so this term applies a weaker force on the nanotube than the first term. The third term also provides a periodic force on the CNT at a frequency of $2\omega_{\mathrm{RF}}$. However as $V_{\mathrm{G}}^{\mathrm{ac}}$ is small, the force applied from this term is much weaker than the first and second term, but is still able to be detected in the right circumstances [40].

Since detecting the motion of a CNT is difficult, it is common to use the rectification technique [35]. By applying a small bias voltage across the source drain electrodes and a dc and ac voltage to the gate electrode, this technique converts the CNT deflection into an electrical current which can be measured with a multimeter.

When the CNT oscillates, the distance from the gate electrode to the CNT changes and therefore the capacitance $C_{\mathrm{G}}^{\mathrm{ac}}(t)$ is given by:

$$C_{\mathrm{G}}^{\mathrm{ac}}(t) = \frac{dC_{\mathrm{G}}}{du} u_{\mathrm{ac}} \cos(\omega_{\mathrm{RF}} t) \tag{2.51}$$

where u is the deflection of the CNT from the equilibrium position. When the nanotube is driven on resonance, $\omega_{\mathrm{RF}} = \omega_n$, the deflection of the CNT becomes large and therefore $C_{\mathrm{G}}^{\mathrm{ac}}$ becomes large. This is shown in Figure 2.11.

Since the quantum dot electrochemical potential and therefore the device conduc-

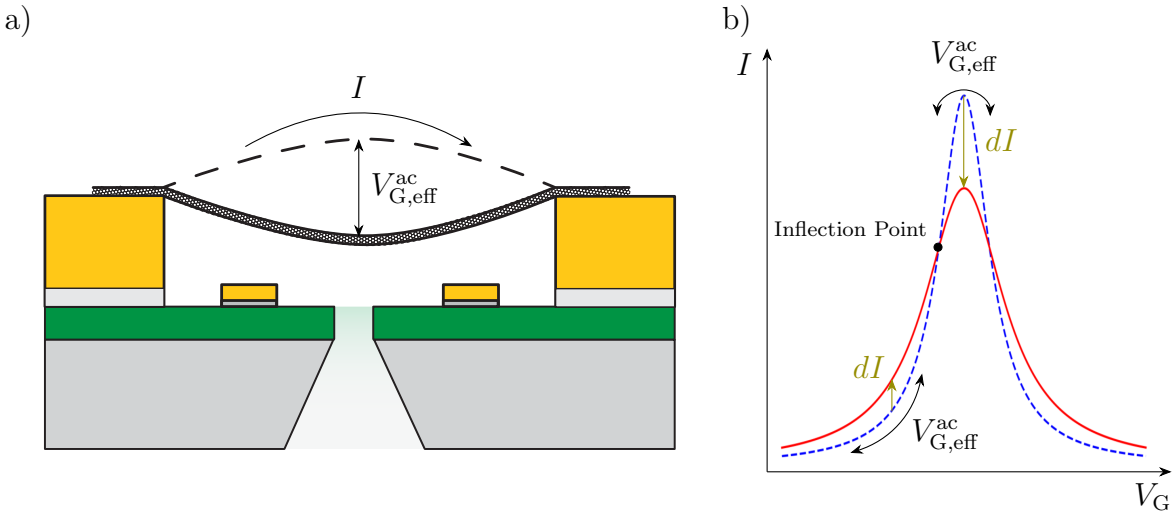

Figure 2.11: a) The vibrations of the CNT creates an effective gate voltage which blocks and unblocks the current through the device. Using the rectification technique only the dc component of the current can be measured. This dc component causes a shift in the expected current depending on where along the Coulomb peak you are. A larger amplitude causes the dc component to be larger causing a larger shift. (b) Motion of the CNT causes small changes in the gate capacitance, these small changes can be seen as an effective change in the ac component of gate voltage. Measuring a time average current gives different measurements from the actual conductance peak; at the top of the peak the time averaged current is lower than expected $dI < 0$, whereas on the flanks of the peak the time averaged current is slightly higher than expected $dI > 0$. (b) is adapted from [43].

Go to Contents

tance depends on the charge induced by the gate $q_c = C_G V_G$ shown in Equation 2.25, by driving the nanotube oscillations on resonance more charge is able to flow onto the CNT modulating the gate capacitance. We can therefore treat the ac modulation of the gate capacitance as an effective component of the gate voltage $V_G^{ac} = \frac{C_G^{ac}(t)}{C_G} V_G$. Using a Taylor expansion of the current with respect to gate voltage and using Equation 2.51 gives:

$$\begin{aligned} I(V_G + V_G^{ac}(t)) = I(V_G) &+ \frac{dI}{dV_G}\frac{V_G}{C_G}\frac{dC_G}{du} u_{ac}\cos(\omega_n t) \\ &+ \frac{1}{2}\frac{d^2I}{dV_G^2}\left(\frac{V_G}{C_G}\frac{dC_G}{du}\right)^2 u_{ac}^2\left(\frac{1}{2} + \frac{1}{2}\cos(2\omega_n t)\right) \\ &+ \frac{1}{6}\frac{d^3I}{dV_G^3}\left(\frac{V_G}{C_G}\frac{dC_G}{du}\right)^3 u_{ac}^3\left(\frac{3}{4}\cos(\omega_n t) + \frac{1}{4}\cos(3\omega_n t)\right) \\ &+ \mathcal{O}(u_0^4) \end{aligned} \tag{2.52}$$

The ac components, ω, 2ω, and 3ω, are too high to be measured by the frequency bandwidth of a multimeter, therefore we can only measure the time averaged current from the CNT oscillations. Omitting the high frequency terms from Equation 2.52 gives us the change in the dc current dI due to the mechanical oscillations:

$$dI = \frac{1}{4}\frac{d^2I}{dV_G^2}\left(\frac{V_G}{C_G}\frac{dC_G}{du}\right)^2 u_{ac}^2 \tag{2.53}$$

where d^2I/dV_G^2 is the rate of change in transconductance. This means that the time averaged measured current is given by:

$$\overline{I} = I(V_G) + \frac{1}{4}\frac{d^2I}{dV_G^2}\left(\frac{V_G}{C_G}\frac{dC_G}{du}\right)^2 u_{ac}^2 \tag{2.54}$$

Equation 2.54 shows that in order to a get a large mechanical signal, the change in transconductance must be large which is true around the conductance peaks in a Coulomb blockade regime. The rate of change in transconductance is zero around the inflection point/midpoint of a conductance peak and highest around the valley and peak of the conductance peak being on the order of several $\mu A/V^2$ [35]. This means on CNT resonance, the measured time averaged current on the Coulomb peak is lowered ($\overline{I} = I(V_G) - dI$), but near the valleys the measured time averaged current is raised ($\overline{I} = I(V_G) + dI$). This process is shown in Figure 2.11 (b).

Go to Contents

Chapter 3

Parametric Excitations

A parametric oscillator is a harmonic oscillator which is driven by varying a system parameter at some frequency typically different from the resonance frequency of the oscillator [39, 44]. It was first described by Michael Faraday in 1831 when he noticed that resonant frequencies of a wine glass could be driven by oscillations at twice that frequency. This is different from a conventional harmonic oscillator which is usually driven by some external force at the resonant frequency. To better explain this, we can imagine a child standing on a swing with their parent pushing them. For the parent to drive the swing on resonance, the parent must push the child at the same frequency of the resonant frequency. This is a driven harmonic oscillator. If we imagine the child without a parent to push them, they can still drive the swing to resonance (assuming a small starting perturbation) by periodically standing up and squatting. By standing up and squatting they change the moment of inertia of the system. By performing this action at twice the fundamental frequency of the swing, they can parametrically drive the swing at its fundamental frequency [45]. Its important to note that if the swing has no starting perturbation then the swing cannot be parametrically driven, and the child will simply be standing and squatting on a motionless swing.

In a simple harmonic oscillator without higher order non-linear terms, the equation of motion is given by:

$$\frac{d^2u}{dt^2} + \frac{\omega}{Q}\frac{du}{dt} + \omega^2 u = 0 \tag{3.1}$$

where $\omega(t)$ is the angular frequency of the oscillator which has a time dependent component, u is the displacement, and t is time. An externally driven harmonic oscillator driven by a sinusoidal force obeys:

$$\frac{d^2u}{dt^2} + \frac{\omega}{Q}\frac{du}{dt} + \omega^2 u = \frac{F_0 \cos(\omega_p t)}{m} \tag{3.2}$$

where F_0 is the drive amplitude of the externally applied force, and m is the mass of the oscillator.

A parametric oscillator is different from an externally driven harmonic oscillator. A parametrically driven oscillator applies a small perturbation to a parameter of the system, such that [46]:

$$\omega^2 \Rightarrow \omega^2(1 + h\cos(\omega_p t)) \tag{3.3}$$

where h is a small positive constant, and ω_p is the pump frequency. Combining Equation 3.3 and 3.1 gives:

$$\frac{d^2u}{dt^2} + \frac{\omega}{Q}\frac{du}{dt} + \omega^2(1 + h\cos(\omega_p t))u = 0 \Rightarrow \frac{d^2u}{dt^2} + \frac{\omega}{Q}\frac{du}{dt} + \omega^2 u = -\omega^2 uh\cos(\omega_p t) \tag{3.4}$$

Comparing Equation 3.4 and 3.2, they both have a driving term. In a driven harmonic oscillator the drive is given by $F_0 cos(\omega_p t)$ whereas in a parametric harmonic oscillator the drive is given by $\omega^2 uhcos(\omega_p t)$. This means that in parametric driving, the displacement u of the oscillator is a factor in the drive force, as is the frequency of the oscillator! When the oscillator is at rest, there is no way to drive it parametrically unlike an externally driven oscillator. But this also means that in parametric driving if the amplitude or the frequency of the oscillator increases then so does the driving force. This can lead to an exponential increase in the amplitude unlike the linear increase associated with externally driven oscillators. This can give way to incredibly low noise amplifiers as by altering one of the parameters of an oscillator rather than an external force, you can drive a resonance without adding more noise into the system.

In order to parametrically drive our oscillator we need to establish the value(s) of the pump frequency ω_p. The fundamental frequency of the oscillator ω_0 will be the easiest to drive. If the resonator is oscillating at its fundamental frequency then its

Go to Contents

displacement will be given by $u \propto u_0 \cos(\omega_0 t)$ where u_0 is the maximum amplitude. Therefore as the displacement is part of the parametric driving force, the parametric driving force is given by:

$$u_0 \cos(\omega_0 t)\cos(\omega_\mathrm{p} t) = \frac{u_0}{2}\cos\Big((\omega_\mathrm{p} - \omega_0)t\Big) + \frac{u_0}{2}\cos\Big((\omega_\mathrm{p} + \omega_0)t\Big) \tag{3.5}$$

In the simplest case we can drive the fundamental resonance effectively when $\omega_\mathrm{p} = 2\omega_0$ [47, 13]. It is possible to drive the fundamental using all integer fractions of the fundamental frequency such that $\omega_\mathrm{p} = 2\omega_0/n$ becoming less effective as n increases [35]. Parametric resonances occur in CNTs because the spring constant can be changed by changing the tension of the CNT via an alternating gate voltage [35]. CNT resonators are particularly susceptible to this as the change in spring constant with gate voltage , dk/dV_G, is large being proportional to $dk/dV_\mathrm{G} \propto 4V_\mathrm{G}^3$ [13, 35]. The change in spring constant, Δk is be given by [35]:

$$\begin{aligned}\Delta k &= -\frac{dF}{du} = \frac{1}{2}\frac{d^2 C_\mathrm{G}}{du^2}\Big(V_\mathrm{G}^2 + 2V_\mathrm{G}V_\mathrm{G}^\mathrm{ac}\cos(\omega_p t) + (V_\mathrm{G}^{ac})^2\cos(2\omega_p t)\Big) \\ &= \Delta k_0 + k_p\cos(\omega_p t) + k_p'\cos(2\omega_p t)\end{aligned} \tag{3.6}$$

where Δk_0 is the change in the spring constant from the dc gate voltage, $k_p\cos(\omega_p t)$ is the change in spring constant from the dc and ac gate voltage, and $k_p'\cos(\omega_p t)$ is the change in spring constant from the ac gate voltage. As $V_\mathrm{G}^{ac} \ll V_\mathrm{G}$, $k_p' \ll k_p$ and the last term can be neglected. Therefore when $\omega_p = 2\omega_0$ we can parametrically drive the fundamental frequency.

The tunability with gate voltage and the parametric motion of a CNT be used as a parametric amplifier [48, 13] as the pump frequency ω_p does not need to be exactly $2\omega_0$ to drive the fundamental. Instead a pump frequency of $2\omega_0 + \sigma$ where $\sigma \ll \omega_0$ can be used for parametric driving. Unfortunately in most other cases when trying to use a CNT in an electromechanical system, this can can lead to scenarios where parametric resonances are confused for harmonics of the CNT [11].

Using the rectification technique described in §2.3.3, it is difficult to determine the difference between a parametrically driven and the harmonics of the CNT (for this point, harmonics of the CNT will be described as directly driven). This is due to

two reasons:

- Rectification technique measurements have no time dependence, meaning parametric resonances or direct resonances appear as a static change at the same drive frequency.
- Rectification technique measurements typically have low signal to noise ratios, requiring high drive powers to see resonances. Since parametric resonances are due to non-linear motion, reducing the drive power would eliminate parametric resonances.

In the following chapters we describe how we set up a new kind of technique for measuring CNT motion with time dependence and improved signal to noise ratio which can determine directly driven resonances from parametric ones.

Go to Contents

Chapter 4

Cryogenic Setup and Device Fabrication

In this chapter we discuss briefly the device fabrication and the wiring in the dilution refrigerator for measuring CNT motion. We also give a brief overview of how the travelling wave parametric amplifier (TWPA) in the fridge works in amplifying the mechanical signals from the CNT.

The full device fabrication contains steps for turning a CNT into a magnetic resonance force microscope (MRFM). The device used in this thesis uses the device fabrication steps 1 to 15 laid out in Patrick Steger's 2025 thesis [40]. The final steps of the device was to back etch the silicon of the device to create a shadow mask such that magnetic material can be deposited on the CNT device without hopefully affecting the flexibility and without massively affecting the quality factor. Due to time restraints, the depositing of the magnetic material was not completed however this opened up the opportunity to perform other interesting scientific experiments with the nearly finished device such as parametric detection and Brownian motion detection in a CNT [40].

4.1 Device Fabrication

The basic principles of the device is a CNT connected between a source and a drain electrode, while suspended freely over one or more gate electrodes. The source and

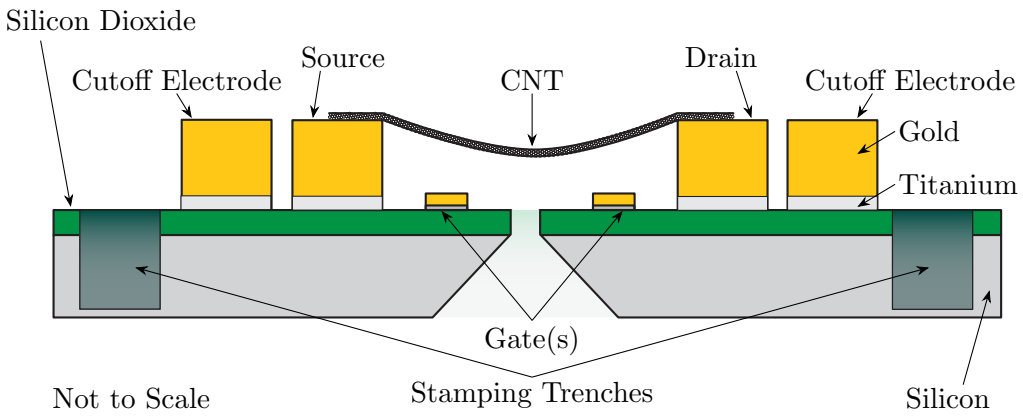

Figure 4.1: Side cut of our device with suspended nanotube. The schematic shows the stamping components (the cut-off electrodes and stamping trenches) and the components for measuring CNT electromechanics at low temperature (source/drain electrodes, and the gates). The patterns were developed on a silicon dioxide substrate to insulate the nanotube as we did not plan on back-gating the device. The etching of the silicon behind the device may have improved the quality of the device by reducing any electrical noise.

drain electrodes are used to apply a bias voltage to the CNT, while the gate electrode is used to both drive the CNT and apply gate voltages to it.

Figure 4.1 shows the cross section of our device. It shows a CNT suspended between a source and drain electrode over two gate electrodes. Beside the source and drain electrodes there are cut-off electrodes, and next to these are stamping trenches. The additional cut-off electrodes and stamping trenches are part of a unique way the nanotube was placed onto the device. The nanotube was grown in a chemical vapour deposition (CVD) furnace onto a quartz fork with nanoparticles of cobalt on its tines. This fork was loaded into a modified probe station where the fork was stamped down onto the device pulling the CNT across the four electrodes. The cut-off electrodes are then used to cut the CNT and anneal it to the source and drain electrodes. The fork is then retracted leaving the CNT behind [49, 50]. This method was chosen due to its repeatability as the device is not damaged during CNT growth. The stamping setup was designed around Patrick Steger's previous work from Regensburg [51]. The stamping method may put the CNT under more tension than on-chip growth but time didn't allow for testing of this. For more information on the stamping process see §4.2.3 of Patrick Stegers Thesis[40] .

The cut-off, source/drain, and gate electrodes were patterned on a silicon diox-

ide/silicon wafer and were made using a combination of electron beam lithography (EBL) and photolithography. A thermal evaporator was used for metallisation. The stamping trenches were made using a thick etching mask and a reactive ion etcher (RIE). The cut away in the silicon and silicon dioxide in between the electrodes and under the CNT is for eventually depositing magnetic material such as cobalt onto the CNT hopefully making the CNT sensitive to alternating magnetic fields. This gap in the silicon may be the reason why the CNT has improved quality by reducing electrical noise in the silicon. For more information on the full fabrication of the device see §4.2.4 of Patrick Stegers Thesis [40].

The device was wire-bonded and glued onto a QDevil daughter board and loaded onto a QDevil motherboard inside the Triton fridge puck. The Triton fridge is covered in the next section. For more information on the loading of the device see §2.2 of Patrick Stegers Thesis [40].

4.2 Dilution Refrigerator Wiring

A dilution refrigerator is needed for our experiment in order to:

- Achieve Coulomb blockade by suppressing transmission rates through the quantum dot which require temperatures lower than 1 K.
- Minimise thermal vibrations by cooling it to its mechanical ground state which temperatures less than $T = hf_0/k_B \approx 12.5$ mK.
- Utilise very low noise amplifiers which use super-conducting niobium and therefore require temperatures less than 7-9 K.

In order to cool the CNT to these temperatures we used an Oxford Instruments Triton DR-15-300-H dilution refrigerator. It is capable of cooling to a base temperature of less than 8 mK although device temperatures may differ depending on thermal connectivity.

A dilution refrigerator is a cryogenic fridge that uses a helium-3/helium-4 mixture to obtain cooling to temperatures lower than 10 mK. There are two kinds of dilution refrigerators: 'wet' fridges and 'dry' fridges. In a wet fridge, the dilution refrigerator

Go to Contents

is submerged in a bath of liquid helium, surrounded by a vacuum, surrounded by a bath of liquid nitrogen, and finally another vacuum. The system is pre-cooled using nitrogen bath,the helium bath, and a 1 K bath. The nitrogen bath is also used to reduce the boil off of the helium and provide more noise isolation. In a dry fridge, the pre-cooling is achieved using a pulse tube refrigerator (PTR) which in the Triton can reach a pre-cooling temperature of ∼3.5 K. We used a dry fridge as these fridges are generally cheaper and simpler to use than a wet fridge as they do not require periodic filling of liquid helium to maintain a low temperature. However due to the pulse tube the system generally is more noisy due to vibrations from the piston.

The fridge reaches colder temperatures than what is possible with just the pulse tube by exploiting the phase separation boundary that forms between ^{3}He and ^{4}He. A dilution unit is shown in Figure 4.2. A dry fridge is a combination of a dilution unit and a pulse tube.

The pre-cooling of the pulse tube allows the ^{3}He-^{4}He mixture to condense into a liquid in the dilution unit. By pumping on the dilution unit we can further cool the helium by causing it to evaporate. Once the temperature has cooled below ∼0.87 K, the mixture separates into two phases, a dilute phase and a concentrated phase. The dilute phase has ∼6.5% ^{3}He concentration whereas the concentrated phase has 100% ^{3}He concentration. This split occurs because ^{3}He atoms are fermionic whereas ^{4}He atoms are bosonic, as well as a difference in inter-atomic forces between the two isotopes. The concentrate phase (containing 100% ^{3}He) is less dense than the dilute phase and therefore sits on-top of the dilute phase in the mixing chamber. A pipe is extended into the mixing chamber which allows the dilute phase to get to the still but not the concentrate phase. ^{3}He has a much higher vapour pressure than ^{4}He which causes mostly ^{3}He to evaporate in the still. This evaporation shifts the equilibrium in the mixing chamber, causing ^{3}He atoms in the concentrate phase to cross the phase boundary into the dilute phase. This process is an endothermic process which takes energy from the surrounding space. Applying a small amount of heat through the still heater causes more ^{3}He to evaporate in the still which can allow, counter intuitively, for more cooling power in the mixing chamber.

Wiring and setup of the Triton fridge was done prior to my arrival at Lancaster, for

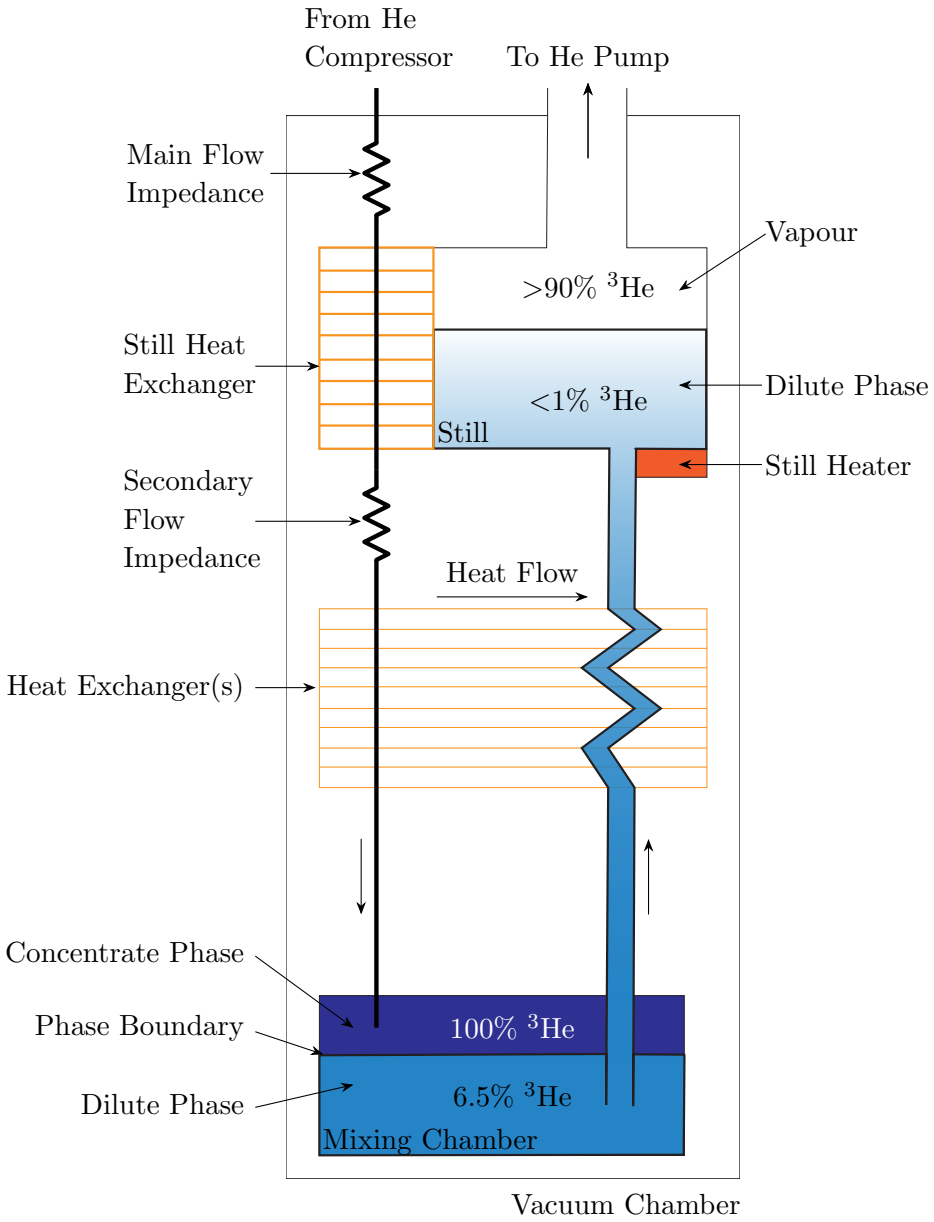

Figure 4.2: Schematic of a dilution refrigerator using ^{3}He and ^{4}He. A dilution refrigerator exploits the endothermic process that occurs when ^{3}He travels from the concentrate phase to the dilute phase in the mixing chamber. The still heater is used to 'pull' and circulate ^{3}He throughout the dilution unit.

Go to Contents

a deeper explanation of the system and the wiring see [40] [52]. From this setup, we are interested in the attenuators used for each of the various ac lines going from room temperature to the mixing chamber. We are interested in the attenuators as this allows us to work out the actual power seen by the device. The attenuation and gain of each ac line is shown in Figure 4.3.

Attenuators are used in the Triton fridge on the ac lines to try and dissipate thermal noise that may come in from the higher stages but also has the affect of dissipating signals. This is often not that concerning for quantum devices as the signal powers generally needed are on the order of ∼-60 dBm [53] and the attenuation can easily be overcome by increasing the power on the signal generator.

The attenuators are anchored to the plates on each stage of the Triton fridge in order to properly thermalise the attenuator to reduce blackbody radiation from the attenuator. Higher attenuation however causes more heat dissipation and for that reason the attenuators are spread out over various stages in order to mitigate this. The attenuation of each ac line going into the fridge is shown in Figure 4.3 (a). Placing attenuators on readout lines is not recommended as attenuators would diminish signals coming from our sample. Therefore instead circulators are used in order to protect the sample and TWPA from any noise coming from the higher stages, as well as stopping any reflected signals from making their way back down to the sample. A low pass filter is used after the TWPA and dual circulators to reduce the spectral density of the outgoing signal so any amplifiers used at higher stages aren't compressed [54].

Figure 4.3 (b) shows the transmission of each ac line going into and out of the fridge while at base temperature and the travelling wave parametric amplifier (TWPA) not being pumped. The transmission was measured using a Keysight P9375A Vector Network Analyser (VNA) [40] [52]. The readout ranges of each outgoing line are shown in the highlighted sections. These highlighted ranges are limited by the specifications of the devices connected to them. The radio frequency (RF) Out line is limited to the frequency range of the High-electron-mobility transistor (HEMT) amplifier. The microwave frequency (MW) Out line is limited on the low side by the frequency range of the circulators and on the high side by the cutoff of the low

Go to Contents

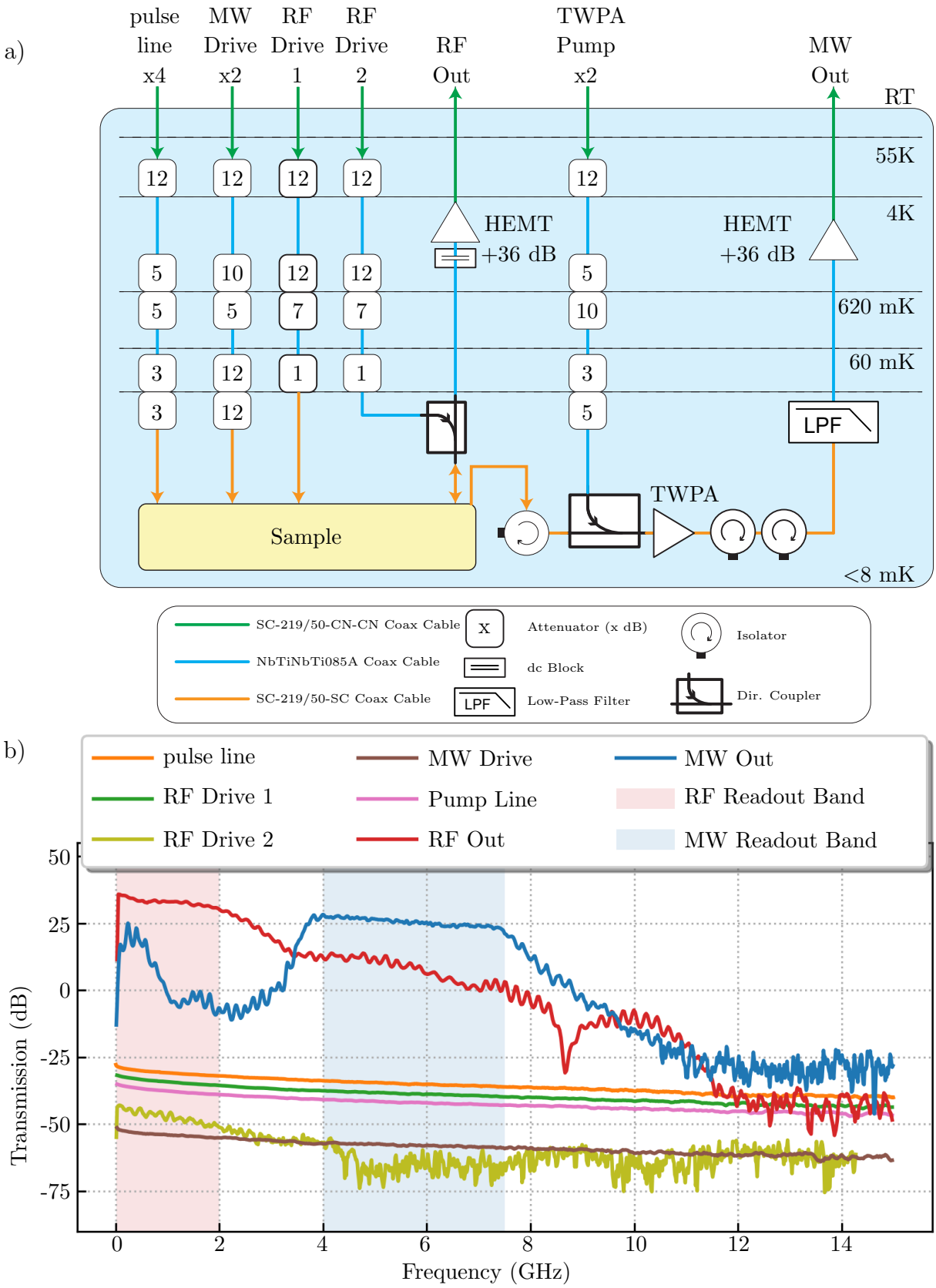

Figure 4.3: a) The attenuation of the wires installed in the Triton dilution fridge. This includes four pulse lines, two low noise microwave (MW) inputs, four radio frequency (RF) inputs with reflectometry, one travelling wave parametric amplifier (TWPA) pump line, and one MW readout. Cabling for the TWPA and HEMTs are not shown. (b) The transmission gain/loss of each ac wire going into the Triton fridge. (a) is redrawn and (b) reproduced from [40].

Go to Contents

pass filter at 7.5 GHz. This places an optimum range for the MW Out from 4 GHz to 7.5 GHz. The higher loss in transmission at higher frequencies comes from the effective cross section of the wire being reduced by skin effects. We decided to use one pulse line for the RF drive, one MW drive line for the MW probe tone, and MW Out for measuring signals using the spectrum analyser in order to utilise the TWPA.

4.3 Travelling Wave Parametric Amplifier

In this section we will go over the travelling wave parametric amplifier (TWPA) that we will be using for the rest of this thesis in order to measure signals coming from the CNT device. The TWPA is connected to the mixing chamber stage of the Triton fridge as shown in Figure 4.3. The amplifier was supplied by our collaborators at VTT Technical Research Centre at Finland Ltd. The full design of the amplifier, how it was made by VTT, and full theory is not described in this thesis; instead only a brief explanation of the TWPA is included. The performance of the TWPA was characterised by Patric Steger[40] and Deepanjan Das[52] which includes the tuning of the amplifiers flux bias, its application while inside a magnetic field, and the noise performance of the amplifier.

Our TWPA is a super-conducting coplanar waveguide (CPW) transmission line made up of super-conducting non-linear asymmetric inductive elements (SNAILs) [55] shown in Figure 4.4 (a). The superconductor used is niobium. Each SNAIL is comprised of two or more Josephson junctions in parallel which is shown in Figure 4.4 (b). One side consists of n number of Josephson junctions with tunnelling energy E_j while the other side consists of just one smaller Josephson junction with tunnelling energy αE_j. The impedance of the device depends on n and α, and the external applied flux bias ϕ_{ext}. By carefully tuning ϕ_{ext} it is possible to impedance match the TWPA to the rest of the MW Out circuitry at 50 Ω [54]. In our TWPA ϕ_{ext} comes from a super-conducting flux bias line on the TWPA chip which is biased by a dc current coming from a battery-powered voltage source. The non-linearity of the SNAILs allows for parametric amplification in a 3-wave mixing process shown in Figure 4.4 (c). The SNAIL works as an amplifier when a pump frequency f_{p} is

Go to Contents

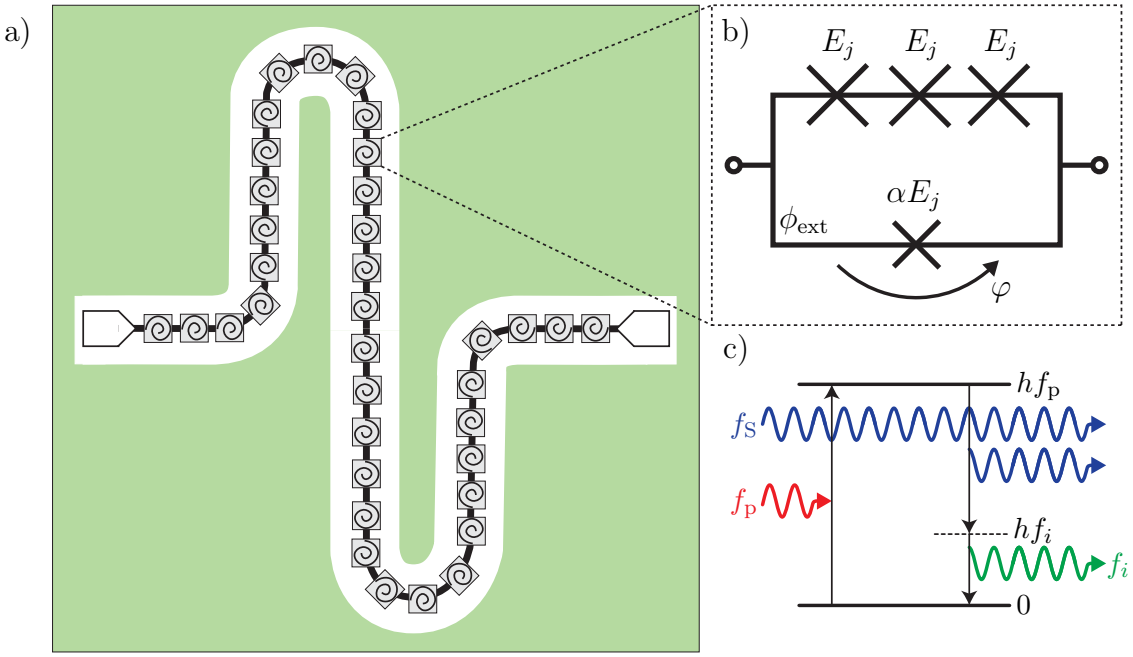

Figure 4.4: a) The TWPA circuit without magnetic flux bias line. The circuit is a super-conducting coplanar waveguide (CpW) transmission line made up of super-conducting non-linear asymmetric inductive elements (SNAILs). The non-linearity of the SNAILs allows for parametric amplification in a 3-wave mixing process. The TWPA is an array of multiple SNAILs stitched together. (b) shows the layout of a SNAIL with three larger Josephson junctions with tunnelling energy E_j and one smaller Josephson junctions with tunnelling energy αE_j in a parallel circuit. The impedance of the SNAIL is tuned by an external flux bias ϕ_{ext}. The SNAIL is parametrised by the phase difference φ across it. (b) is reproduced from [55]. (c) Parametric amplification of a signal f_{S} by 3-wave mixing. A photon from the pump frequency f_{p} excites an energy level which decays when stimulated by a weak signal from f_{S} creating another photon also at f_{S}. A photon at f_i, the idler frequency, is also produced to conserve energy; f_i is equal to the difference between f_{p} and f_{S}. Reproduced from [40].

Go to Contents

applied due to the non-linearity in its inductance. This creates a virtual energy level at hf_{p}. When a weak signal f_{S} stimulates the energy level it decays into a photon also at frequency f_{S}, and also creates a photon with frequency f_i at the difference between f_{p} and f_{S} in order to conserve energy.

The TWPA can be operated in two modes:

- Phase-sensitive gain

  The pump and signal have a fixed phase relation in the TWPA. This means that $f_{\mathrm{p}} = 2f_{\mathrm{S}}$ and as such the idler frequency f_i is equal to the signal frequency f_{S} in 3-wave mixing.

- Phase-insensitive gain

  The pump, signal, and idler frequencies have to obey $f_{\mathrm{p}} = f_{\mathrm{S}} + f_{\mathrm{D}}$ but $f_{\mathrm{S}} \neq f_i$ which is more suitable for our application explained in §5.

For this thesis, the TWPA used a pump frequency of 12 GHz, a flux bias current of 819μA, and is in phase-insensitive mode allowing broad band amplification.

Go to Contents

Chapter 5

A Time Dependent Technique: An Electromechanical Mixer

Unfortunately using the rectification technique to measure the CNTs mechanical oscillations is somewhat limited and the only way to determine parametric motion from directly driven motion is by comparing the quadratic curve ratios. In the results from this thesis comparing the quadratic curve ratios does work very well as shown in Figure 6.5 (what is meant by quadratic curve ratios is explained in §6.2), but attempts at this by others are not as clear [11] as the ratio is dependent on the bending rigidity of individual CNTs. Therefore comparing the curve ratios to determine whether a mode is driven parametrically or directly is dubious at best.

The main problem with the rectification technique for distinguishing parametric modes from directly driven modes is that it lacks any time dependence, such that any vibrations of the CNT regardless of what frequency they are actually coming from will show up as a current, and determining what frequency this current has come from is impossible. We therefore need a way of measuring time dependent signals from the CNT. The ac signals from CNT motion are incredibly small, but by using a near quantum limited amplifier (the TWPA described in Section 4.3) we are able to read these signals in a spectrum analyser. Unfortunately the TWPA amplifier has a working frequency from 4 - 7.5 GHz which is far beyond the normal mechanical frequencies of a CNT mechanical resonator which are generally in the MHz range (apart for a few exceptions [11]). This means any signal from the nanotube will

not be amplified by the TWPA, and actually blocked by the circulators on the MW readout lines.

Fortunately for us a CNT can be turned into a electromechanical mixer due to the non-linearity in its conductance [56]. CNT mechanical resonators are generally used as down-converters to convert the electromechanical signal from the CNT into the kHz range for detection via a lock in amplifier [56] [31] [57]. But in order to utilise the TWPA, we use the CNT as a up-converter mixer. An ideal mixer either up-converts or down-converts one frequency to another. A mixer has three signal components, a radio frequency (RF) input ω_{RF}, a local oscillator (LO) input ω_{LO}, and an intermediate frequency (IF) output. If the IF signal produced is at $\omega_{\mathrm{LO}} \pm \omega_{\mathrm{RF}}$ where $\omega_{\mathrm{LO}} > \omega_{\mathrm{RF}}$, then the mixer is an up-converter. If the IF signal produced is at $\omega_{\mathrm{RF}} \pm \omega_{\mathrm{LO}}$ where $\omega_{\mathrm{LO}} < \omega_{\mathrm{RF}}$ then the mixer is a down-converter. Our device is an up-converter and therefore will produce signals at $\omega_{\mathrm{LO}} \pm \omega_{\mathrm{RF}}$ as $\omega_{\mathrm{LO}} > \omega_{\mathrm{RF}}$.

The current through the device I is given by the conductance G and the bias voltage V_{SD}, where $I = GV_{\mathrm{SD}}$. The conductance and therefore the current is proportional to the induced charge on the CNT. The induced charge on the nanotube q_C is given by [56]:

$$q_c = C_{\mathrm{G}} V_{\mathrm{G}}^{\mathrm{ac}}(t) + V_{\mathrm{G}} C_{\mathrm{G}}^{\mathrm{ac}}(t) \tag{5.1}$$

This induced charge is formed of two terms. The first term is from the modulated gate electrode voltage at some frequency and is non-zero at any driving frequency. The second term comes from the mechanical oscillations of the CNT; as the CNTs displacement from the gate electrode changes, the capacitance also changes. This term is non-zero when the nanotube is driven on resonance, when the CNT oscillations are at their largest.

If we just send a drive frequency at ω_{RF} through the gate electrode, then the time-dependent conductance $G^{\mathrm{ac}}(t)$ is given by:

$$\begin{aligned} G^{\mathrm{ac}}(t) &= \frac{dG}{dV_{\mathrm{G}}} dV_{\mathrm{G}}(t) \\ &= \frac{dG}{dV_{\mathrm{G}}} (V_{\mathrm{G}}^{\mathrm{ac}}(t) + \frac{C_{\mathrm{G}}^{\mathrm{ac}}(t)}{C_{\mathrm{G}}} V_{\mathrm{G}}) \end{aligned} \tag{5.2}$$

where again the first term is from the modulated gate electrode, and the second

term ω_n is the frequency of motion of the CNT. The CNT motion interacts with the non-linearity in the conductance allowing us to use it as a mixer by applying another ac voltage to the source at a frequency ω_{MW}. The current through the device is then given by:

$$I_{\mathrm{mix}}(t) = G^{\mathrm{ac}}(t)V_{\mathrm{SD}}^{\mathrm{ac}}(t) \tag{5.3}$$

where $G^{\mathrm{ac}}(t) \propto \cos(\omega_{\mathrm{n}}t)$ and $V_{\mathrm{SD}}^{\mathrm{ac}}(t) \propto \cos(\omega_{\mathrm{MW}}t)$. Therefore in a simple case:

$$\begin{aligned} I_{\mathrm{mix}}(t) &\propto \cos(\omega_{\mathrm{n}}t)\cos(\omega_{\mathrm{MW}}t) \\ &\propto \frac{1}{2}\Big(\cos\Big((\omega_{\mathrm{MW}}-\omega_{\mathrm{n}})t\Big) + \cos\Big((\omega_{\mathrm{MW}}+\omega_{\mathrm{n}})t\Big)\Big) \end{aligned} \tag{5.4}$$

From Equation 5.4 we can see that the two frequencies are up-converted to two signals at $\omega_{\mathrm{MW}} + \omega_{\mathrm{n}}$ and another at $\omega_{\mathrm{MW}} - \omega_{\mathrm{n}}$. Therefore by picking a suitable frequency for ω_{MW} we can utilise the TWPA in amplifying any signals coming from the CNT. We chose a frequency of 5 GHz based on the results in §4.3 as this would place the mixed signal frequency around $5 \pm 0.26n$ GHz where $n \in \mathbb{N}$. This frequency range is well within the TWPA and MW readout frequency band. We now have a way of amplifying and measuring the CNTs motion.

In reality the mixer current is not as simple as described in Equation 5.4 due to interactions between the gate and source electrode. Therefore the bias voltage is given by:

$$V_{\mathrm{SD}}^{\mathrm{ac}}(t) = V_{\mathrm{SD}}^{\mathrm{dc}} + V_{\mathrm{SD},0}\cos(\omega_{\mathrm{MW}}t) + V_{\mathrm{SG},0}\cos(\theta_{RF}) \tag{5.5}$$

where $V_{\mathrm{SD}}^{\mathrm{dc}}$ is the dc bias voltage, $V_{\mathrm{SD},0}\cos(\omega_{\mathrm{MW}}t)$ is the MW probe tone contribution, and $V_{\mathrm{SG},0}\cos(\theta_{RF})$ is an asymmetric parasitic coupling between the gate electrode and source electrode. θ_{RF} is:

$$\theta_{\mathrm{RF}} = \omega_{\mathrm{RF}} + \phi_{\mathrm{RF}} \tag{5.6}$$

where ϕ_{RF} is the phase of the parasitic coupling. The conductance $G^{\mathrm{ac}}(t)$ depends on the displacement of the CNT, and therefore (in a similar fashion to Equation 2.52)

Go to Contents

can be given by:

$$\begin{aligned} G^{\mathrm{ac}}(t) &= G_0 + G'u(t) + \frac{1}{2}G''u(t) + \dots \\ &= G_0 + G'u_0\cos(\theta_n) + \frac{1}{4}G''u_0^2(1+\cos(2\theta_n)) + \dots \end{aligned} \tag{5.7}$$

where $u(t) = u_0\cos(\theta_n)$, and $\theta_n = \omega_n t + \phi_n$ where ϕ_n is the phase of the CNT motion. Combining together Equation 5.5 and 5.7 into Equation 5.3 gives:

$$\begin{aligned} I_{\mathrm{mix}}(t) = {} & G_0V_{\mathrm{SD}}^{\mathrm{dc}} + G_0V_{\mathrm{SD},0}\cos(\omega_{\mathrm{probe}}t) + G_0V_{\mathrm{SG},0}\cos(\theta_{RF}) \\ & + G'u_0\cos(\theta_n)V_{\mathrm{SD}}^{\mathrm{dc}} + G'u_0\cos(\theta_n)V_{\mathrm{SD},0}\cos(\omega_{\mathrm{probe}}t) \\ & + G'u_0\cos(\theta_n)V_{\mathrm{SG},0}\cos(\theta_{RF}) \\ & + \frac{1}{4}G''u_0^2(1+\cos(2\theta_n))V_{\mathrm{SD}}^{\mathrm{dc}} + \frac{1}{4}G''u_0^2(1+\cos(2\theta_n))V_{\mathrm{SD},0}\cos(\omega_{\mathrm{probe}}t) \\ & + \frac{1}{4}G''u_0^2(1+\cos(2\theta_n))V_{\mathrm{SG},0}\cos(\theta_{RF}) \\ & + \dots \end{aligned} \tag{5.8}$$

Excluding components that do not depend on displacement, there are dc components:

$$\begin{aligned} I_{\mathrm{mix}}^{dc} = {} & \frac{G''u_0^2V_{\mathrm{SD}}^{\mathrm{dc}}}{4} \\ & + G'u_0V_{\mathrm{SG},0}\langle\cos(\theta_n)\cos(\theta_{RF})\rangle \\ & + \frac{G''u_0^2V_{\mathrm{SG},0}}{4}\langle\cos(2\theta_n)\cos(\theta_{RF})\rangle \\ & + \dots \end{aligned} \tag{5.9}$$

where when $\theta_{RF} = \theta_n, 2\theta_n \dots$ extra dc components will be produced independent of gate voltage. And there are ac components, most of which are blocked by the circulators (as discussed in §4.2), given by:

$$\begin{aligned} I_{\mathrm{mix}}^{ac}(t) = {} & G'u_0V_{\mathrm{SD},0}\cos(\theta_n)\cos(\omega_{\mathrm{probe}}t) \\ & + \frac{1}{4}G''u_0^2V_{\mathrm{SD},0}\cos(2\theta_n)\cos(\omega_{\mathrm{probe}}t) \\ & + \dots \end{aligned} \tag{5.10}$$

Go to Contents

Therefore if $\phi_n = 0$, we are left with Equation 5.4 but with extra electrical overtones at integer multiples of the frequency of motion (signals at $\omega_{\mathrm{MW}} \pm \omega_n$, $\omega_{\mathrm{MW}} \pm 2\omega_n$, and so on).

5.1 Setup

In order to turn the CNT into an electromechanical mixer, the rectification circuitry shown in Figure 2.10 was altered for ac signals to be measured via a spectrum analyser and the TWPA. The circuitry builds on top of the rectification circuit connecting a bias tee to the source of the device, and then adding a MW signal generator to that line providing a small ac voltage to the bias voltage. The circuit is also adapted to use the TWPA by adding a pump line to the circuit after the device. This new circuit is shown in Figure 5.1; In the following section superscript numbers linked to the component numbers of Table 5.1.

Due to a lack of foresight when fabricating the device, we needed to add a series of cancelling lines to destructively interfere with leaked signals. This is because we have another non-linear device in the circuit, the TWPA, which also can act as an RF mixer. It was found that the TWPA was mixing the leakage of the RF and MW tones to produce a signal where the mechanical signals should be; this signal did not respond to any gate voltage or bias voltage change which confirmed it wasn't from the CNT. The leakage of the RF and MW tones are due to the construction of the device and the high impedance of the CNT. As the source, drain, and gate electrodes are all long parallel strips of metal there is significant capacitive and inductive cross-talk between them. Combining this with the high impedance of the CNT, which reduce the tranmission anyway, it is clear that only a small amount will be mixed in the CNT and more signal from the cross-talk will be mixed in the TWPA. The cancelling lines act to cancel these leakage signals before they can enter the TWPA.

In hindsight adding a cryogenic high pass filter for the RF leakage and a bandstop for the MW leakage between the device and the amplifier would have made the circuitry simpler but this would require a whole device overhaul to add the bandstop, warming up of the Triton dilution refrigerator to add the filters, and redoing all the initial

Go to Contents

characterization tests of the device all of which are time consuming. The MW leakage could be cancelled with a filter too which could have saved on fabrication time, but since the mixed signal is relatively close to the MW frequency, finding a filter that blocks the MW leakage without interfering with the mixed signal could prove difficult.

The drive power necessary to get a parametric response is much higher than one needed to get a fundamental response using the electromechanical mixer setup. At lower powers the RF and MW cancelling can be 'tuned' to cancel the RF and MW power leakage before the starting the measurement and then left alone for the whole measurement. Unfortunately high RF drive powers are needed to get a parametric response from the CNT harmonics as shown in Figure 6.8 and therefore a more 'active' cancelling was required on both the cancelling circuits to stop mixing of the leaked powers in the TWPA. To actively cancel the RF drive, a calibration dataset is used to cancel the leaked RF power for each drive frequency using a phase shifter, a digital attenuator, and a RF amplifier. The MW cancelling required a Python script constantly working behind the scenes while running the measurement as the wavelength of the MW probe tone (around 4 cm) made it sensitive to the Teflon knee of our cables. This meant the MW cancelling was sensitive to fluctuations in the room temperature even with an air conditioning unit keeping the room to $20 \pm 1°C$. This would cause the cancelling to move off phase, allowing more power to leak through to the TWPA. The Teflon knee is a common phenomenon found in Teflon coated RF cables where around 19°C expansion of the Telfon causes a change in dielectric constant which causes a change in phase. In our MW probe tone this causes a change in phase of 3° which is more than enough to cause the MW leakage power to worsen. To deal with this constantly changing phase of the MW cables two changes were made; phase stable cables were used in the MW probe tone arm and the MW cancelling arm in order to try and minimise any phase change from room temperature fluctuations, and another spectrum analyser was added to the setup to measure the MW power leakage and then used to adjust the amplifier and attenuator in the MW cancelling circuit. Unfortunately the phase stable cables were not enough on their own to deal with the fluctuating phase as the devices and various adapters in the circuit were still susceptible to the room temperature fluctuations.

Go to Contents

The cancelling setup is explained further in Appendix D.

Like in the rectification circuit, a RF signal generator is connected to the gate electrode through a bias tee to drive the CNT. The RF signal is generated by a Rohde & Schwarz SMBV100A[1] signal generator. The signal is then split into 2 signals, an RF cancel line and an RF drive line, by a Mini-Circuits ZESC-2-11+ power splitter[2]. Following the RF drive line, the line is first attenuated by 10dB to match the power between the RF drive and RF cancel lines. The line is then attenuated again by cryogenic attenuators which are shown in Figure 4.3; the attenuation shown in Figure 5.1 shows the cumulative sum of the attenuators on the pulse line the RF drive line is connected to. Lastly the RF drive line passes through a bias tee connected to the device gate electrode and a dc gate voltage supplied by a low noise voltage source module from a QuTech IVVI-DAC2. Following the RF cancel line, there is a phase shifter designed by Edward Laird[3][58], a Vaunix LDA-602 Digital Attenuator[4], and a Mini-Circuits ZX60-33-LN-s+ amplifier[5]. The phase shifter is controlled by a Keithley 2450 SMU which is controlled by a PC. The mini-circuits amplifier is ran at its typical dc supply voltage of 5 V supplied by a Keysight E3630A dc Power Supply. The power through the RF cancel line is matched to the RF drive line by changing the attenuation of the variable attenuator. The RF Cancel line is attached to the TWPA pump line using a Pasternack PE2210-10 directional coupler[6].

Similar to the RF lines, the MW probe tone is connected to the source electrode through a bias tee. The MW signal is generated by a Rigol DSG3136B signal generator[7]. The signal is then split into 2 signals, an MW probe line and a MW cancel line, by a Mini-Circuits ZFRSC-183-S+ power splitter[8]. Following the MW probe line, it is connected straight to the RF drive line into the cyrostat. The attenuation shown in the cumulative sum of all the attenuators on the RF drive line the MW probe line is connected to. The MW probe line is then connected to a bias tee connected to the source of the device and a dc bias voltage supplied by a low noise voltage source module from a QuTech IVVI-DAC2. Following the MW cancel line, the line is then split again by a Mini-Circuits ZFRSC-183-S+ power splitter[8] with one side going to a Vaunix LPS-802 phase shifter and the other going to a Vaunix LDA-802EH digital attenuator. The two sides are then combined

Go to Contents

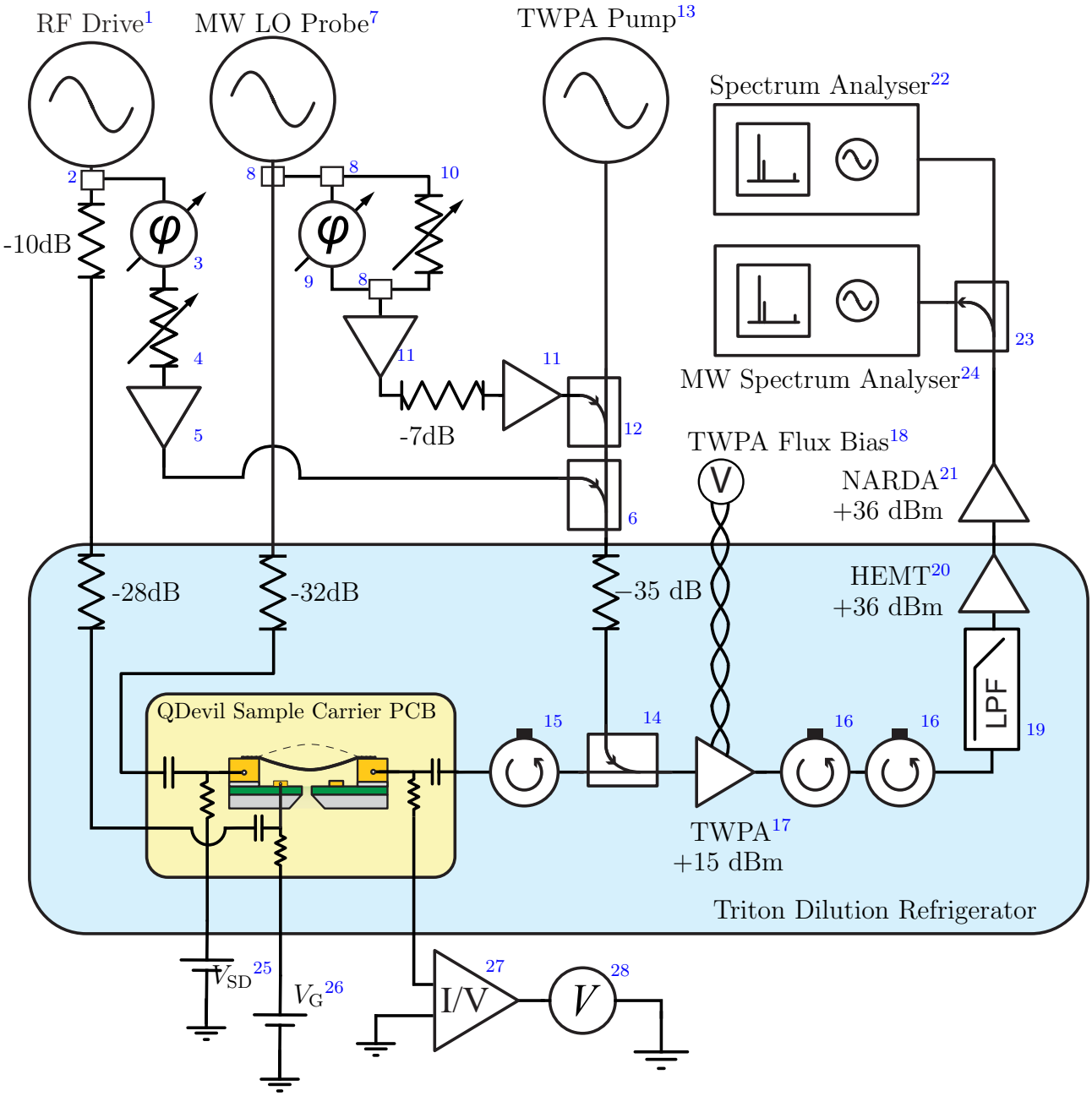

Figure 5.1: The circuitry needed to turn the device into a mixer for time-dependent measurements needed to tell the difference between directly driven and parametrically driven resonances in the CNT. By sending a 5 GHz signal through the source drain and a RF driving frequency through the gate, the two frequencies are mixed together, due to the non-linearity in the nanotubes conductance, producing a signal at $f_{MW} \pm f_{IF}$. Any signal is then amplified by the TWPA and read by the spectrum analyser giving us time-dependent signals. At high RF and MW powers cancellation circuits are needed to stop mixing of leakage frequencies into the TWPA which would obscure signals from the CNT. The second spectrum analyser is needed to adjust the MW cancellation on the fly as the cabling is effected by the Telfon knee which affects the phase at $\sim 19°C$.

Go to Contents

Component Number	Model	Powered by
1	Rohde & Schwarz SMBV100A	N/A
2	Mini-Circuits ZESC-2-11+	N/A
3	Custom Phase Shifter[1]	Keithley 2450 SMU
4	Vaunix LDA-102	N/A
5	Mini-Circuits ZX60-33-LN-S+	Keysight E3630A dc Power Supply
6	Pasternack PE2210-10	N/A
7	Rigol DSG3136B	N/A
8	Mini-Circuits ZFRSC-183-S+	N/A
9	Vaunix LPS-802	N/A
10	Vaunix LDA-802EH	N/A
11	Mini-Circuits ZX60-24A-S+	Keysight E3630A dc Power Supply Keithley 2450 SMU
12	Krytar 120420	N/A
13	Windfreak SynthHD	N/A
14	Krytar 120420	N/A
15	LNF-CIC4-12A	N/A
16	LNF-CICIC4-12A	N/A
17	TWPA	Flux Bias[18] and TWPA Pump[13]
18	Battery Powered Voltage Source at 819μA	
19	Marki Microwave FLP-0750 7.5 GHz Lowpass	N/A
20	LNF-LNC0.3 14A HEMT	
21	Narda LNA-30-04001200-15-10P	Keysight E3630A dc Power Supply
22	Rohde & Schwarz FSV3044	N/A
23	Pasternack PE2210-20	N/A
24	Rigol DSA875	N/A
25	QuTech IVVI-DAC2	N/A
26	QuTech IVVI-DAC2	N/A
27	QuTech IVVI-DAC2	N/A
28	Keithley 2100	N/A

Table 5.1: Part list of the rectification and electromechanical mixer technique.

Go to Contents

with another Mini-Circuits ZFRSC-183-S+ power splitter[8]. This setup allows finer control of the phase of the MW cancelling line [59]. This is necessary to deal with the small wavelength of the MW signal. The combined signal is then passed through two Mini-Circuits ZX60-24A-S+ MW amplifiers[11] and a 7 dB attenuator. One of the amplifiers is controlled by a Keysight E3630A dc Power Supply running at its typical operating voltage of 5 V, and the other is powered by a Keithley 2450 SMU. The amplifier powered by the Keithley controls the gain through MW cancel line by unconventionally running the amplifier at a untypical supply voltage. In theory this should be replaced with a proper variable gain amplifier or an amp-attenuator setup like on the RF cancel line. The MW cancel line is then attached to the TWPA pump line using a Krytar 120420 cryogenic directional coupler[12] before the RF cancel line. The MW coupler must come before the RF coupler because the transmission loss of MHz signals through the Krytar is quite large.

The TWPA pump signal is provided by a Windfreak SynthHD operating at 12 GHz at -2.6 dBm. The TWPA pump signal passes through the RF and MW coupler, and then down into the dilution refrigerator using the TWPA pump line described in Figure 4.3. The attenuation shown in Figure 5.1 is a cumulation of all the attenuators on the TWPA pump line. The TWPA pump line then joins the MW readout via a Krytar 120420 cryogenic directional coupler[14]. The magnetic flux bias of the TWPA is controlled via a battery powered voltage source to a current of 819 μA.

The readout for the device has two components, a dc part and an ac part. The readout signals are split by a bias tee. The dc part is measured by a transimpedance amplifier and a Keithley 2100 multimeter as described already in the rectification technique (Figure 2.10). The ac part is taken up the MW readout line. From the drain of the device, there is a LNF-CIC4-12A circulator[15], the TWPA coupler[14], a LNF-CICIC4-12A dual circulator[16], and a Marki Microwave FLP-0750 7.5 GHz low pass filter[19]. The signal is then amplified by a low noise factory LNF-LNC0.3 14A HEMT[20] on the 4 K stage, and then amplified again by a Narda LNA-30-04001200-15-10P[21] room temperature amplifier powered by the Keysight E3630A dc power supply at 15 V. The Narda amplifier gain was affected by fluctuations in the room temperature so a cooler was designed to keep the amplifier at a more stable temperature. From the NARDA amp, the signal is split in two by a Pasternack PE2210-20

Go to Contents

directional coupler[23]. The coupled port with 20 dB attenuation is connected to a Rigol DSA875 spectrum analyser [24]. The Rigol spectrum analyser is used to measure the power leakage of the MW probe tone. The out port of the coupler is connected to a Rohde & Schwarz FSV3044 spectrum analyser. The Rohde & Schwarz spectrum analyser measures the electromechanical signals from the device.

5.2 Setup Parameters

This section describes how the bias voltage, gate voltage, RF power, and MW power were found. As the circuit incorporates two different techniques, we had to find parameters that best caused parametric resonances to appear. For the case of the rectification method, we are interested in areas where d^2I/dV_G^2 is the highest, whereas for the mixer we are interested in areas where dG/dV_G is highest. d^2I/dV_G^2 will be highest at the peaks and troughs of the Coulomb peaks whereas dG/dV_G will be highest on the flanks of the Coulomb peaks. This generally means for the the rectification method we are looking for areas with the highest Coulomb peaks but for the electromechanical method we are looking for areas with the sharpest peaks. When searching for mechanical modes this can lead to a difference in signal strength between the rectification technique and the electromechanical technique.

To find the best bias voltage, we performed a stability diagram of the device by sweeping both gate voltage and bias voltage while measuring the current which is shown in Figure 5.2 (a). The device shows no current flow on bias voltages between ~ -6 mV to ~ 6 mV. Coulomb diamonds appear around 7 mV therefore a bias voltage of $7 - 9$ mV would give the best signals. There is no current flow on gate voltages above ~ -3 V. There is a region of interest with gate voltages from 7 V to -9 V. Therefore using gate voltages in this region will be the most likely place to see mechanical resonances. By taking a look at the differential of dG/dV_G around this region,a good response from the electromechanical mixer will be around -8.5 V.

To find the best gate voltage, we take a trace from the stability diagram at a fixed bias voltage of 9 mV. These results are shown in Figure 5.2 (a). Again they show that the best gate voltage regions will be around -7 V to -9 V. By taking the differential dG/dV_G we again see that the best region should be around -7 V to

Go to Contents

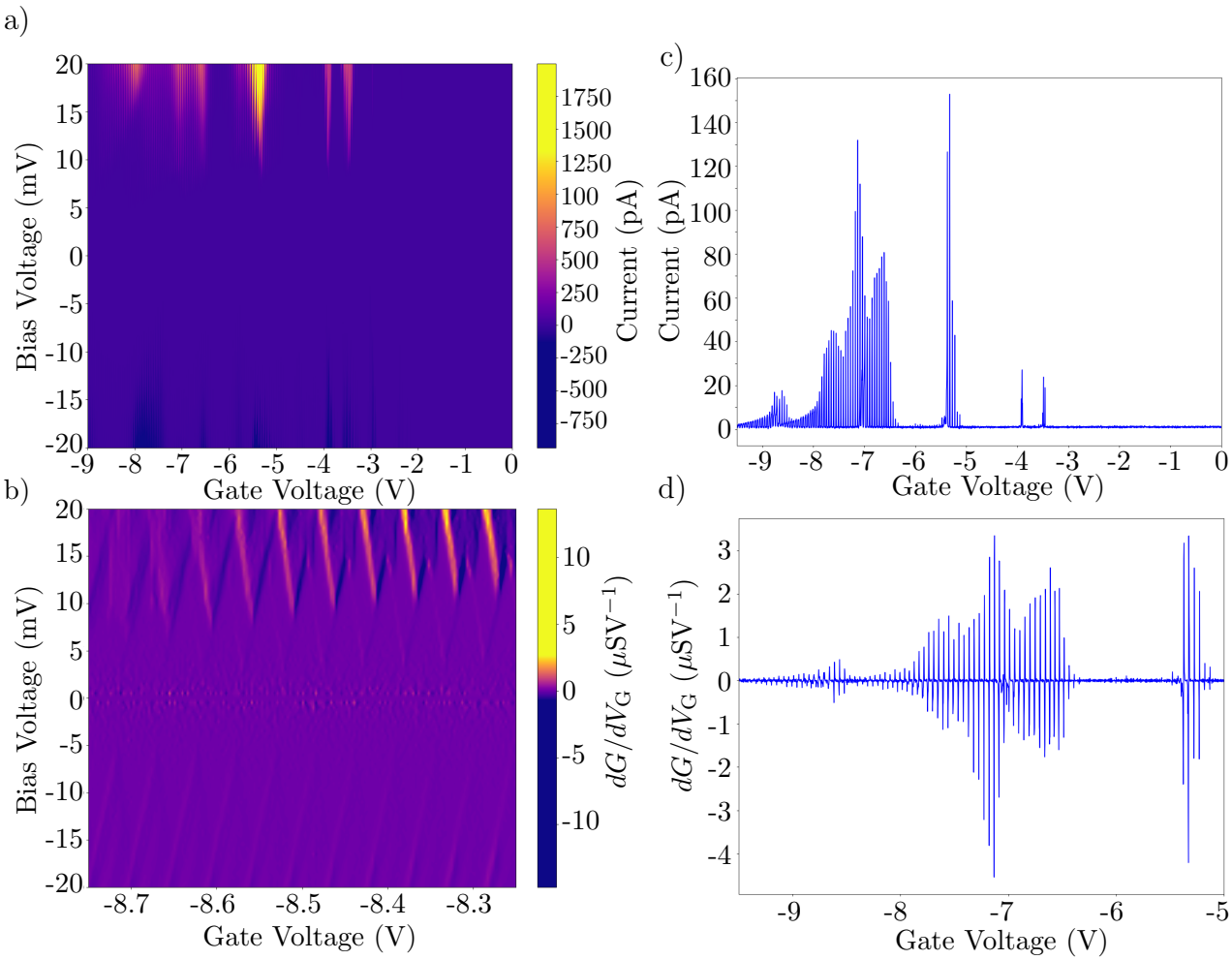

Figure 5.2: a) shows the stability diagram of the device. Coulomb diamonds appear at gate voltages lower than −3 V, with a larger region of diamonds around −7 V, and appear at bias voltages above 6 mV and below −6 mV. The diamonds are not symmetric between positive and negative bias voltages probably due to the tunnel junction width not being consistent between bias voltages. (b) shows differential conductance of the CNT between gate voltages of −8.75 to −8.25 V, and bias voltages from 20 mV to −20 mV. There are strong regions of conductance around −8.4 V over a few Coulomb diamonds. (c) shows the current over a range of gate voltages from 0 V to −9 V with the bias voltage set to 9 mV. The strongest current peaks are around −5.3 V. There are larger regions of current peaks between −6.5 V to −9 V. (d) shows the differential conductance of the CNT over a range of gate voltages from 0 V to −9 V with the bias set to 9 mV. The strongest transconductance again is around −5.3 V. There is a large region of slightly smaller differential conductance peaks from −6.5 V to −8.6 V.

Go to Contents

−9 V.

All RF and MW powers stated are the powers that enter the top of the dilution refrigerator so that the results of electromechanical mixer technique are comparable to the results of the rectification technique.

To find the best parameters for the MW probe tone, we first need to find the mechanical resonances of the CNT using the rectification part of the setup using a bias of 9 mV and a gate of ~ 7 V. A number of mechanical resonances were found by performing a large frequency sweep across a small gate voltage. The resonances used in this thesis were found at frequencies around 260 MHz, 525 MHz, and 795 MHz. Faint resonances appear at 130 MHz and 65 MHz at very high drive powers [40]. Since the resonance around 260 MHz had the best response to drive power and shows no response while scanning at half the drive frequency (Figure 5.3), we are confident this is the fundamental frequency of the device. Interestingly 'twin' resonances appear at each harmonic. These are from the CNT having two degrees of freedom (oscillations parallel to the gate electrode, and another perpendicular to the gate electrode) and has been observed by other groups [60].

Finding the best RF and MW power required sweeping of both parameters to finally settle on the correct powers. Earlier in the chapter the frequency of the MW probe tone was set to 5 GHz to utilise the TWPA, next we needed to work out the MW power of the probe tone. Using a gate voltage of −8490 mV, and an RF power of −25 dBm, by sweeping frequency and MW power around one of the fundamental modes we can see how the MW power affects the electromechanical signal. We should expect that as the power of the MW probe tone increases, the signal of the resonance should also increase as the mixed signal should be proportional to the amplitude of the MW probe tones (From Equation 5.4), however at high MW probe powers the device temperature will increase reducing the SNR. Figure 5.4 shows these results. Clearly as the microwave power is increased, so does the resonance power. For example at −15 dBm MW probe power, the signal at 260.5 MHz is $\sim$ −86 dBm whereas at −25 dBm, the signal at 260.5 MHz is $\sim$ −92.5 dBm. As expected the background noise level also increased as the MW probe power was increased; this is best seen in Figure B.1. For example at −20 dBm probe power, the

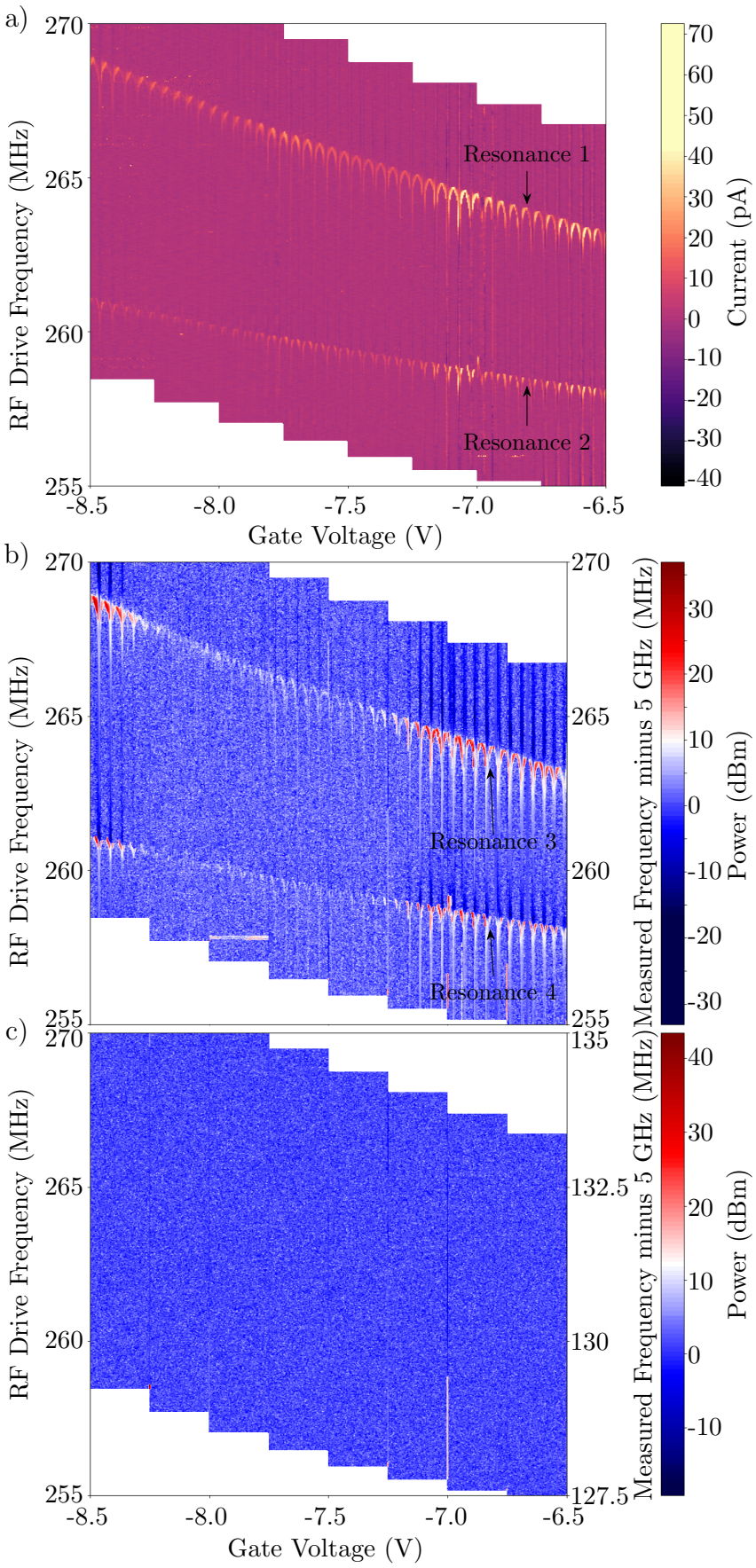

Figure 5.3

Frequency Gate sweeps of the fundamental using the rectification technique and the electromechanical mixer technique with the column average subtracted from each column in order to remove the Coulomb peaks. The parameters used for all panels were a bias voltage of 9 mV, an RF drive power of −10 dBm, and a MW probe tone frequency of 5 GHz and power of −15 dBm. (a) shows the results from the rectification technique; the twin resonances show a quadratic dependence with the gate voltage and show the spring softening of the CNT around the Coulomb peaks. (b) shows the results from the electromechanical technique while scanning at 5.260 GHz; the twin resonances show a quadratic dependence with the gate voltage and show the spring softening of the CNT around the Coulomb peaks which is the same as in the rectification method. (c) shows the results from the electromechanical technique while scanning at 5.130 GHz. If there are any parametric resonances then scanning at this frequency should show them, however there are no resonances shown which indicates the pair of resonances we see around 260 MHz are the fundamental frequency. Resonances have been fitted to Equation 6.1 and parameters are shown in Table 6.1.

Go to Contents

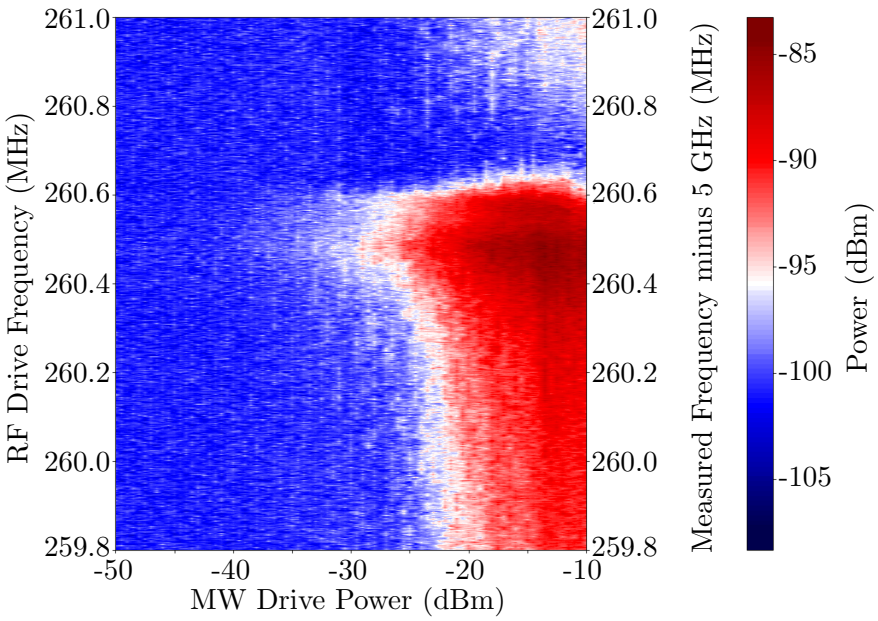

Figure 5.4: Testing the MW power in the mixer at an RF drive of −25 dBm, bias voltage of 9 mV, and a gate voltage of −8490 mV. At ∼ −30 dBm the resonance signal in the electromechanical mixer becomes strong. At higher powers the resonance signal becomes stronger in the electromechanical mixer but the noise floor also increases possibly due to heating of the CNT. This is better seen in Figure B.1.

measured current at 260.8 MHz is around 10 pA whereas at −15 dBm probe power, the measured current at 260.8 MHz is around 20 pA. A probe power of −15 dBm was chosen although in hindsight a power of around −20 dBm would have given similar results without the arduous challenge of trying to cancel the higher power MW leakage.

Finding the best RF power started by using high RF powers (∼ 3 dBm) and slowly reducing this to try and find a power than produced an linear response from the CNT electromechanical resonator. This was to try and get the best quality factor from the electromechanical mixer technique as higher quality factors have the highest sensitivity. Figure 5.5 (a) and (b) shows a comparison of the fundamental response of the CNT resonator in the electromechanical mixer technique (a) and the rectification technique (b). The parameters used in the figure were a bias voltage of 9 mV, a gate voltage of −8514 mV, a probe tone power of −15 dBm, and probe frequency of 5 GHz. In both methods, the CNT resonator is in a non-linear regime as the signal seems to be being pushed over to one side (or duffed), however clearly the signal in the mixer technique is stronger than the signal in the rectification technique as the

signal to noise ratio (SNR) of the electromechanical mixer technique is 32.4 whereas the rectification technique has a SNR of 1.6. The SNR was calculated via:

$$\mathrm{SNR} = \frac{\mathrm{Power}_{\mathrm{max}} - \overline{\mathrm{Noise}}}{\mathrm{Power}_{\mathrm{range}}} \tag{5.11}$$

The lower SNR in the rectification technique is due to the high noise range of 5 pA and the low signal height of 11 pA. The mixer technique has a noise range that is higher than the rectification technique of 18 pW but has a significantly higher signal height of 586 pW. Figure 6.7 also shows the electromechanical technique being more sensitive than the rectification technique. For this figure, the same parameters as Figure 5.5 were used. It shows that the fundamental resonance using the rectification technique appears around −34 dBm drive power, whereas in the electromechanical technique the fundamental resonance appears at a much lower power of −65 dBm; 2.1 orders of magnitude lower than in the rectification method. The best quality factor using the electromechanical mixer technique is shown in Figure 5.5 (c) while being driven at a power of −54 dBm. The quality factor is ∼ 20,000 which is much lower than the $\sim 203,300$ [40] measured by Patrick Steger on the same device earlier albeit at different parameters and on the higher twin mode of the fundamental resonance. An RF power of −54 dBm was not used for the frequency-gate sweeps as the parametric resonances only appeared above −32 dBm. This unfortunately meant the nanotube would be susceptible to Coulomb broadening.

Figure 5.6 shows at high RF powers the Coulomb peaks are broadened which affects signal strength. The settings used in Figure 5.6 are a 9 mV bias, and a MW probe tone frequency of 5 GHz and power of −15 dBm. (a) shows the rectification technique results and nicely shows the Coulomb peaks and how they widen at high RF powers. It shows that the Coulomb peak widens as the RF power is increase as the width of the peak increases from 9 mV at −50 dBm to 11 mV at 0 dBm using the peak located around −8.507 V. (b) shows the pure electrical mixing at very high RF drive powers. If we recall Equation 5.1, then $V_G^{\mathrm{ac}}(t)$ is no longer negligible, and creates a mixer current independent of the CNT motion. The mixer results show that the Coulomb peak begins at around −35 dBm and then gets broader as the RF increases. At −20 dBm using the peak around −8.507 V for example the width

Go to Contents

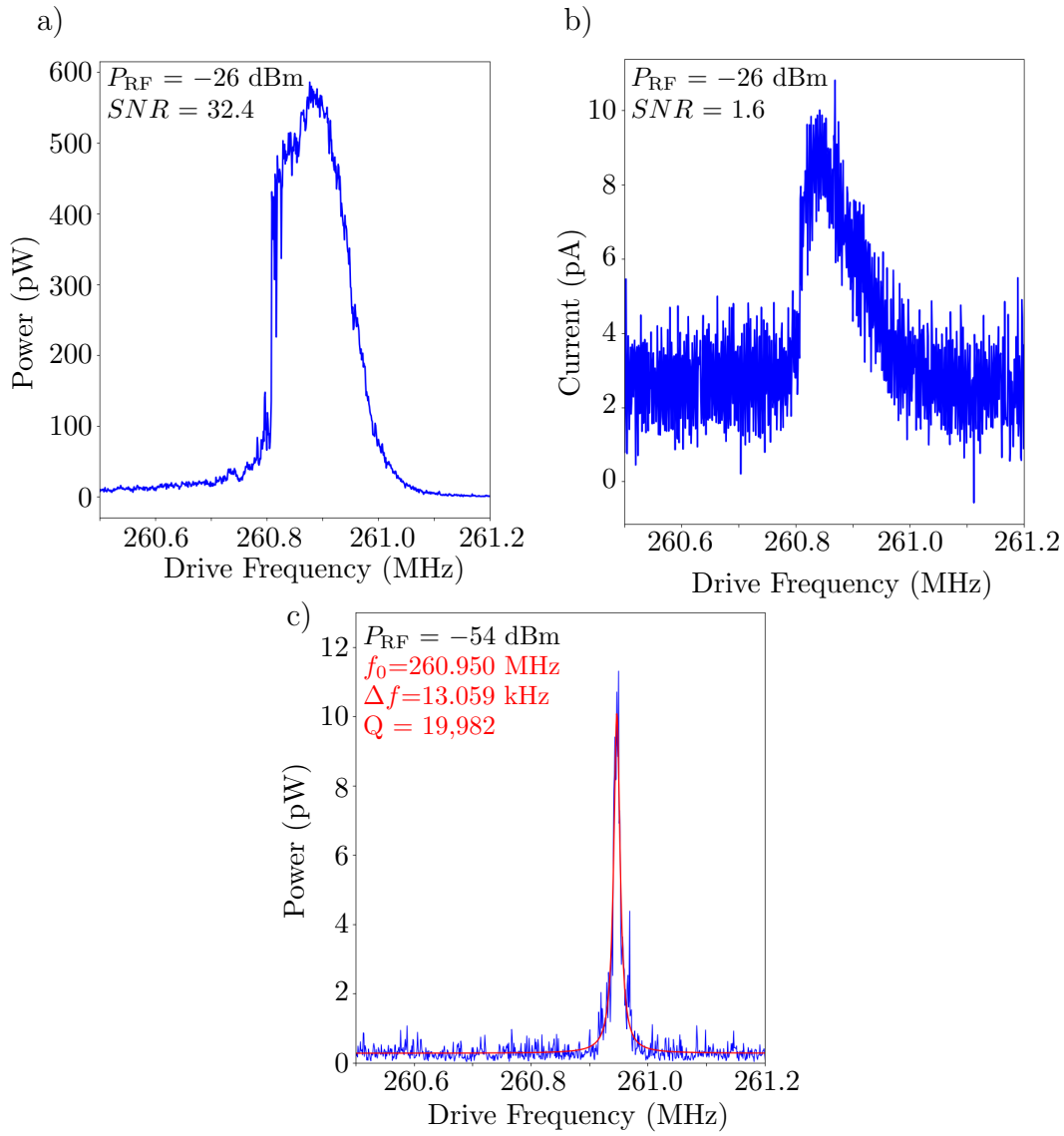

Figure 5.5: Output power/current from the CNT mechanical resonator. For all measurements, the bias voltage is 9 mV, the gate voltage is −8514 mV, the microwave probe tone power is −15 dBm, and the microwave probe tone frequency is 5 GHz. The drive frequency is swept across the mechanical resonance and the power/current is measured from the spectrum analyser or multimeter respectively. (a) shows the electromechanical technique through the spectrum analyser with an RF drive power of −26 dBm. (b) shows the electromechanical signal measured using the rectification technique through the multimeter with an RF drive power of −26 dBm. The mixer has a far greater sensitivity than the rectification technique. The signal to noise ratio (SNR) is far higher for the mixer technique than the rectification technique. (c) shows the mechanical resonator driven at a lower power such that the resonance fits a Lorentzian fit with a full width half maximum Δf of 13.059 kHz and a centre frequency f_0 of 260.95 MHz. The quality factor Q is $19,982$ where $Q = f_0/\Delta f$.

Go to Contents

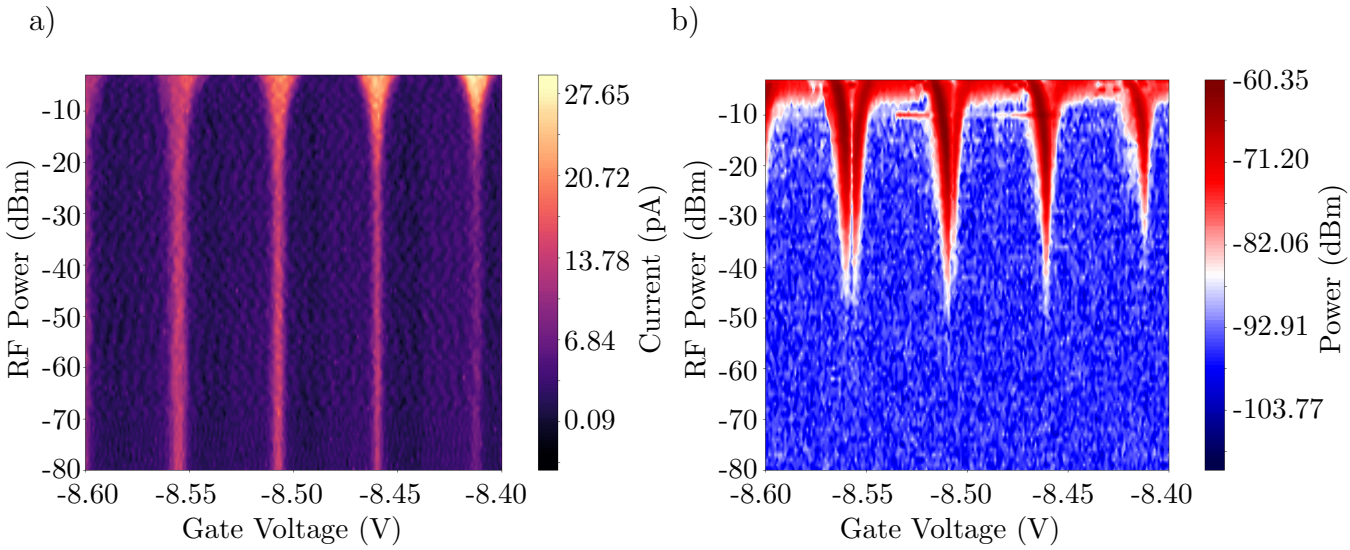

Figure 5.6: The broadening of the Coulomb peak with RF power. Parameters used were a 9 mV bias, an RF drive frequency of 265 MHz, and a MW probe tone power of −15 dBm; the RF drive frequency is off resonance for this gate voltage. (a) shows the rectification technique results. The Coulomb peaks were measured by altering the drive power over a set gate voltage range. It shows that the Coulomb peak starts to broaden around −10 dBm. As the peak broadens in (a), the current through the device should decrease but in our device the current increases as the drive power increases. (b) shows the electromechanical mixer technique results. By driving the nanotube off resonance we should not see any features. However as the drive power increases, features in the electromechanical mixer technique appear. The features are the result of the RF drive cross-talking with the drain electrode or non-linearities in the conductance which then mixes with the MW probe tone producing a purely electrically mixed signal. This signal appears around −35 dBm.

of the Coulomb peak is 9 mV whereas at 0 dBm the width is 19 mV. This broadening of the Coulomb peak reduces the steepness of the peak. Since the gradient is dG/dV_G and the mixer signal power depends on dG/dV_G, at RF powers where the peak is broadened, the measured mixer signal power will be less than expected. The results shown in Figure 5.6 (a) do not show the amplitude of the Coulomb peak decreasing with RF power, but the results in Figure 5.6 (b) show the electrical mixing overcoming the electromechanical mixing.

Go to Contents

Chapter 6

Parametric Detection and Confirmation Using An Electromechanical Mixer

In this chapter, I will highlight how the electromechanical mixer technique can be used to detect parametric resonances as well as methods confirming that the resonances we see are in fact parametrically driven rather than directly driven. We will be looking at the modes around the first and second harmonic of the CNT mechanical oscillator which are around 520 MHz and 780 MHz respectively. There should be four modes around the first Harmonic, two directly driven and two parametrically driven. Only the first harmonic will be used for confirming that the resonances we see are in fact parametric and not directly driven.

6.1 Frequency-Gate Scans

As discussed in §3, the most effective way to drive the fundamental resonance parametrically is when the drive frequency is twice that of the fundamental. Using the circuit described in the previous chapter, we can measure using the rectification technique and the electromechanical mixer technique. For these results we will produce three panels (a,b,c) of frequency vs gate voltage sweeps, (a) using the rectification method, (b) using the electromechanical mixer while scanning around

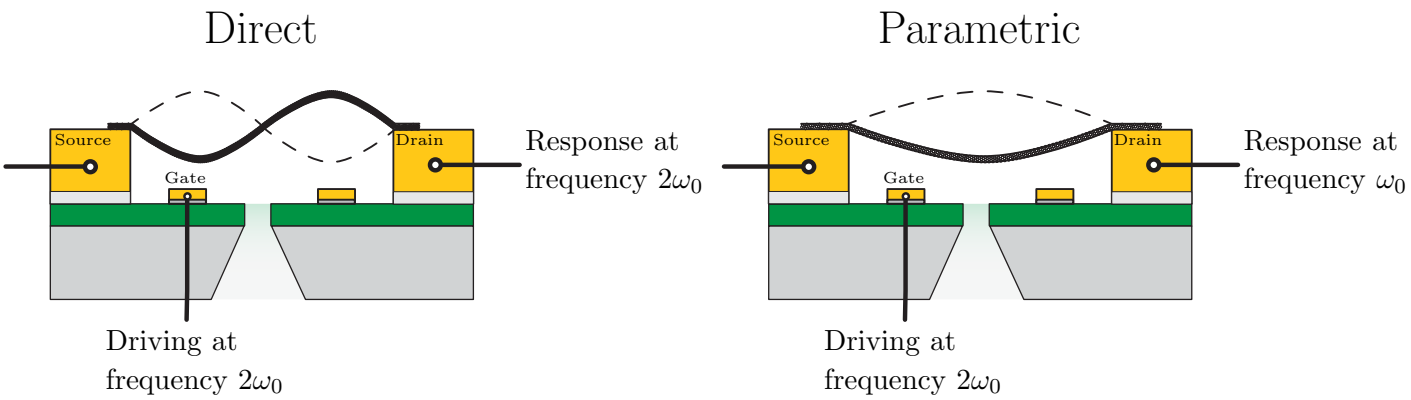

Figure 6.1: Demonstration of the difference between directly driving and parametrically driving the CNT. In direct driving, driving at the resonant frequency produces a response at the same frequency whereas in parametric driving, driving at twice the resonant frequency parametrically drives the fundamental producing a response at half the frequency.

the drive frequency plus 5 GHz, and (c) using the electromechanical mixer while scanning around half the drive frequency plus 5 GHz.

Assuming we are scanning around the first harmonic, the rectification technique panel (a) should show four resonances, two directly driven (due to the CNTs two degrees of freedom) and two parametrically driven. In the first electromechanical mixer panel (b) scanning at 5 GHz plus the drive frequency, we expect to see four resonances that match the rectification technique results. In the final electromechanical mixer panel (c) we should only see two resonances which match some of the resonances in (a) and (b). The two resonances appearing in (c) at subharmonics of the drive frequency is evidence of parametric motion in the CNT.

In the first electromechanical results (b), the reason why the parametric resonances of the fundamental appear at these frequencies in the electromechanical mixer can be explained using Equation 5.10 and 5.9. The effective voltage generated by the CNTs motion interacts with its conductance producing measurable signals at integer multiples of the frequency of motion. In practice, only the first few resonances appear as the signal strength decreases rapidly but this heavily depends on the conductance (G'' might be greater than G' for example).

To confirm that all the resonances seen are not cable resonances we should see that the resonances depend on gate voltage when we perform a long range gate voltage vs frequency measurement. This relationship should be quadratic from Equation 2.50

Go to Contents

and generally fits well to this equation from §2.3.2:

$$f_i(V_G) = a_i(V_G - V_{0,i})^2 + f_{0,i} \tag{6.1}$$

where f_i is the frequency of the ith resonance, a_i is a constant of the ith resonance, V_G is the gate voltage, $V_{0,i}$ is the voltage offset of the ith resonance, and $f_{0,i}$ is the frequency offset of the ith resonance. The presence of $V_{0,i}$ is due to static charges on the substrate which causes an offset in the gate voltage. This has already been observed by N. Hüttner et al. [42]. A resonance following this relation confirms they are not cable resonances. Furthermore we can confirm that the results are from electromechanical motion by looking for spring softening of the resonances around the Coulomb peaks as explained in §2.3.2.

6.2 Quadratic Curve Ratios

In §2.3.1 the equation that described the CNT harmonic frequencies given by:

$$\omega_n = 2\pi \frac{n+1}{2L} \sqrt{\frac{T}{\rho A}} \tag{6.2}$$

However in reality, our approximation of bending rigidity not having any effect on the CNT is an approximation, and the bending rigidity does have some effect on the frequencies. Therefore the frequencies of the harmonics should be higher than expected as the bending rigidity resists the motion of the CNT. Comparing the ratio, R, given by:

$$R = \frac{\omega_n}{n\omega_0} \tag{6.3}$$

where ω_n is the frequency of the nth harmonic, n is the harmonic number, and ω_0 is the fundamental frequency, between the nth harmonic and the fundamental should produce a value of R greater than one. However as parametric resonances are resonances of a lower harmonic, the ratio R between the fundamental and the fundamental being parametrically driven should be exactly one.

Go to Contents

Resonance #	Drive Type	Technique	$f_{0,i}$ (MHz)	$V_{0,i}$ (V)	a_i (kHz/V^2)
1	Direct	Rectification	260.34 ± 0.46	-3.84 ± 0.32	390.31 ± 34.39
2	Direct	Rectification	256.15 ± 0.68	-3.13 ± 0.95	165.34 ± 36.21
3	Direct	Mixer	257.66 ± 1.49	-1.84 ± 1.07	248.81 ± 47.23
4	Direct	Mixer	255.21 ± 1.53	-2.03 ± 2.05	137.45 ± 51.05
5	Parametric	Rectification	517.80 ± 2.91	-2.59 ± 1.09	548.62 ± 119.80
6	Direct	Rectification	523.37 ± 0.08	-5.70 ± 0.06	825.72 ± 24.14
7	Direct	Rectification	521.64 ± 0.04	-6.43 ± 0.03	1092.96 ± 30.48
8	Parametric	Rectification	503.00 ± 19.33	2.99 ± 12.46	145.02 ± 168.27
9	Parametric	Mixer	522.78 ± 8.32	-4.55 ± 2.94	929.35 ± 843.80
10	Direct	Mixer	523.25 ± 0.20	-5.70 ± 0.15	815.47 ± 59.40
11	Direct	Mixer	521.51 ± 0.04	-6.61 ± 0.06	1307.62 ± 69.63
12	Parametric	Mixer	516.30 ± 0.90	-5.85 ± 0.66	824.10 ± 277.53
13	Parametric	Mixer	259.44 ± 2.22	-3.09 ± 1.61	309.42 ± 108.43
14	Parametric	Mixer	255.41 ± 2.81	-2.22 ± 3.65	142.22± 94.13

Table 6.1: The fitted resonance curve parameters of the resonances seen in Figure 5.3 and 6.2 using Equation 6.1. a_i is a constant of the ith resonance, $V_{0,i}$ is the voltage offset of the ith resonance, and $f_{0,i}$ is the frequency offset of the ith resonance.

6.3 First Harmonic Results

6.3.1 Frequency-Gate Scans

Figure 6.2 shows frequency-gate sweeps of the first harmonic around 520 MHz using the rectification technique (a), the electromechanical technique while measuring at the drive frequency plus 5 GHz, and the electromechanical technique while measuring at half the drive frequency plus 5 GHz.

In Figure 6.2 (a) and (b), it shows 4 resonances with frequencies of, in order of bottom to top, 523 MHz, 526 MHz, 530 MHz, and 538 MHz when measured at a gate voltage of ~ -8.6 V. The outer two resonances in both (a) and (b) seem to appear around -7 V and -8.5 V with a short range and are otherwise not visible. In (a) the inner resonances (resonances 6 and 7) appear across the whole voltage range, whereas in (b) the inner resonances appear in similar places to the outer resonances around -7 V and -8.5 V but with a larger range generally spanning ~ 0.5 V compared to the outer resonances spanning ~ 0.25 V or less.

In Figure 6.2 (c) 2 resonances are shown with frequencies of 261.5 MHz and 269 MHz when measured at a gate voltage of ~ -8.6 V. Similar to the resonances 6 and 7, resonances 13 and 14 appear around -7 V and -8.5 V generally spanning ~ 0.5 V.

Go to Contents

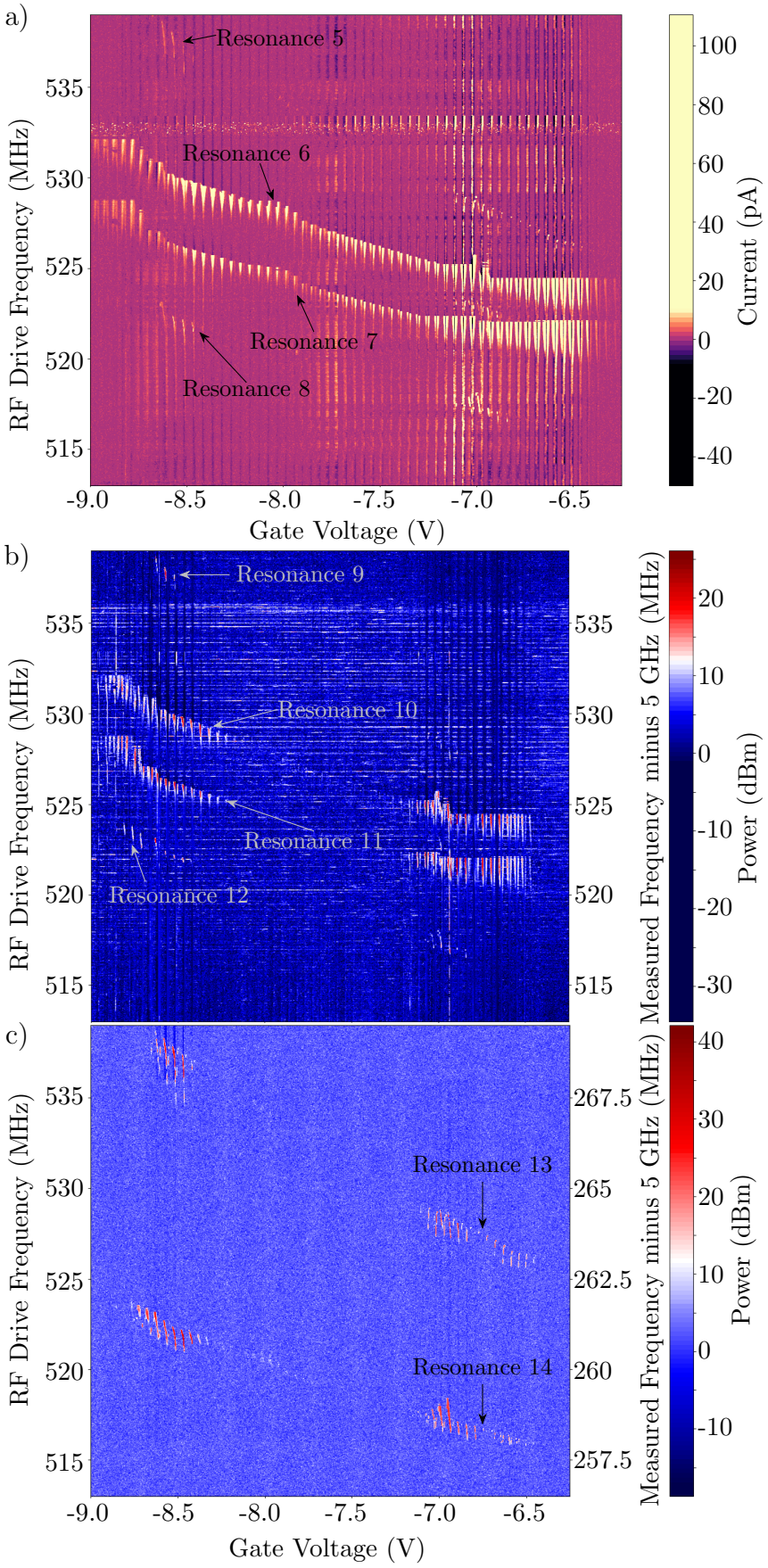

Figure 6.2

Frequency-Gate sweeps of the first harmonic using the rectification technique and the electromechanical mixer technique with the column average subtracted in order to remove the Coulomb peaks. The parameters used for all figures were a bias voltage of 9 mV, an RF drive power of −10 dBm, and a MW probe tone frequency of 5 GHz and power of −15 dBm. (a) shows the results from the rectification technique; the fourth resonances show a quadratic dependence with the gate voltage and show the spring softening of the CNT around the Coulomb peaks. There is no way to easily determine which resonances are parametric or directly driven. (b) shows the results from the electromechanical technique while scanning at the RF drive frequency (∼ 5.525 GHz); the four resonances show a quadratic dependence with the gate voltage and show the spring softening of the CNT around the Coulomb peaks which is similar to the rectification method. (c) shows the results from the electromechanical technique while scanning at half the RF drive frequency (∼ 5.2625 GHz). As there are resonances appearing at this frequency we can infer that the outer resonances seen in (b) and (a) are parametric resonances of the fundamental.

Go to Contents

The resonances in (c) are being driven at an twice the fundamental frequency but resonances are appearing at fundamental frequency.

The results from fitting the resonances from Figures 6.2 and 5.3 to Equation 6.1 are shown in Table 6.1. The fitting involved some extrapolation as we were only able to fit to one side of the curve as the device showed no conductance on the positive side of the curve. Figure 6.2 (a) shows 4 resonances, resonance 5,6,7, and 8, which have centre frequencies of 517.80 MHz, 523.37 MHz, 521.64 MHz, and 503.00 MHz respectively with centre voltages of -2.59 V, -5.70 V, -6.43 V, and 2.99 V respectively with a curvature, a, of 548.62 kHz/V^2, 825.72 kHz/V^2, 1092.96 kHz/V^2, and 145.02 kHz/V^2 respectively. The centre frequencies of resonances 6,7,8 in the order shown in (a) with 8 having the lowest frequency of 503 MHz, 7 having 521.64 MHz, and 6 having 523.37 MHz. Resonance 5 however has a centre frequency of 517.80 MHz which places its centre frequency between resonances 7 and 8. The error in resonance 8 and 5s centre frequency is much higher than resonances 6 and 7 being $\pm$19.33 MHz and $\pm$2.91 MHz rather than $\pm$0.08 MHz and $\pm$0.04 MHz. The centre voltages of the resonances 6 and 7 are low being around -5.70 V and -6.43 V when being compared to the centre frequencies of the fundamental resonances 1 and 2 which have centre voltages between -3 V and -4 V. The centre voltage for resonance 5 is more similar to resonance 1s centre voltage being -2.59 V compared to -3.84 V. The centre voltage for resonance 8 is very different from the other centre voltages being 2.99 V rather than below -3 V like the other resonances. The error in the centre voltages of resonance 8 and 5 similar to the centre frequencies is much higher than resonances 6 and 7 being $\pm$12.46 V and $\pm$1.09 V compared to $\pm$0.06 V and $\pm$0.03 V respectively. The curvature, a, of resonances 6 and 7 are much higher than the curvature of resonances 1 and 2 being 825.72 kHz/V^2 and 1092.96 kHz/V^2 rather than 390.31 kHz/V^2 and 165.34 kHz/V^2 respectively. The curvature of resonance 8 is similar to resonance 2 being 145.02 kHz/V^2 compared to 165.34 kHz/V^2. The curvature of resonance 5 is not similar to resonance 1 being 548.62 kHz/V^2 compared to 390.31 kHz/V^2 but it is more similar than the curvatures of resonances 6 and 7.

Figure 6.2 (b) shows 4 resonances, 9,10,11, and 12 which have centre frequencies 522.78 MHz, 523.25 MHz, 521.51 MHz, and 516.30 MHz respectively with centre

voltages of −4.55 V, −5.70 V, −6.61 V, and −5.85 V respectively with curvature a of 929.35 kHz/V^2, 815.47 kHz/V^2, 1307.62 kHz/V^2, and 824.10 kHz/V^2. The centre frequencies of the the resonances 10,11,12 in (b) chronologically follow 12 at 503.00 MHz, 11 at 521.51 MHz, and 10 at 523.25 MHz. Resonance 9s centre frequency is 522.78 MHz which places it between resonance 10 and 11. The error in the centre frequencies in resonance 9 is larger than the error in the other resonances as the error in 9 is ±8.32 MHz whereas the error in 10,11, and 12 are ±0.20 MHz, ±0.04 MHz, and ±0.90 MHz respectively. The centre voltages of resonances 10 and 11 are similar to the resonances 6 and 7 being −5.70 V and −6.61 V, and −5.70 V and −6.43 V respectively. The centre voltages of resonances 10 and 11 are not similar however to resonances 1 and 2 which have centre voltages of −3.84 V and −3.13 V. The resonances 9 and 12 have similar centre voltages to resonances 10 and 11 being −4.55 V and −5.85 V compared to −5.70 V and −6.61 V respectively. Resonance 9 centre voltage is slightly lower than the other centre voltages in (b). The error in the centre voltages in (b) in largest in resonance 9 which has an error of ±2.94 V compared to ±0.15 V, ±0.06 V, and ±0.66 V in resonances 10, 11, and 12 respectively. The curvature a of resonance 10 is similar to resonance 6 being 815.47 kHz/V^2 and 825.72 kHz/V^2 respectively. The curvature of resonance 11 is higher than resonance 7 being 1307.62 kHz/V^2 compared to 1092.96 kHz/V^2. The curvature of resonance 9 and 12 are much higher than the curvatures of resonance 5 and 8 being 929.35 kHz/V^2 and 824.10 kHz/V^2 compared to 548.62 kHz/V^2 and 145.02 kHz/V^2 respectively.

Figure 6.2 (c) shows 2 resonances, 13 and 14 with centre frequencies of 259.43 MHz and 253.92 MHz respectively with a centre voltage of −3.08 V and 0.31 V respectively with a curvature a of 305.66 kHz/V^2 and 105.95 kHz/V^2 respectively. The centre frequencies of resonance 13 and 14 are similar to the centre frequencies of resonance 1 and 2 being 259.43 MHz and 253.92 MHz compared to 260.34 MHz and 256.15 MHz. The centre frequency of resonance 14 is slightly below the centre frequency of resonance 2. The errors in the centre frequencies of resonances 13 and 14 are much higher than the errors of resonance 1 and 2 being 2.23 MHz and 3.91 MHz compared to 0.46 MHz and 0.68 MHz respectively. The centre voltages of resonance 13 are similar to the centre voltage of resonance 1 being −3.08 V compared

Resonance #	Frequency (MHz)	Peak Height	Gate Voltage (mV)
5	536.92	9 pA	-8527
6	529.80	21 pA	-8527
7	526.16	14 pA	-8527
8	521.84	15 pA	-8527
9	537.38	39 pW	-8530
10	529.96	121 pW	-8530
11	526.24	103 pW	-8530
12	522.04	32 pW	-8530
13	537.24	527 pW	-8530
14	521.84	203 pW	-8530

Table 6.2: Peak heights and frequencies for the resonances shown in Figure 6.3.

to -3.84 V. The centre voltages of resonance 14 are much higher than the centre voltages of resonance 2 being 0.31 V compared to -3.13 V. The error in the centre voltages of resonances 13 and 14 are much higher than those of resonance 1 and 2 being ± 1.62 V and ± 5.05 V compared to ± 0.32 V and ± 0.95 V respectively. The curvature a of resonance 13 and 14 are slightly lower than the curvature of resonance 1 and 2 being 308.66 kHz/V^2 and 105.95 kHz/V^2 compared to 390.31 kHz/V^2 and 165.34 kHz/V^2 respectively.

Figure 6.3 shows the resonance peaks from Figure 6.2 at a gate voltage around -8.53 V. The heights of the peaks are shown in Table 6.2. The peak heights of resonance 5 and 8 are more similar to the peak heights of resonance 6 and 7, than the peak heights of resonance 9 and 12 are to the peak heights of resonance 10 and 11. For example, the peak height ratio of resonance 5 compared to resonance 6 is 0.45 whereas the peak height ratio of resonance 12 compared to resonance 10 is 0.26. The resonance peaks of 13 and 14 are significantly higher than the resonance peaks of resonance 9 and 12 as the peak heights are 527 pW and 203 pW compared to 39 pW and 32 pW respectively.

Figure 6.4 shows a zoom in of the resonance 4 and 12 around a gate voltage of -8.51 V. The figure shows the fundamental resonance during direct driving in (a) and the same resonance being parametrically driven in (b). Both figures show the characteristic curve of a mechanical resonance.

Go to Contents

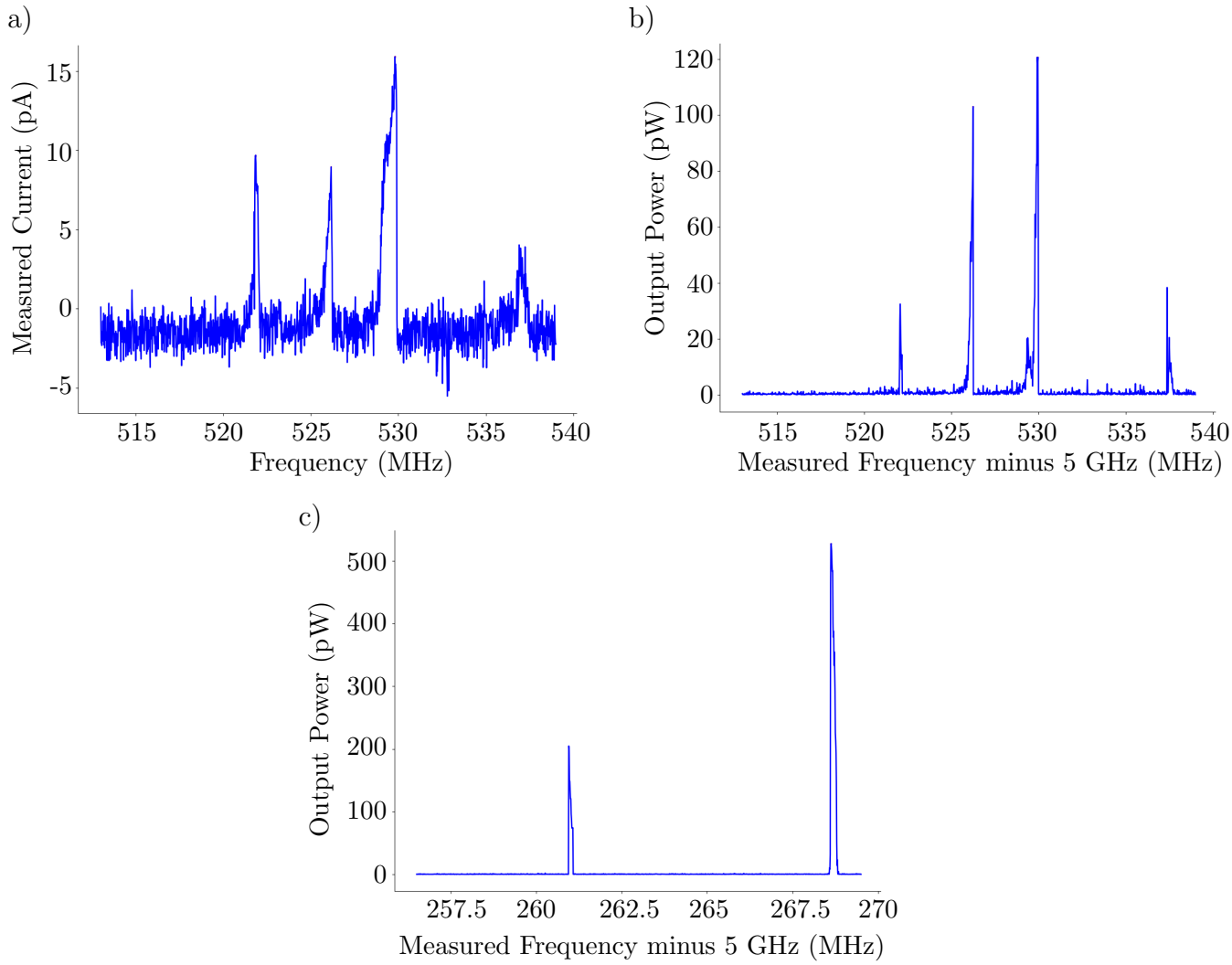

Figure 6.3: The resonance peaks at a gate voltage of ∼-8.53 V and a bias of 9 mV showing 4 resonance peaks at 521.84 MHz, 526.16 MHz, 529.80 MHz, and 540 MHz when driven by an RF generator at −10 dBm. (a) shows the measured current using the rectification technique. It shows from left to right resonances 8, 7, 6, and 5. (b) shows the output power using the electromechanical technique while scanning at the drive frequency plus 5 GHz. It shows from left to right, resonance 12,11,10, and 9. (c) shows the output power using the electromechanical technique while scanning at half the drive frequency plus 5 GHz, and shows peaks at 261.5 MHz and 269 MHz. It shows from left to right resonances 14 and 13. Peak heights and frequencies are shown in Table 6.2.

Go to Contents

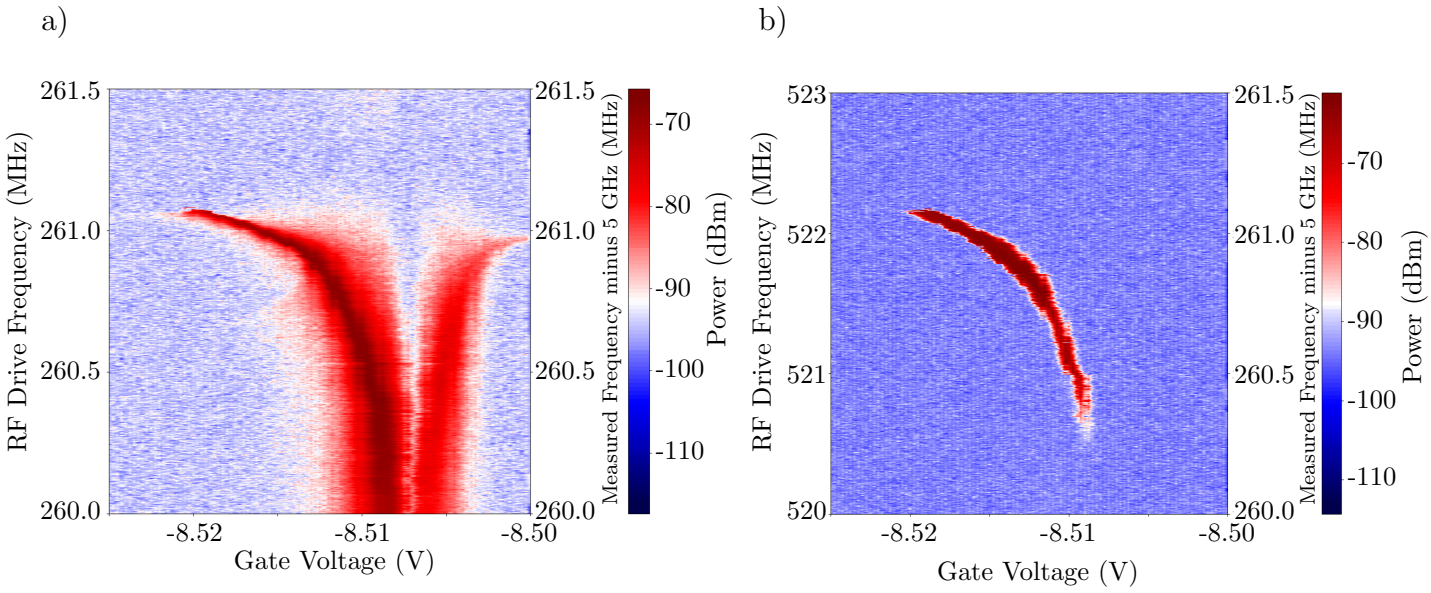

Figure 6.4: The spring softening of the CNT and the resonance peak(s) used for the frequency-RF power scans. (a) shows the spring softening of one of the twin resonances of the fundamental while being directly driven. (b) shows the spring softening of the same resonance but while being parametrically driven at twice the resonance frequency.

6.3.2 Quadratic Curve Ratios

Figure 6.5 shows the ratios of the resonances in Figure 6.2 compared to the resonances in Figure 5.3. A linear fit of Figure 6.5 and the average ratio of all the points is shown in Table 6.3.

Ratios 1:5 to 2:8 in Table 6.3 are the ratios of the resonances in Figure 6.2 (a) compared to the resonances in Figure 5.3 (a).

The gradient, A, of ratios 1:5 and 2:8 are smaller than the gradient of ratios 1:6 and 2:7 being 1.545×10^{-8} mV^{-1} and -17.613×10^{-8} mV^{-1} compared to 476.571×10^{-8} mV^{-1} and 120.303×10^{-8} mV^{-1} respectively. The y intercept, B, of ratios 1:5 and 2:8 are very close to equalling one being 0.011% and 0.081% different respectively. The y intercept of ratios 1:6 and 2:7 are not as close to equalling one as ratios 1:5 and 2:8 being 2.649% and 1.781% different respectively. The average ratio of ratio 1:5 and 2:8 are closer to equalling one than the average ratio of ratio 1:6 and 2:7 being 0.021% and 0.0046% different compared to 0.874% and 0.897% respectively.

Ratios 3:9 to 4:12 in Table 6.3 are the ratios of the resonances in Figure 6.2 (b)

Go to Contents

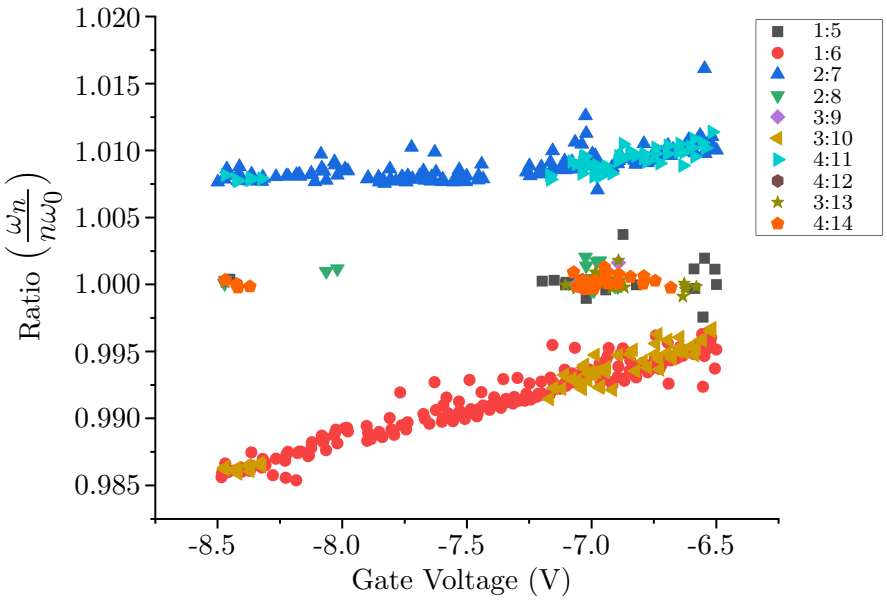

Figure 6.5: The resonance ratios using Equation 6.3 of resonance 1 to resonance 5 (grey), 1 to 6 (red), 2 to 7 (blue), 2 to 8 (green), 3 to 9 (purple), 3 to 10 (yellow), 4 to 11 (cyan), 4 to 12 (brown), 3 to 13 (olive), and 4 to 14 (orange). The ratios of 1:6, 2:7, 3:10, and 4:11 are the ratios of first order harmonics compared to the fundamental modes. These ratios are above and below one. The ratios of 2:8, 1:5, 3:9, and 4:12 are the ratios of supposedly parametrically driven resonances at the first harmonic compared to the fundamental. These ratios are effectively equal to one. The ratios of 3:13 and 4:14 are supposedly parametrically driven resonances of the fundamental compared to the fundamental. These ratios are effectively equal to one.

Ratio	A (10^{-8} mV^{-1})	B (arbitrary units)	Average
1:5	1.545	1.00011	1.00021
1:6	476.571	1.02649	0.99126
2:7	120.303	1.01781	1.00897
2:8	-17.613	0.99919	1.00046
3:9	561.527	1.04812	1.00032
3:10	515.953	1.02947	0.99282
4:11	127.495	1.01824	1.00925
4:12	194.340	1.01690	1.00024
3:13	-16.281	0.99901	1.00012
4:14	19.1942	1.00161	1.00023

Table 6.3: Resonance Ratios of Figure 6.5 fitted to a linear function given by $f(V_G) = B + AV_G$ and the average of all the points. Parametrically driven resonances when compared to the fundamental should have a gradient, A, that is very close to 0, a y-intercept, B, that is very close to one, and an average ratio value very close to one.

Go to Contents

compared to the resonances in Figure 5.3 (b).

The gradient of ratios 4:11 and 4:12 are smaller than the gradient of ratios 3:9 and 3:10 being 127.495×10^{-8} mV^{-1} and 194.340×10^{-8} mV^{-1} compared to 561.527×10^{-8} mV^{-1} and 515.953×10^{-8} mV^{-1}. Gradient ratios of 4:11 and 4:12 however aren't as small as gradient ratios of 1:5 at 1.545×10^{-8} mV^{-1} and 2:8 at -17.613×10^{-8} mV^{-1}. The y intercept of ratios 4:11 and 4:12 are closer to one that the y intercepts of 3:9 and 3:10 being 1.824% and 1.69% different compared to 4.812% and 2.947% respectively. The average ratio of ratio 3:9 and 4:12 are closer to equalling one than the average ratio of ratio 3:10 and 4:11 being 0.032% and 0.024% different compared to 0.718% and 0.925% different respectively.

Ratios 3:13 to 4:14 in Table 6.3 are the ratios of the resonances in Figure 6.2 (c) compared to the resonances in Figure 5.3 (b).

The gradient of ratios 3:13 and 4:14 are similarly small like ratios 1:5 and 2:8 being -16.281×10^{-8} mV^{-1} and 19.1942×10^{-8} mV^{-1} respectively. The y intercept of ratio 3:13 is close to one being 0.099% different. The y intercept of 4:14 is close to one but larger than 3:13 being 0.161% different. The average ratio of ratio 3:13 and 4:14 are both very close to equaling one being 0.012% and 0.023% different.

6.4 First Harmonic Further Investigation

To confirm that the resonances we are seeing at half the drive frequency of the first harmonic are parametric resonances, we can look at how the drive power affects the output power. This should be different between a parametric resonance and direct resonance.

We will start with the familiar case of a direct linear resonance. For a direct linear response the drive power F_p is related to the amplitude u via [35]:

$$u = \frac{F_p}{\sqrt{M^2(w_p^2 - \omega_0^2)^2 + \Gamma^2\omega_p^2}} \tag{6.4}$$

Go to Contents

If the CNT is being driven on resonance (i.e $\omega_p = \omega_0$) then Equation 6.4 becomes:

$$u = \frac{F_p}{\Gamma\omega_0} \tag{6.5}$$

Since we cannot measure F_p and u easily, we need to convert this equation into measurable quantities. We know that the output power measured in the spectrum analyser from the electromechanical mixer is given by:

$$P_{mix} = I_{mix}^2 R \tag{6.6}$$

where I_{mix} is the mixer current and R is the impedance (50 Ω). We also know that the mixer current is directly proportional to the conductance and bias voltage across the device from Equation 5.4. Therefore Equation 6.6 becomes:

$$\begin{aligned} P_{mix} &= I_{mix}^2 \cdot R \\ &= \left(G^{ac}(t)V_{SD}^{ac}(t)\right)^2 R \\ &= \left(V_{SD}^{ac}(t)\left(\frac{dG}{dV_G}\left(V_G^{ac}(t) + \frac{C_G^{ac}(t)}{C_G}V_G\right)\right)\right)^2 R \end{aligned} \tag{6.7}$$

We know that the power is related to the voltage by $P \propto V^2$ therefore $V_{SD}^{ac} = K_1\sqrt{P_{MW}}$ where K_1 is a constant, and P_{MW} is the power of the microwave probe tone. Figure 6.6 (a) shows the contribution from the electrical mixing to the measured signal at different drive powers at a gate voltage of −8514 mV. By subtracting the electrical mixing power from our output power measured on resonance, we will be left with purely the electromechanical power. Therefore $V_G^{ac}(t) + C_G^{ac}(t)V_G/C_G \simeq C_G^{ac}(t)V_G/C_G$. Using Equation 2.51, Equation 6.7 becomes:

$$P_{mix} \simeq \left(K_1\sqrt{P_{MW}}\frac{1}{C_G}\frac{dG}{dV_G}\frac{dC_G}{du}u_0 V_G\cos(\omega_n t)\right)^2 R \tag{6.8}$$

The root mean squared of the power then $\langle\cos(\omega_n t)\rangle = 1/\sqrt{2}$. As the gate voltage during these power scans is fixed, dG/dV_G is constant. As the nanotube displacement is much smaller than the height of the CNT above the gate electrode, from Equa-

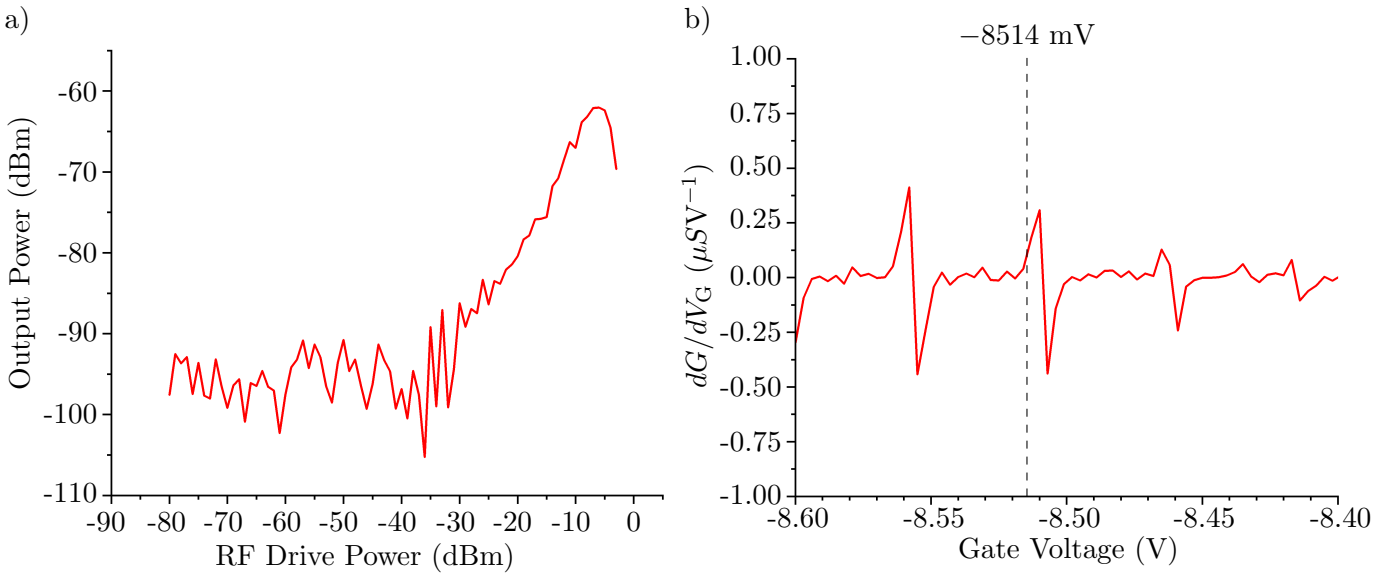

Figure 6.6: (a) The output power from purely electrical mixing in the CNT, measured using a bias voltage of 9 mV, gate voltage of −8514 mV, a drive frequency of 265 MHz, and a MW probe tone power of −15 dBm. The CNT is driven off resonance to see the power from purely electrical mixing. It shows the electrical mixing appearing at around −30 dBm and then steadily increasing until it reaches its peak at ∼ −7 dBm where the output power is around −60 dBm. (b) shows the differential conductance (dG/dV_G) of the CNT at a fixed bias voltage of 9 mV. The differential conductance around −8514 mV is ∼ 0.13 μSV^{-1}.

tion 2.43 we know that dC_G/du is also constant. Therefore $dG/dV_G \cdot dC_G/du \approx K_2$ where K_2 is a constant. Equation 6.8 then becomes:

$$P_{mix} \simeq \left(K_1 K_2 \sqrt{P_{MW}} \frac{1}{C_G} K_3 u_0 \frac{V_G}{\sqrt{2}} \right)^2 R \tag{6.9}$$

As P_{MW}, C_G, V_G, and R are all constant, and K is the product of all constant then Equation 6.9 becomes:

$$P_{mix} = K \cdot u^2 \Rightarrow u = \left(\frac{P_{mix}}{K} \right)^{\frac{1}{2}} \tag{6.10}$$

Using Equation 2.50 we can convert the power to a force experienced by the CNT. Since we are only interested in the ac voltages and the square term is small, the force is proportional to the ac voltage ($F_p \propto V_G^{ac}$). As the power is related to voltage via $V_G^{ac} \propto \sqrt{P_p}$, the relation between force and power is $F_p \propto \sqrt{P_p}$. Therefore using

Go to Contents

Equation 6.10 and $F_p \propto \sqrt{P_p}$, Equation 6.5 becomes:

$$P_{mix}[\text{mW}] = K_3 \frac{P_p[\text{mW}]}{\Gamma^2 \omega_0^2} \tag{6.11}$$

where K_3 is a constant. For better fitting, the data presented in Section 6.4.1 was converted to dBm. In dBm, Equation 6.11 is given by:

$$P_{mix}[\text{dBm}] = 10log(\frac{K_3}{\Gamma^2 \omega_0^2}) + P_p[\text{dBm}] \tag{6.12}$$

Therefore the output power is directly proportional to the drive power, $P_{mix}[\text{dBm}] \propto P_p[\text{dBm}]$, and the resonance should appear at all drive powers assuming the signal is not covered by the noise floor.

For a parametric resonance, the relation between the drive force F_p to its amplitude u is given by [12]:

$$\frac{F_p^2}{(4M\omega_0)^2} \left(\Gamma^2 + \left(\Delta\omega_p - \frac{3\gamma u^2}{8\omega_0} \right)^2 \right)^{-1} = 1 \tag{6.13}$$

where F_p is the drive force, M is the mass of the oscillator, ω_0 is the fundamental frequency, Γ is the damping coefficient, $\Delta\omega_p = (\omega_p/2) - \omega_0$ where ω_p is the drive frequency, γ is the duffing coefficient, and u is the amplitude. Equation 6.13 shows that vibrations at half the pump frequency are excited as long as the drive force is larger than the damping of the CNT, such that $|F_p|/4M\omega_0 > \Gamma$. If the driven resonator were otherwise linear, there would be two possible outcomes: for weak parametric driving the intrinsic damping would overwhelm the drive and the displacement would be zero; for strong driving the displacement would increase without bound. The existence of stable parametric oscillations in Figure 6.2 shows that either the stiffness or the damping must be non-linear. For the rest of this section we will assume the CNT is not subjected to a non-linear friction.

If we take the case where parametric resonances should be largest, then $\omega_p \approx 2\omega_0$ therefore $\Delta\omega_p = 0$. Rearranging Equation 6.13 for the amplitude u on parametric resonance gives:

$$u = \left(\frac{4F_p^2}{9\gamma^2 M^2} - \frac{64\omega_0^2 \Gamma^2}{9\gamma^2} \right)^{\frac{1}{4}} \tag{6.14}$$

Go to Contents

Simplified to:

$$u = (aF_{\mathrm{p}}^2 - (b))^{\frac{1}{4}} \tag{6.15}$$

where $a = 4/9\gamma^2 M^2$ and $b = 64\omega_0^2\Gamma^2/9\gamma^2$. Therefore combining Equations 6.15, 6.10, and $F_{\mathrm{p}} \propto \sqrt{P_{\mathrm{p}}}$ gives:

$$P_{\mathrm{mix}}[mW] = (aP_{\mathrm{p}}[mW] - b)^{\frac{1}{2}} \tag{6.16}$$

where P_{p} is the drive power in mW, $a = K_4 4/9\gamma^2 M^2$, and $b = K_4 64\omega_0^2\Gamma^2/9\gamma^2$, and where K_5 is a constant. As the data in Section 6.4.1 fitted better to dBm data, in dBm Equation 6.16 becomes:

$$P_{\mathrm{mix}}[dBm] = 5log(\frac{a10^{\frac{P_{\mathrm{p}}[dBm]}{10}}}{1\mu W^2} - \frac{b}{1\mu W^2}) \tag{6.17}$$

Therefore a parametric resonances output power is proportional half the drive power, $P_{\mathrm{mix}}[dBm] \propto \frac{1}{2}P_{\mathrm{p}}[dBm]$, and the resonance should only appear once the 'turn on' drive power has been reached, $a10^{\frac{P_{\mathrm{p}}[dBm]}{10}} > b$.

Therefore by measuring the power from a resonance driven parametrically and one driven directly at different drive powers we should find that the parametric resonance turns on at a certain drive power and follows a square root dependence, whereas the direct resonance has no 'turn on' and follows a linear dependence.

6.4.1 Output Power vs Drive Power

Figure 6.7 and Figure 6.8 show frequency-RF drive power sweeps of the fundamental while being directly driven and the fundamental being supposedly parametrically driven respectively. They show the resonances at a fixed gate voltage of -8154 mV and a MW power of -15 dBm; The mechanical resonance including the spring softening around the Coulomb peak is shown in Figure 6.4.

Figure 6.7 sweeps drive frequency across the directly driven fundamental resonance using the rectification method (a) and the electromechanical technique (b). Although not a study of this thesis, its clear that the electromechanical technique is far more sensitive to the CNT motion at lower powers. For example, given the max-

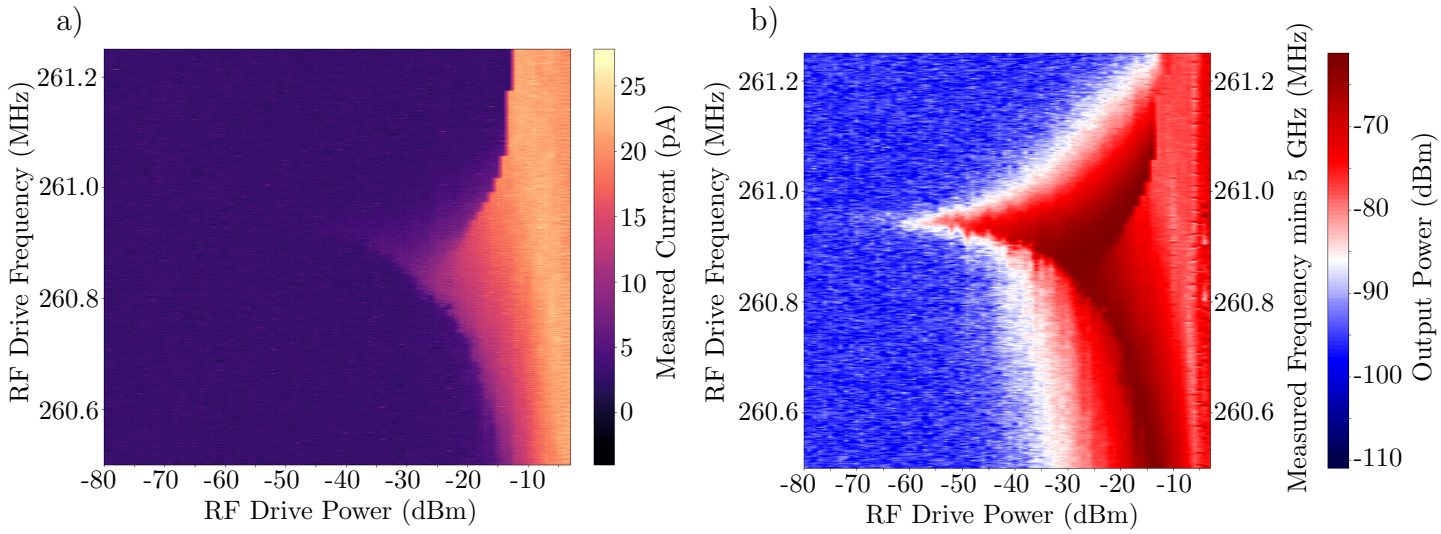

Figure 6.7: Frequency-RF Drive Power scans of the fundamental mode while being directly driven at a fixed gate voltage of −8154 mV and a MW power of −15 dBm. The drive powers are swept from low (left) to high (right). (a) shows the current measured using the rectification technique. (b) shows the power measured using the electromechanical mixer technique. As the RF drive power increases so does the width of the resonance until the Coulomb peaks are broadened so much that they start to merge with each other. The fundamental seems to appear at around −65 dBm and then slowly increases until around −40 dBm where it plateaus.

imum of the leftmost column (max noise floor) in the rectification method is 8.4 pA, the drive power where the resonance appears above the noise floor is −34 dBm whereas in the electromechanical method the max noise floor is −88.1 dBm and the drive power where the resonance appears is −65 dBm. The frequency that the resonance appears at in the rectification technique is 260.604 MHz and in the electromechanical technique is 260.947 MHz.

Figure 6.8 sweeps the parametrically driven fundamental resonance using the rectification technique (a) and electromechanical mixer technique (b). In the rectification technique, assuming a noise floor of 7.9 pA the parametric resonance appears at −22 dBm at 521.846 MHz. In the electromechanical mixer technique, assuming a noise floor of −87.6 dBm, the parametric resonance appears at −32 dBm at 260.9595 (521.919) MHz.

From Figures 6.7 (b) and 6.8 (b), by taking the maximum output power of each RF drive power (maximum output power of each column) we can create an output power vs drive power plot which we can attempt to fit Equation 6.12 to Equation 6.17.

Go to Contents

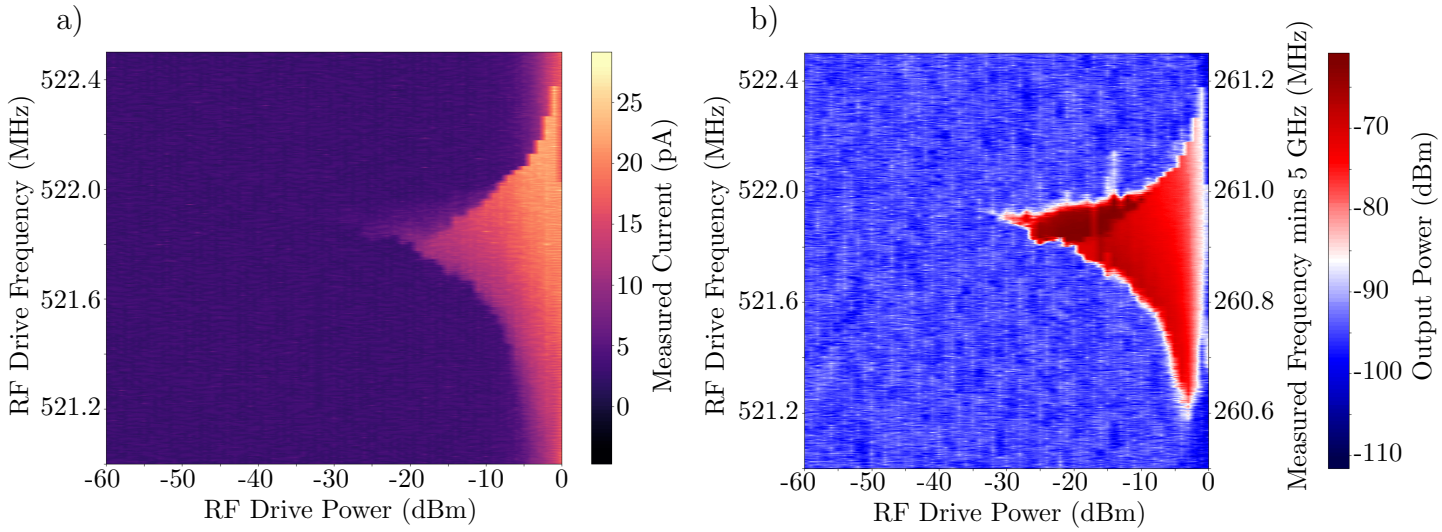

Figure 6.8: Frequency-RF Drive Power scans of the fundamental while being parametrically driven at a fixed gate voltage of −8154 mV and a MW power of −15 dBm. (a) shows the current measured using the rectification technique. (b) shows the power measured using the electromechanical mixer technique. The parametric response, best seen in (b), appears at around −32 dBm and then rapidly increases in output power reaching its peak by around −25 dBm.

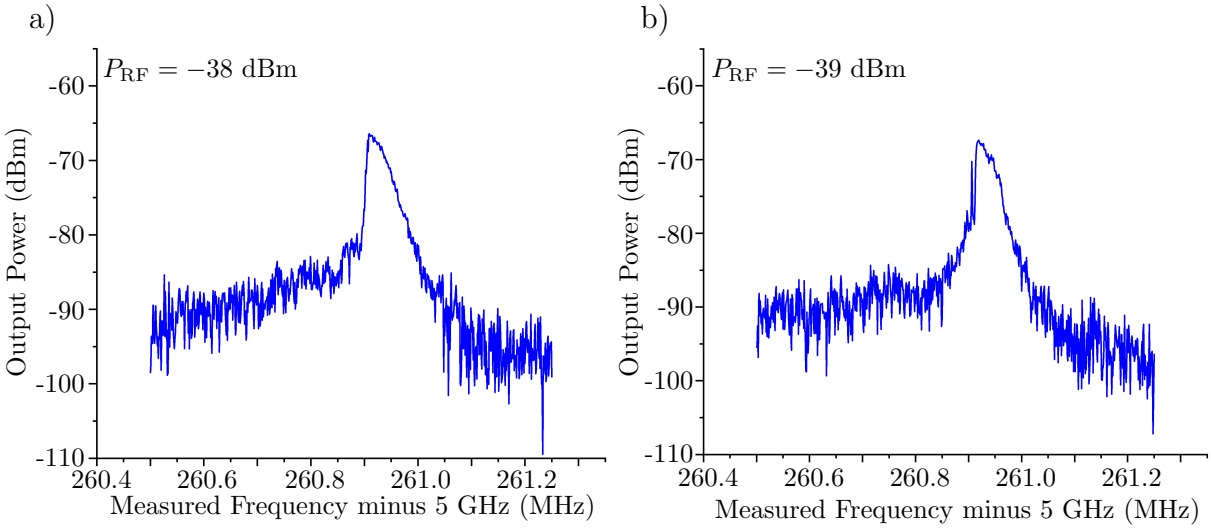

Figure 6.9: The duffing of the fundamental as the CNT mechanical resonator changes from linear to non-linear motion. (a) shows the CNT in non-linear motion. (b) shows the CNT at the very edge of linear motion. Since Equation 6.4 is for linear motion, any point above or equal to -38 dBm should be ignored.

Go to Contents

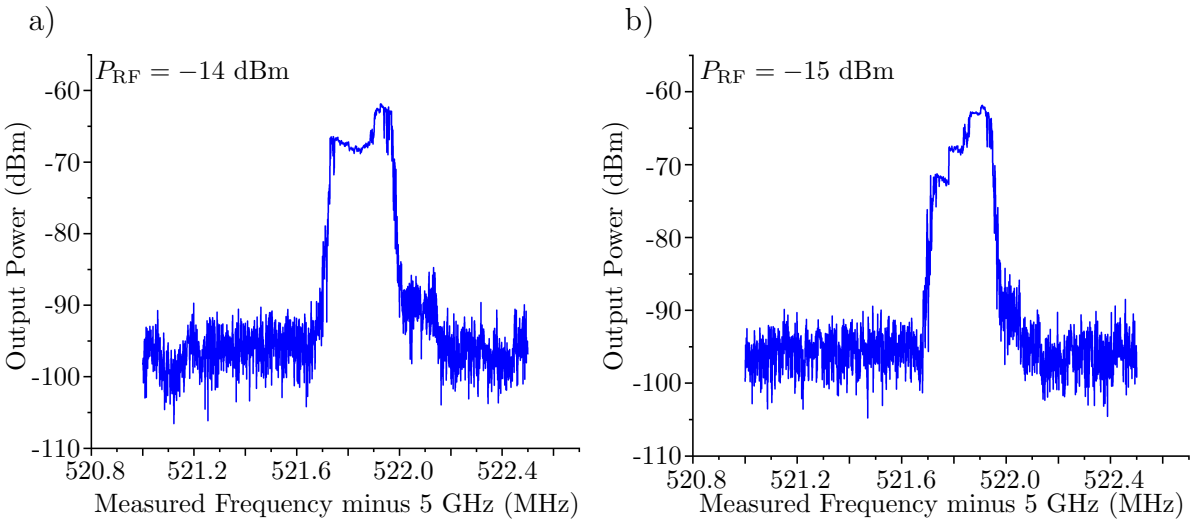

Figure 6.10: As the drive power increases the parametric resonance peak begins to split into two. (a) shows the peak being split at -14 dBm drive power, perhaps by coupling between modes [61]. (b) shows just one peak at −15 dBm. Therefore any peak above or equal to -14 dBm should be ignored when attempting fitting.

To improve the quality of the fit, we need to mask some data points so they aren't used in the fitting. Since the max noise floor of Figure 6.7 is ∼-88.1 dBm any data point below or equal to that should be excluded as the resonance is being hidden by noise. The same applies for Figure 6.8 with a max noise of ∼-87.6 dBm, any data point below or equal to that should be excluded.

Since Equation 6.12 applies only to linear motion of the CNT, the equation will no longer apply to the output power of the CNT when in a non-linear regime. Figure 6.9 shows that at above RF drive powers of -39 dBm the resonance peak becomes duffed, no longer being a Lorentzian shape, and therefore RF drive powers of -38 dBm and above should be masked from the fitting data.

Data points that are measured during Coulomb broadening should also be masked due to the output power being affected by the broadening as discussed in §5.2, therefore ideally any data points taken at drive powers above -40 dBm should be masked. However the parametric resonance only appears at drive powers greater than -40 dBm therefore for the parametric resonance we can only take into consideration that the power measured is likely to be lower than it should be.

At sufficiently high RF drive powers, the resonance peak begins to split into two peaks which affects the output power. In the parametrically driven fundamental

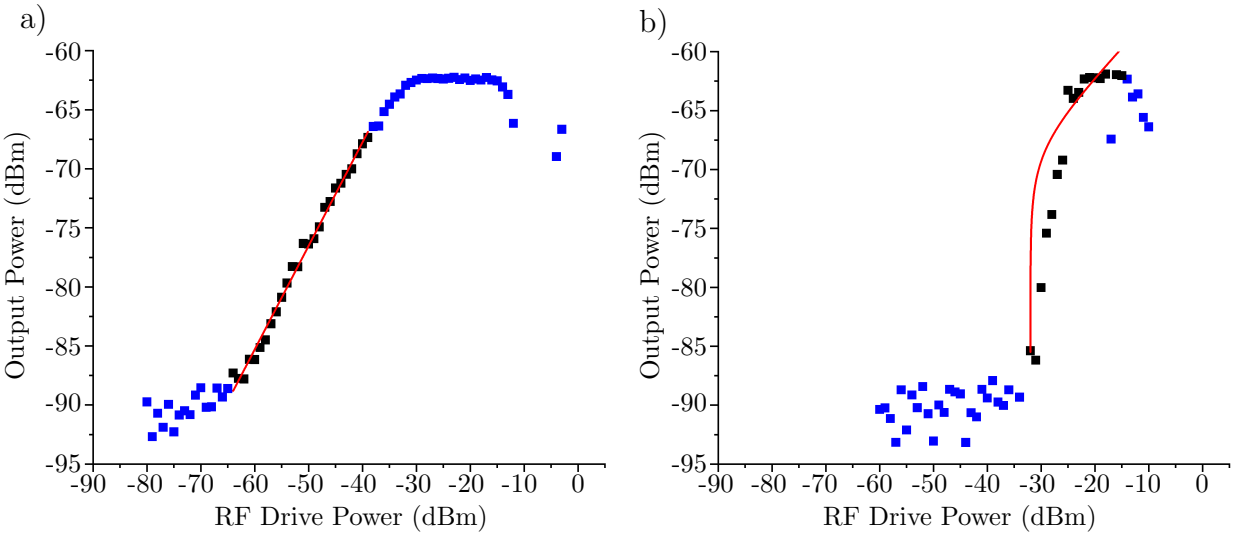

Figure 6.11: a) shows the maximum measured peak height at each drive power vs the RF drive power of the fundamental being directly driven. The purely electrical mixing power from Figure 6.6 has been subtracted from this data. Masked data points are shown in blue. Data points used for the fitting are shown in black. (b) shows the maximum measured peak height at each drive power vs the RF drive power of the fundamental being supposedly parametrically driven. In (a) as the RF drive power increases, the output power also increases proportionally. In (b), at an RF drive power of around −33 dBm the resonance 'turns on' and the output power increases rapidly with increasing RF drive power.

Fundamental ($P_{\text{mix}} = A + BP_{\text{p}}$)		Parametric ($P_{\text{mix}} = 5log(a10^{P_{\text{p}}/10} - b)$)	
A (dBm)	B	a (mW)	b (μW^2)
-32.662 ± 0.823	0.877 ± 0.016	$3.71 \pm 1.28 \times 10^{-11}$	$2.34 \pm 0.06 \times 10^{-14}$

Table 6.4: Fitted parameters when Equations 6.12 and 6.17 are fitted to Figure 6.11 (a) and (b) respectively.

this happens at RF drive powers at -14 dBm or above as shown in Figure 6.10. At drive powers of −15 dBm and lower the resonance is still one peak so the output power should not be affected by the peak splitting.

Figure 6.11 shows the maximum output power at each drive power vs RF drive power of the fundamental being directly driven (a) and supposedly parametrically driven (b). Data points in blue have been masked, and were not used in the fitting. Qualitatively looking at Figure 6.11 (a), the resonance appears at around −64 dBm drive power and then seems to follow a linear relationship between the output power and the drive power. Quantitatively fitting a linear function given by $P_{\text{mix}} = A + BP_{\text{p}}$ where A and B are constants to the unmasked data points returns a value of A of -32.662 ± 0.823 dBm and a value of B of 0.877 ± 0.016 (no units). Qualitatively

looking at Figure 6.11 (b), the resonance appears at around −33 dBm drive power and then the output power rises linearly with drive power until it plateaus at a drive power of −25 dBm. Quantitatively fitting a Equation 6.17 to the unmasked data points returns a value of a of $3.71 \pm 1.28 \times 10^{-11}$ mW and a value of b of 2.34 ± 0.06 μW^2.

6.5 First Harmonic Analysis

Section 6.3 confirms that resonances 5, 8, 9, 12, 13, and 14 are clearly parametric resonances of the fundamental. The most obvious piece of evidence is shown in Figure 6.2 (c) which shows a resonance response at around 262.5 MHz while driving at twice that frequency at 525 MHz. This is further shown in the curve ratios (Figure 6.5) as the resonance ratios between these resonances and the fundamental are effectively equal to one. Table 6.3 shows a linear fit and average of the ratios of each resonance to the fundamental resonances. The gradient, A, of resonances 5, 8, 9, 12, 13, and 14 are effectively 0 which indicates the resonances are exact matches which is only possible if they are parametric resonances. The y intercept, B, of resonances 5, 9, 12, 13, and 14 are also effectively 1 which again indicates the resonances are exact matches which is only possible if they are parametric resonances. Resonance 9 has a y-intercept that is comparable to resonance 10 (which shows a directly driven resonance) but resonance 9s average ratio is similar to resonance 6, 8, 12, 13, and 14. The y-intercept anomaly probably comes from a lack of points from this resonance instead. The average ratios of resonance 5, 8, 9, 12, 13, and 14 are all very close to 1 which indicates the resonances are exact matches of the fundamental which is only possible if they are parametric resonances.

We further confirm that resonance 14 is parametric by comparing the output power vs drive power of resonance 14 and resonance 4 shown in Figure 6.11. The output power vs drive power of resonance 4 (Figure 6.11(a)) shows an almost linear response as the value of B is almost equal to one being 0.877 ± 0.016. This means that as drive power increases the output power almost linearly increase with it. The reason why the output power is slightly lower than expected is probably due to two reasons. The first is that the impedance of the CNT at the voltages used in the measurements is

Fundamental Fit Constant	A	-32.662 dBm
Fundamental Fit Constant	B	0.877
Parametric Fit Constant	a	3.71×10^{-11} mW
Parametric Fit Constant	b	2.34×10^{-14} μW^2

Table 6.5: The properties of the CNT that were calculated from A, a, and b.

much higher than 50 Ω, and also constantly changes depending on the conductance of the device. This means that the MW probe tone has a high chance of being reflected at the CNT/electrode interface. When the nanotube is driven harder, the conductance of the CNT changes, causing more power to be lost due to the reflectance at the interface causing the output power to be less than expected. The second reason is that when the nanotube oscillates over the Coulomb peak the output power will decrease as the average current over the peak is lower than the true height of the peak. At high drive powers, the nanotube is more likely oscillating over the peak as the larger amplitude causes a larger change in the effective gate voltage. This means as drive power increases the output power should decrease. Both of these reasons results in the gradient of the curve not being as steep as expected. The output power vs drive power of resonance 14 (Figure 6.11 (b)) shows an entirely different response to drive power than the fundamental (Figure 6.11 (a)). It shows that the parametric response 'turns on' at a drive power of -34.08 dBm and the output power then quickly increases with drive power following **??**. This type of behaviour is characteristic of parametric resonances. Combining this with the fact that resonance 14 appears at half the drive frequency this resonance is the fundamental being parametrically driven. As the resonances 13, 12, 9, 8, and 5 have the same curve ratio they are also parametric resonances of the fundamental. Resonance 13, 9, and 5 are resonance 3 being driven parametrically producing a signal at ω_0 (13) and $2\omega_0$ (9,5). Resonances 12 and 8 are resonance 4 being driven parametrically producing a signal at $2\omega_0$ (12,8).

In Figure 6.10 (b) as the drive power is increased the single peak begins to split into 2 peaks at a drive power of -14 dBm and then stops being split around -9 dBm where the peak assumes a box shape. This could imply that one of the amplifiers is being compressed causing the box shape. The peak splitting around -12 dBm has been seen by others [32, 61]. As the nanotube at this drive power is non-linear while

looking at the directly driven fundamental, the splitting could be to do with the non-linear motion of the CNT at this drive power resulting in the CNT resonator turning into a chaotic oscillator.

The electromechanical technique is more sensitive than the rectification technique which is shown by comparing the panels in Figure 6.7. In the rectification technique (a) assuming a background noise of 8.4 pA the drive power where the resonance appears is −34 dBm, whereas in the electromechanical mixer technique assuming a background noise of −88.1 dBm the drive power where the resonance appears is −65 dBm. This is 1.9 times lower than the rectification technique and allows us to see the CNT linear motion as shown in Figure 5.5 (a) and (b). However there are apparent caveats to the electromechanical mixer technique as seen in Figure 6.2 as the electromechanical mixer technique only shows the resonances at specific voltages presumably when dG/dV_G is highest, whereas the rectification technique appears across more of the scanned gate voltage range. As the electromechanical mixer depends on both the transconductance and conductance, it would seem more likely that it would have more 'dead spots' than the rectification technique which only depends on the transconductance. This also affects which part of the resonance we see as the electromechanical mixer will be strongest on the flank of the Coulomb peak whereas the rectification technique will be strongest on the peak and troughs of the Coulomb peak. The electromechanical technique also includes another parameter, the microwave probe tone, which may affect the CNT signal. This may explain the apparent flat topped resonances seen in Figure 6.2 on resonances 6, 7, 10, and 11 around −6.6 V and 8.75 V as the high microwave power causes the resonances to extend further than they should causing them to obscure other resonances. This also has the effect of causing the fitting function for Equation 6.1 to place the centre gate voltage around these voltages ($\sim$ −6.6 V) even when the true centre voltages lie around −3 V basing off resonances 1-4.

Go to Contents

6.6 Second Harmonic Results & Analysis

This section shows and analyses the results from the 2nd harmonic of our CNT device. The results show scans of the electromechanical mixer technique at different fractions of the drive frequency. These results use a smaller gate range than the results discussed in §6.3 scanning over only a few Coulomb peaks between −6.95 V to −7.15 V. The other parameters used are the same as in Figure 6.2 having a bias voltage of 9 mV, an RF drive power of −10 dBm, and a MW probe tone of 5 GHz at −15 dBm. The column average has been subtracted from each column in order to remove the Coulomb peaks to better show the resonances.

In the rectification technique in Figure 6.13 (a), there are considerably more resonances around the second harmonic than the first harmonic, having ten resonances rather than four. Figure 6.13 (b) shows the results from the electromechanical mixer technique while driving around 792.5 MHz and measuring around $\sim$ 5.7925 GHz. It only shows eight resonances rather than ten shown in the rectification technique. Parametric driving at $3\omega_0$ has been predicted by analogous electrical circuits [62], and measured in superconducting resonators at three times the fundamental mode [63] but has yet to measured in a CNT resonator. Using our new technique we can attempt to decipher where these resonances are coming from. The two brighter resonances towards the top of the scans (a) and (b) are likely to be directly driven resonances whereas the lowest resonances are likely to be parametric resonances.

Figure 6.13 (c) shows the results from the electromechanical mixer technique while driving around 792.5 MHz and measuring around $\sim$ 6.585 GHz. It faintly shows two resonances around 1605 MHz and 1586 MHz. This is likely the effective 2ω component described in Equation 2.52 of the two directly driven modes. Parametric resonances of the fundamental might appear at these frequencies but they would be so weak to be undetectable in our setup.

If the fundamental is being parametrically driven at $\sim$ 792.5 MHz, then the response we are seeing at $\sim$ 5.7925 GHz is the 3ω component of Equation 2.52. By scanning at a ω_0, $2\omega_0$, and $3\omega_0/2$ we can attempt to find out where the resonances seen around $3\omega_0$ are coming from. These results are shown in Figure 6.14. Figure 6.14 (a) shows the results from the electromechanical mixer technique while driving around $\sim$792.5

Go to Contents

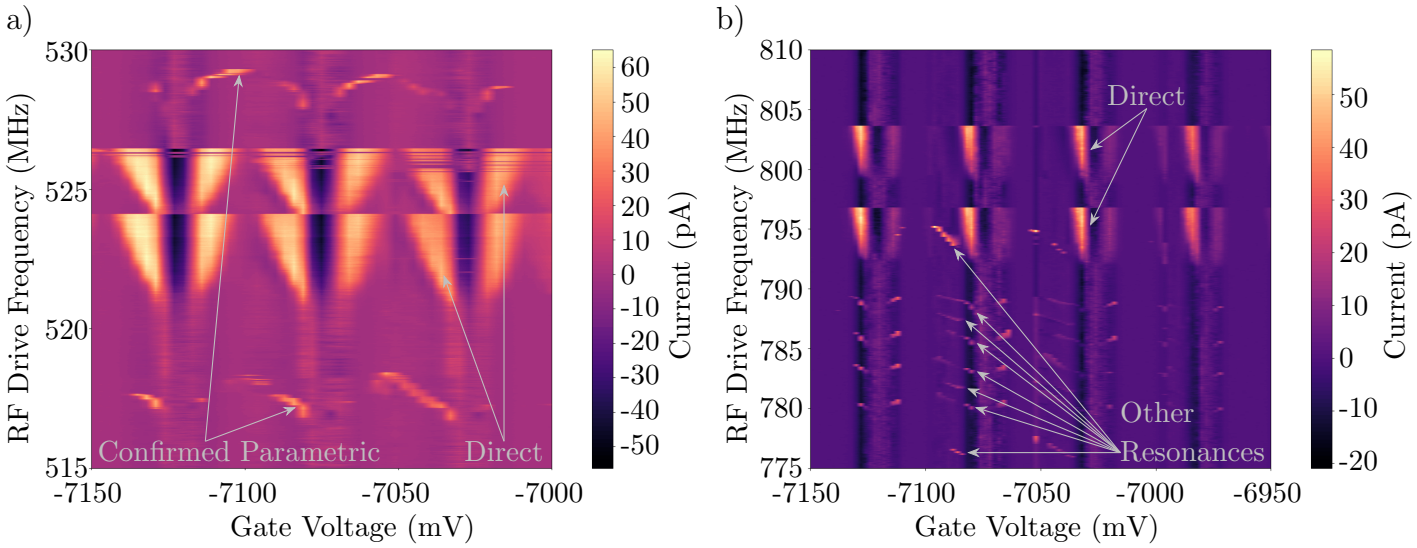

Figure 6.12: Column averaging was used to remove Coulomb peaks and make the resonances more apparent. The scans use a driving frequency around $\sim$ 520 MHz and $\sim$ 780 MHz respectively, a gate voltage of $\sim$ 7.075 V and ~ -7.05 V respectively, an RF drive power of -10 dBm, and a bias voltage of 9 mV. The current is measured using the rectification method. (a) shows the first harmonic where there are four apparent modes; two potentially directly driven and two potentially parametrically driven. Using the rectification method it is impossible to distinguish between directly driven and parametrically driven modes as the measured current has no time dependence. (b) shows the 2nd Harmonic where there are ten apparent modes; two of which are potentially directly driven and 8 which are parametrically driven. The 8 potential parametric modes are potentially lower harmonics that are being parametrically driven.

Go to Contents

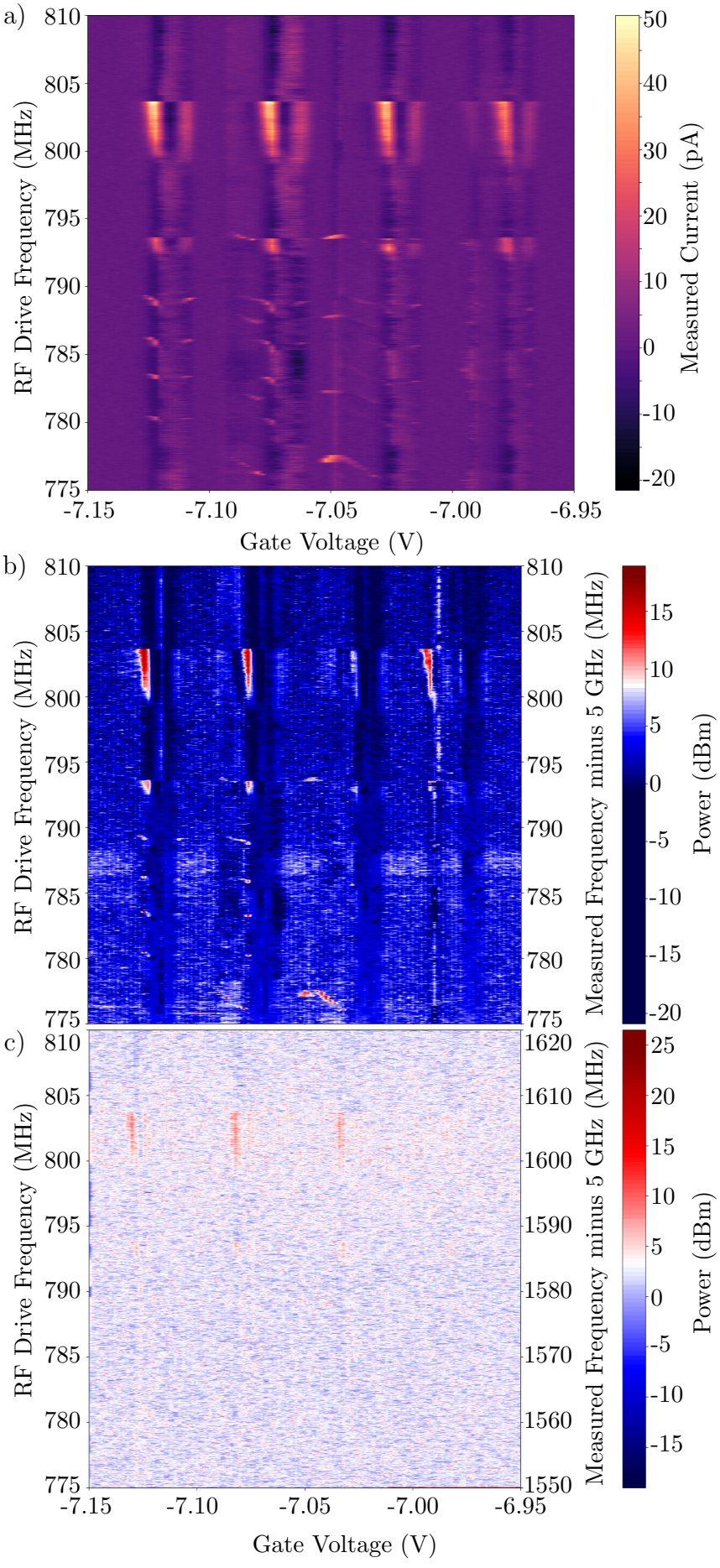

Figure 6.13

Frequency-Gate sweeps of the second harmonic using the rectification technique (a) and the electromechanical mixer technique (b,c) with the column average subtracted in order to remove the Coulomb peaks. The parameters used for all figures were a bias voltage of 9 mV, an RF drive power of −10 dBm, and a MW probe tone frequency of 5 GHz and power of −15 dBm. (a) shows ten resonances ranging from 775 to 810 MHz. The two brighter resonances at the top are likely directly driven resonances whereas the dimmer resonances below the directly driven resonances are likely parametric resonances. (b) shows the results from the electromechanical technique while scanning at around 5.7925 GHz. It shows eight resonances appearing around 5.7925 GHz. Two of the resonances seen in (a) do not appear in (b). (c) shows the results from the electromechanical technique while scanning at 6.585 GHz. It shows the component of the effective 2ω component as described in Equation 2.52 appearing.

Go to Contents

Ratio	Average
3:15	1.000034
4:16	1.000306
3:17	1.000174
4:18	1.000404

Table 6.6: Quadratic Curve Ratios of Figure 6.14. A ratio of 3:15 means a ratio of resonance 3 to resonance 15 using Equation 6.3. Ratio averages close to one indicate that the resonance is a parametric resonance of the fundamental frequency.

MHz and measuring around ∼5.2625 GHz. It shows two resonances at 259.2 MHz and 264.3 MHz which shows these two resonances are parametric driving of the fundamental. Figure 6.14 (b) shows the results from the electromechanical mixer technique while driving around ∼792.5 MHz and measuring around ∼ 5.525 GHz. It shows two resonances at 518 MHz and 528 MHz. The resonance at ∼ 5.525 GHz is the 2ω component of Equation 2.52.

Long range scans from 6.6585 GHz to 5 GHz were performed to try and find the other four resonances in Figure 6.13 (b) but unfortunately no resonances were found in this range. This could have been an issue with the spectrum analyser and the triggering system as such long scans had not been performed before.

Due to time constraints we were unable to perform output power vs drive power measurements like we did in Section 6.3. We can still however look at the quadratic curve ratios between resonances 15, 16, 17, and 18 compared to the fundamental resonances 3 and 4. The ratios of 3:15, 4:16, 3:17, and 4:18 are 0.0034%, 0.0306%, 0.0174%, and 0.0404% different from one respectively. As these ratios are very close to one these resonances could be parametric resonances of the fundamental as predicted by Svensson et al. [63]

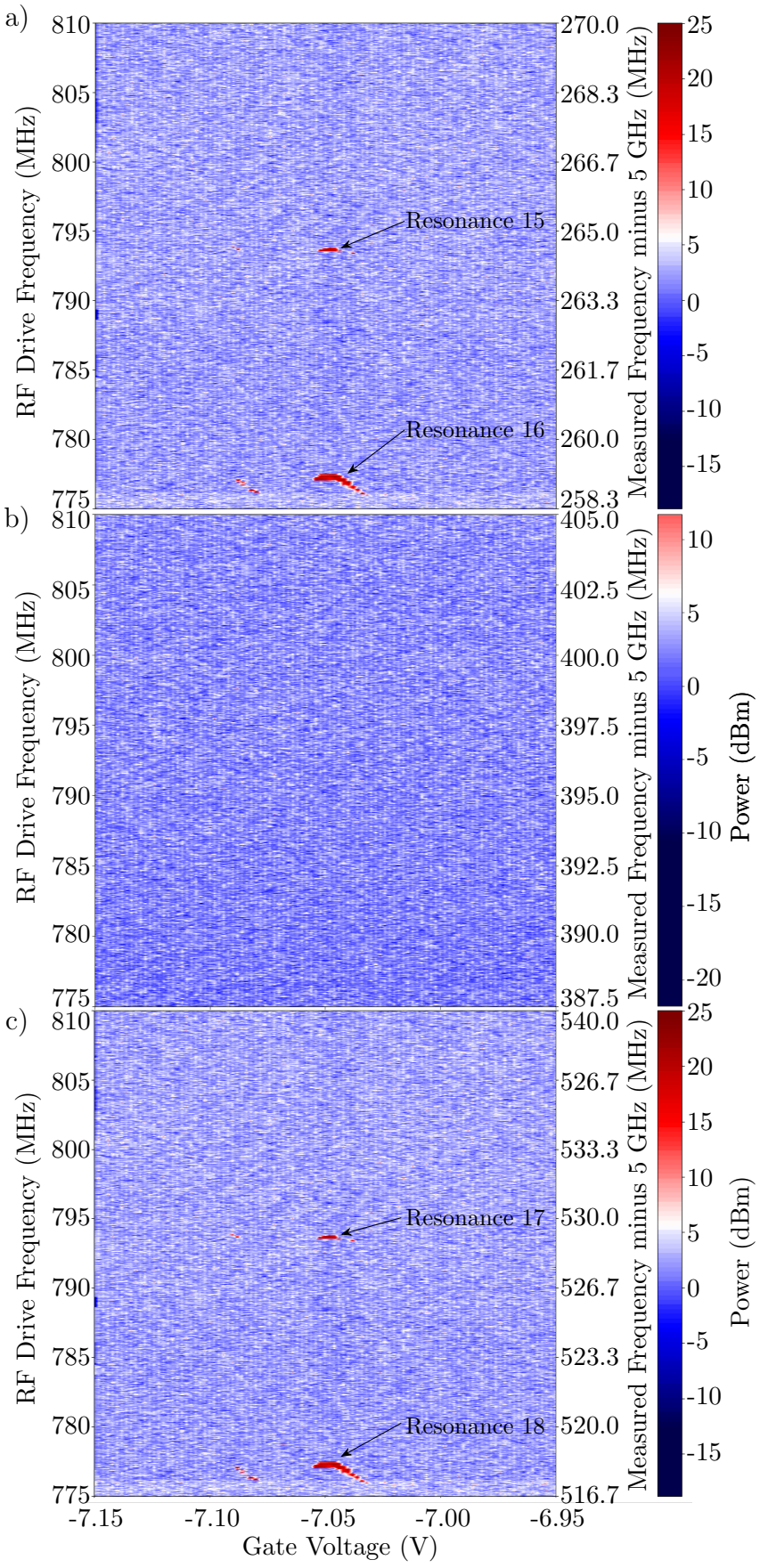

Frequency-Gate sweeps of the second harmonic using the electromechanical mixer technique with the column average subtracted in order to remove the Coulomb peaks. The parameters used for all figures were a bias voltage of 9 mV, an RF drive power of −10 dBm, and a MW probe tone frequency of 5 GHz and power of −15 dBm. (a) shows the results from scanning at 5.265 GHz while driving at 792.5 MHz. The resonance seen is parametric driving of the fundamental frequency. (b) shows the results from scanning at 5.3975 GHz while driving at 792.5 MHz. There are no resonances seen at this frequency. (c) shows the results from scanning at 5.530 GHz while driving at 792.5 MHz. The resonance seen is the 2ω component of the current as described in Equation 2.52 from the parametric driving of the fundamental frequency seen in (a).

Figure 6.14

Go to Contents

Chapter 7

Conclusion

In this thesis we have shown a new type of CNT resonator circuit that is capable of ultrasensitive time-dependent measurements. We have done this by using the non-linearity in a CNTs conductance to turn it into an up-converter mixer, this new technique is known as the electromechanical mixer technique. Mechanical signals are then amplified using a state-of-the-art near-quantum-limited amplifier, a TWPA, allowing for measurements that are more sensitive to CNT mechanical signals and measurements that have time dependence when compared to commonly used rectification techniques. Using this new technique in further research opens up the possibility of using a CNT resonator as a magnetic resonance force microscope (MRFM) by attaching a small piece of magnetic material to the CNT.

We have also shown that using the time dependence of this new technique we can perform resonance analysis on CNT mechanical resonances. CNTs are prone to parametric resonances due to their spring constant being highly dependent on the gate voltage [35]. Parametric resonances appear at harmonics of the CNT, and as such situations in the past where parametric resonances are mistaken for harmonics of the CNT have occurred [11]. This new technique is capable of distinguishing parametric from directly driven motion as we are able to scan at frequencies different from the drive frequency. By scanning at sub-harmonics of the drive frequency we can see parametric resonances of the fundamental frequency. In future research it could be possible to use this type of CNT device to make a tunable parametric amplifier similar to previously made cantilever CNT parametric amplifiers [13, 48].

This would be useful for dark matter detection which need tunable low-temperature amplifiers that function as expected in strong magnetic fields.

We can establish that the fundamental frequency of the CNT is around 260 MHz as this resonance has the best response to low drive powers and by scanning at half the drive frequency (plus 5 GHz) we see no other resonances. We see twin resonances at the fundamental which has been seen by others [60] which is due to the CNT having two degrees of freedom to oscillate in. The first harmonic of the CNT is around 525 MHz. By driving the CNT around 525 MHz we observe four resonances rather than the expected two. Using the electromechanical technique we are able to see where these extra two mechanical resonances from the CNT motion are coming from by using the time dependence of this technique. By driving the CNT at 525 MHz and measuring at half that (plus 5 GHz) we measure only two resonances. By comparing these two resonances to the fundamental, the ratio between them is exactly one implying they are the fundamental being parametrically driven. We can further distinguish parametrically driven from directly driven motion by looking at how the resonance peak reacts to different drive powers. The directly driven fundamental shows an almost linear response between output power and drive power. However the output power is slightly lower than expected because of two reasons. The first being that the CNT has a very high impedance causing a loss in MW power at the source electrode/CNT interface. The second is that at very high drive powers the nanotube can oscillate over the Coulomb peak creating an effective peak lower than the true height of the peak. The parametrically driven fundamental is not linear and instead shows a 'turn on' power around -34 dBm and then logarithmically increases in output power. This type of curve is characteristic of a parametric response. The output power for the parametric response is also slightly lower than expected and again this is probably due to the mismatch in impedance and Coulomb peak broadening. To address the high impedance of the CNT, we could in future fabricate the CNT device with a super-conducting impedance matching circuit which would couple to the CNT [64].

As well as the electromechanical mixer technique being useful for detecting parametric resonances it is also more sensitive than the rectification technique for detecting mechanical resonances. While looking at the same resonance in the rectification

method and the electromechanical technique, the resonance appears at −34 dBm in the rectification method but at −65 dBm in the electromechanical mixer technique. The electromechanical mixer technique has a caveat however as it depends on both the transconductance and the conductance of the device rather than just the transconductance. This results in more 'dead' areas when doing frequency vs gate voltage measurements than using the rectification technique. There is also a difference in where the mechanical resonances appear in the rectification technique compared to the electromechanical mixer technique. The rectification technique will be strongest at the peak and troughs of the Coulomb peaks whereas the electromechanical technique will be strongest on the sides of the Coulomb peaks.

The data recorded could have been more reliable if we didn't have to use a passive RF and active MW cancelling while doing measurements. Constantly changing parameters in the background of the measurements causes smears across data as explained in Appendix D ruining measurements, and slows down measurements by constantly changing parameters for each frequency/drive power point. In future this should be fixed by using a high pass filter to block RF leakage and a bandstop between the device and the TWPA to block the MW leakage.

At high drive powers the resonance peak was seen to split into two peaks. This has also been observed by others [32] when driving the CNT at high drive powers. It is likely that at high drive powers the nanotube behaves as a chaotic oscillator which results in random spikes. In Figure 6.2 (b) there are flat parts on the resonances which are probably resonances of the gate and drain gold electrodes which is then mixing in the TWPA with the 5 GHz probe tone. If the electrode resonances interact with the mechanical resonance of the CNT they cause the mechanical resonances to cover a large range of drive frequencies. The electrode resonances appear around $\sim$ 533 MHz (only in the rectification technique), $\sim$ 525 MHz, and $\sim$ 523 MHz. Electrode resonances interacting with the mechanical resonances has been seen in Changyao Chen et al. [65]. In future doing measurements over a larger gate voltage would make these electrode resonances clearer. The electrode resonances also seemed to depend on MW power so reducing the MW power and increasing the RF power would hopefully show parametric excitation more clearly.

Go to Contents

It was expected that the quadratic curve ratios of the first harmonic to the fundamental would both lie above one as the bending rigidity of the carbon nanotube should cause harmonics of the CNT to have frequencies slightly larger than integer multiples of the fundamental. However the quadratic curve ratio of resonance 6 and 10 compared to the resonance 1 and 3 respectively are less than one. This means that the resonance occurring perpendicular to the substrate has not doubled in frequency.

There are resonances around the second harmonic that were not explained. Figure 6.13 (a) and (b) show ten and eight resonances respectively. Using the new electromechanical mixer technique, we performed resonance analysis on the resonances seen. It showed a pair of resonances from the fundamental being driven by a drive frequency at three times the fundamental frequency. From literature, we should expect parametric driving of the fundamental at $2\omega_0/n$ not at $3\omega_0$. Further study needs to be done in order to confirm these resonances are parametric by doing output power vs drive power scans as performed on the first harmonic, and further study into theory. The other resonances seen around the second harmonic were not explained. We attempted to find out where these were coming from doing a long range scan however the results were unclear showing resonances that didn't have any dependence on gate voltage nor where we expected them to be. The results could have been an problem with the spectrum analyser as this length of scan hadn't been performed before causing it to read an overload value or an issue with the trigger source being triggered too often. Looking for bugs in the spectrum analyser driver could help prevent this.

Go to Contents

Appendices

Appendix A

RF Phase Shifter Characteristics

The phase shifter used in the RF cancelling circuit was a custom phase shifter made by Edward Laird's student, G Yin, from Oxford University. The design is similar to the one found in this paper [66]. In Figure A.1, the characteristics of the phase shifter are shown.

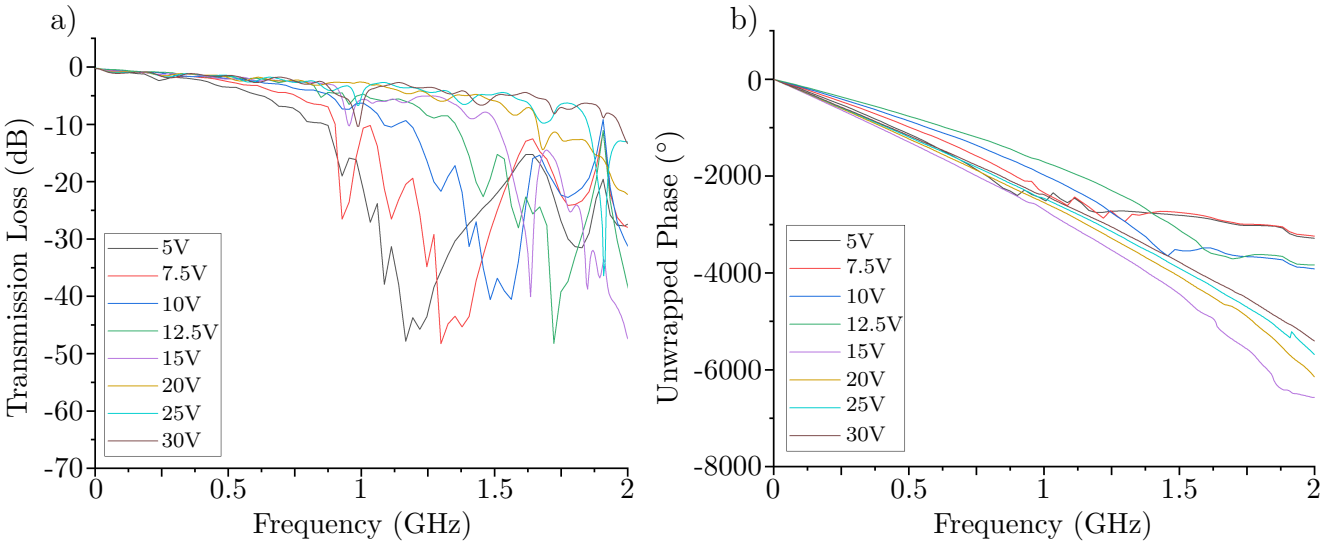

Figure A.1: a) Transmission and (b) Phase of a Matt Greens Phase Shifter at different voltages from 5 V to 30 V. This phase shifter is part of the RF cancellation circuit and was made by Edward Laird's student while at Oxford University. As the voltage is increased the transmission loss of the device decreases as the frequency is increased. The phase shifter is still able to change the phase at a large range of frequencies. A voltage of 20 V was generally used for the RF cancelling due to little transmission loss at higher frequencies.

Appendix B

MW Power Sweeps

Figure B.1 shows the effect the MW probe tone power had on the mechanical resonance while using the rectification technique. At a MW power of ~ -22 dBm, the background noise increases as either the Coulomb peak widens or the CNT starts to warm due to excess power entering the CNT.

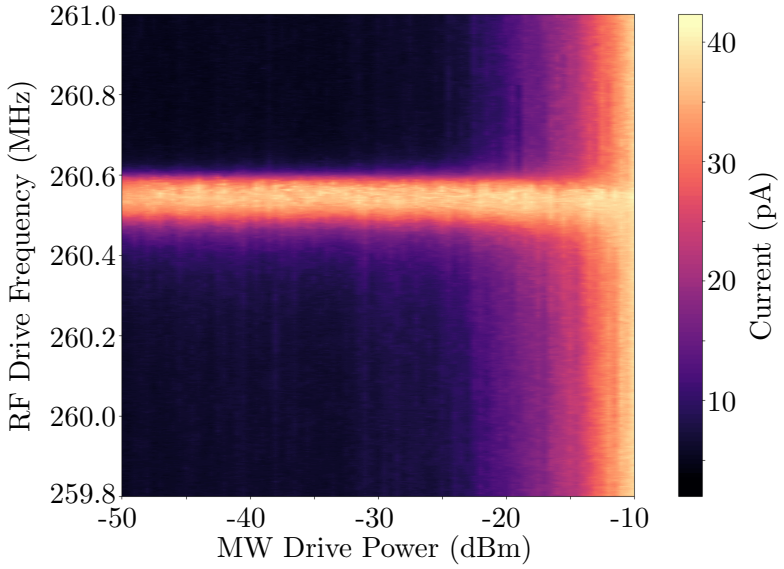

Figure B.1: Testing the MW power in the dc. At a MW power of ~ -22 dBm the background noise increases as the Coulomb peak widens and possibly as the CNT starts to warm slightly.

Appendix C

Narda Amplifier Cooler

The Narda low noise amplifier (LNA) is a +36 dB amplifier, however the gain has been observed to vary with temperature - decreasing as temperature increases, and vice versa. The experimental setup to show this uses a Keysight P9375A VNA to measure the S_{21} transmission. To measure the device temperature, an LM35 Temperature Sensor was clamped to the pre-existing (but insufficient) heat sink, and the output voltage from this was measured using a digital multimeter (DMM).

With no stabilisation, the device rose to a maximum temperature of around 56°C, with around 2°C of periodic fluctuation due to the air conditioning in the room. This is shown in Figure C.1. The high temperature resulted in a gain reduction at 8 GHz from +35.4 dB to $+34.10 \pm 0.133$ dB, so clearly some apparatus to reduce the internal heating was necessary.

Figure C.2 shows the gain from the amplifier with the cooler attached. The gain from the amplifier has been improved at the gain at 8 GHz has gone from +34.10 dB without the cooler to +35.36 dBm with the cooler. The deviation in gain from the amplifier has decreases as well as deviation in the gain at 8 GHz has gone from

	Heatsink Range(°C)	Heatsink Temperature Range (°C)	S21 @ 8GHz (dB)	S21 Range @ 8GHz (dB)
No Cooling	54.7 - 57.8	3.1	34.10 ± 0.133	1.436
With Cooler	27.9 - 28.4	0.5	35.36 ± 0.009	0.043

Table C.1: The temperature range and gain of the Narda amplifier with and without a cooler attached.

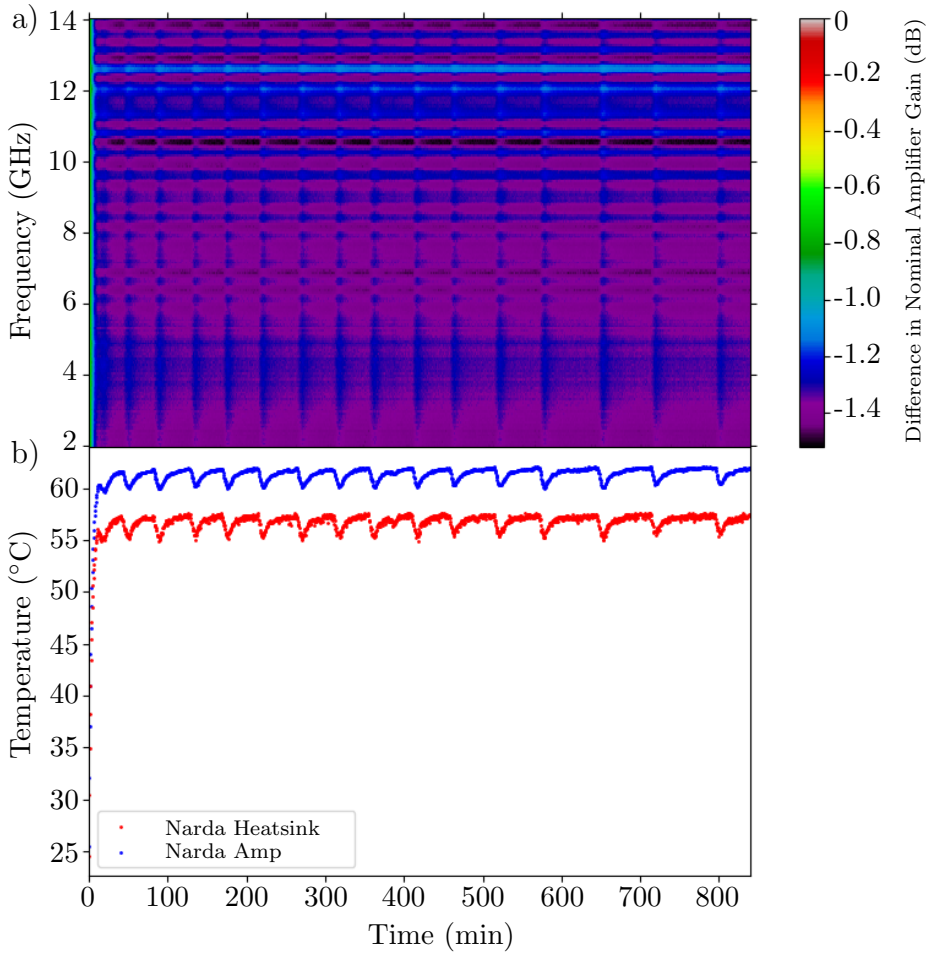

Figure C.1: (a) The change in gain of the Narda from its nominal gain of +35.4 dB without the cooler over 15 hours. The gain from the amplifier is decreased by $\sim$ 1.3 dB and has a $\pm$0.133 dB variation. (b) The temperate of the Narda and heatsink over 15 hours. The temperature range of the heatsink is 54.7°C – 57.8°C.

Go to Contents

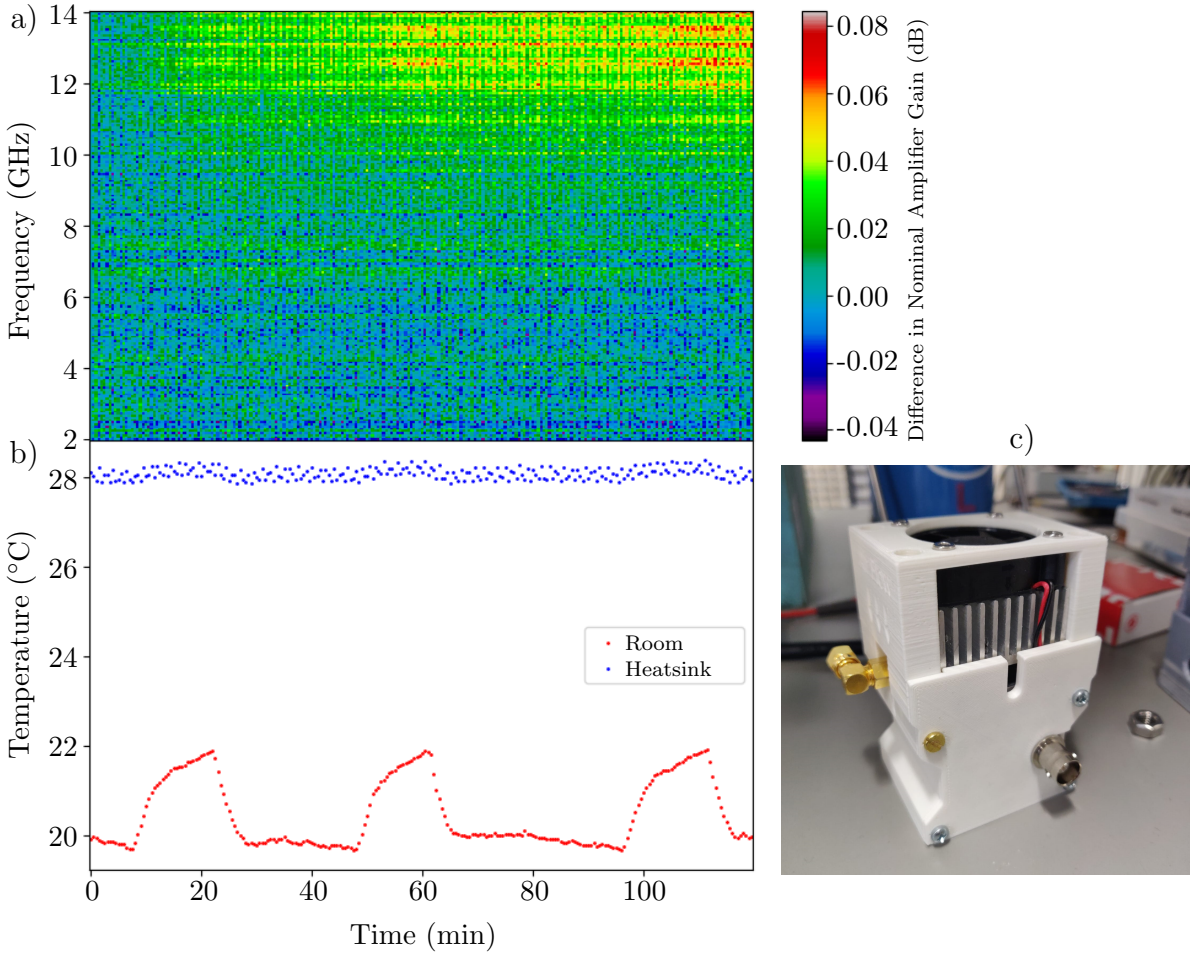

Figure C.2: (a) The change in gain of the Narda from its nominal gain of +35.4 dB with the cooler over 2 hours. The gain from the amplifier is 35.36 ± 0.009 dB. (b) The temperate of the Narda and heatsink attached to the Narda over 2 hours. The temperature range of the heatsink is $27.9°C - 28.4°C$. (c) The cooler assembly compromising of a fan, heatsink, PCB, and the Narda amp.

Go to Contents

0.133 dB without the cooler to 0.009 dB with the cooler. The improvement in gain is due to the Narda amplifier being significantly cooler going from $\sim 56.25°C$ without the cooler to $\sim 28.15°C$ with the cooler. The improvement in the deviation of the gain is due to the improvement in the stability of the temperature of the amplifier. The temperature range of the Narda amplifier without the cooler was $3.1°C$ whereas with the cooler the temperature range was $0.5°C$.

The schematic and CAD files for the cooler are available here.

Go to Contents

Appendix D

RF & MW Cancellation

The RF and MW cancellation were an active process during measurements performed in this thesis and as such a reader may have questions as to how much the results were affected by such processes.

The RF cancellation worked off calibration data taken before the measurements were performed. The calibration data was created by firstly deciding on a drive frequency range and RF drive power to be used in the measurement. The Rohde & Schwarz SMBV100A signal generator which sequentially produces those drive frequencies at the decided RF drive power while the RF leakage through the device is measured in the Rohde & Schwarz FSV3044 spectrum analyser. Using the Vaunix LDA-102 digital attenuator and our custom RF phase shifter for each RF drive frequency, the attenuator and phase shifter are tweaked to minimise the RF leakage as much as possible. These values are then saved to a database where they are called upon during the measurement.

The MW cancellation was a more active process than the RF cancellation. In theory, once the phase shifter and amplifiers in this circuit were set, as the frequency and power of the MW probe doesn't change, it shouldn't needed to be tweaked. Unfortunately, as described earlier in the Chapter 5 due to the air conditioning in that room and the Telfon knee of the cables used, the phase of the cancelling signal would change. Attempts at making this signal more stable were made by replacing the cables with TP220 temperature phase stable cables and encasing equipment in

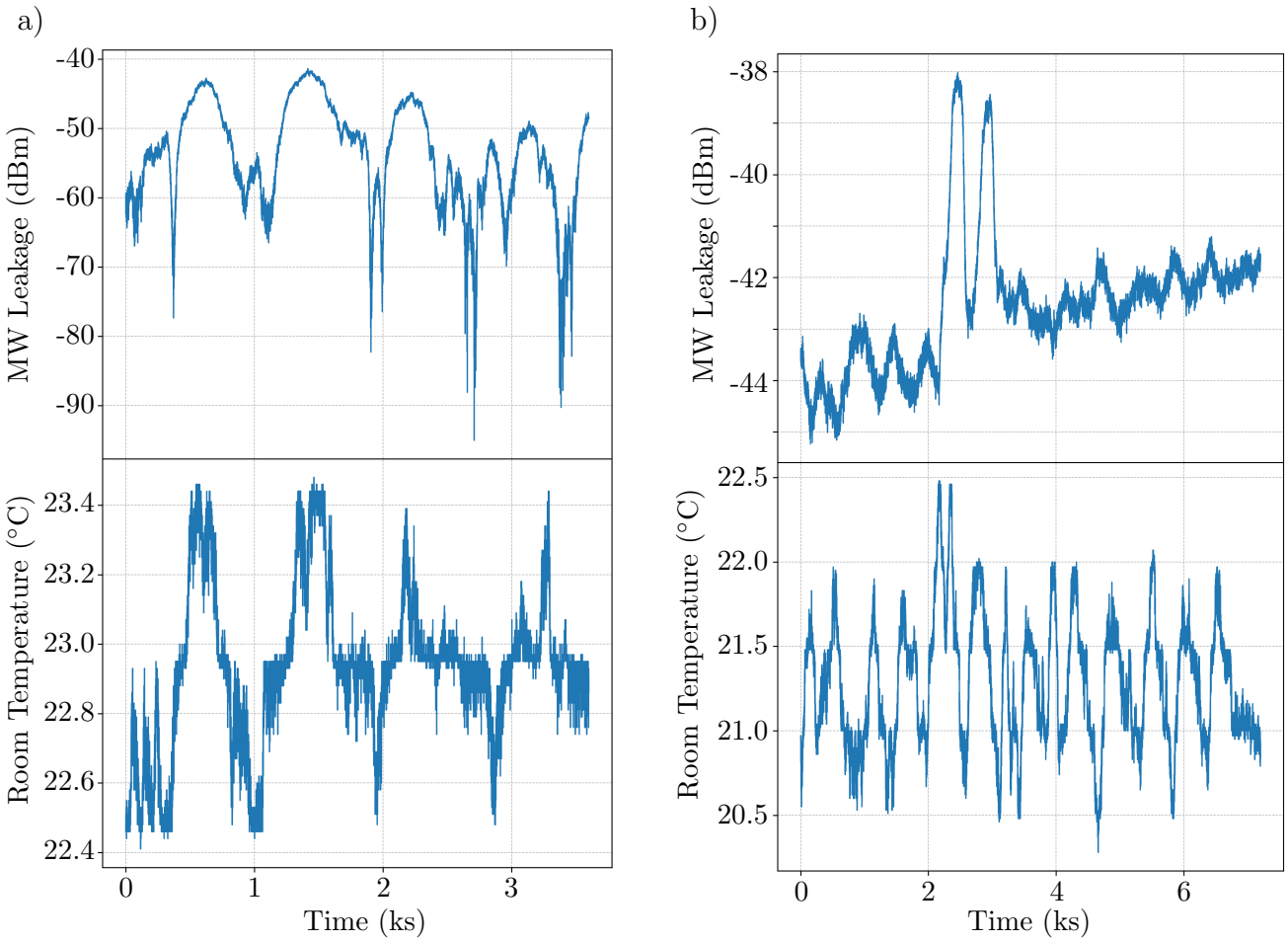

Figure D.1: (a) The MW leakage through the device without any phase stable cables or insulation. The peaks and troughs in the MW leakage match with the fluctuations in the room temperature. (b) The MW leakage through the device with phase stable cables and insulation. The range of the MW leakage has been significantly reduced, but there is still some dependence on the room temperature.

insulation. However, as some components in the circuit such as 90° bends or splitters couldn't be replaced nor insulated, the circuit was still subjected to temperature fluctuations.

Therefore to deal with these small fluctuations, a script was designed in Python that would measure the MW probe tone leakage using a Rigol DSA875 spectrum analyser, and then tweaks the phase shifter and attenuator to find the minimum MW leakage.

The RF leakage was usually lower than −80 dBm. The MW leakage was usually kept below −70 dBm except in extenuating circumstances as the script was designed to keep the MW leakage below −70 dBm. As the RF leakage was always calibrated be-

fore any measurement, only the MW leakage could go above the −70 dBm level. At about −50 dBm the signals would mix to raise the noise floor in the measurements. Resonances in the measurements are not likely of being these mixed signals due to timings. Measurement sweeps would typically take < 50 ms per point whereas shifts in the MW leakage power typically take ~ 500 ms. Therefore if we were seeing fake resonances from the mixing of the RF and MW leakage they would appear as long streaks in the sweep direction in the measurement. As we do not see these, then what we are seeing must be the electromechanical motion of the CNT.

Go to Contents

Bibliography

[1] L. J. E. Hofer, E. Sterling, and J. T. McCartney. "Structure of Carbon Deposited from Carbon Monoxide on Iron, Cobalt and Nickel". In: *The Journal of Physical Chemistry* 59.11 (1955), pp. 1153–1155. DOI: 10.1021/j150533a010. eprint: https://doi.org/10.1021/j150533a010. URL: https://doi.org/10.1021/j150533a010.

[2] Sumio Iijima. "Helical microtubules of graphitic carbon". In: *Nature* 354 (1991), pp. 56–58. URL: https://api.semanticscholar.org/CorpusID:4302490.

[3] Michael Tiza et al. "Applications of nanomaterials in highway pavements". In: *NanoEra* (Dec. 2022).

[4] Laura P. Zanello et al. "Bone Cell Proliferation on Carbon Nanotubes". In: *Nano Letters* 6.3 (2006), pp. 562–567. DOI: 10.1021/nl051861e. eprint: https://doi.org/10.1021/nl051861e. URL: https://doi.org/10.1021/nl051861e.

[5] Antonio J. Paleo et al. "Carbon Nanotube–Polyurethane Composite Sheets for Flexible Thermoelectric Materials". In: *ACS Applied Nano Materials* 6.19 (2023), pp. 17986–17995. DOI: 10.1021/acsanm.3c03247. eprint: https://doi.org/10.1021/acsanm.3c03247. URL: https://doi.org/10.1021/acsanm.3c03247.

[6] Giovanni Valenti et al. "Co-axial heterostructures integrating palladium/titanium dioxide with carbon nanotubes for efficient electrocatalytic hydrogen evolution". In: *Nature Communications* 7 (Dec. 2016), p. 13549. URL: https://www.proquest.com/scholarly-journals/co-axial-heterostructures-integrating-palladium/docview/1847872979/se-2.

[7] Mukul Kumar and Yoshinori Ando. "Chemical Vapor Deposition of Carbon Nanotubes: A Review on Growth Mechanism and Mass Production". In: *Journal of nanoscience and nanotechnology* 10 (June 2010), pp. 3739–58. DOI: 10.1166/jnn.2010.2939.

[8] Menno Poot and Herre S.J. van der Zant. "Mechanical systems in the quantum regime". In: *Physics Reports* 511.5 (2012), pp. 273–335. DOI: https://doi.org/10.1016/j.physrep.2011.12.004. URL: https://www.sciencedirect.com/science/article/pii/S0370157311003644.

[9] Yutian Wen et al. "Measuring carbon nanotube vibrations using a single-electron transistor as a fast linear amplifier". In: *Applied Physics Letters* 113 (Oct. 2018), p. 153101. DOI: 10.1063/1.5052185.

[10] AK Hüttel et al. "Nanoelectromechanics of suspended carbon nanotubes". In: *New Journal of Physics* 10.9 (2008), p. 095003.

[11] Edward Laird et al. "A High Quality Factor Carbon Nanotube Mechanical Resonator at 39 GHz". In: *Nano letters* 12 (Nov. 2011), pp. 193–7. DOI: 10.1021/nl203279v.

[12] Adrian Bachtold, Joel Moser, and M. Dykman. "Mesoscopic physics of nanomechanical systems". In: *Rev. Mod. Phys.* (Feb. 2022). DOI: 10.48550/arXiv.2202.01819.

[13] Alexander Eichler et al. "Parametric amplification and self-oscillation in a nanotube mechanical resonator". In: *Nano letters* 11.7 (2011), pp. 2699–2703.

[14] Michael Faraday. "On a peculiar class of acoustical figures; and on certain forms assumed by groups of particles upon vibrating elastic surfaces". In: *Abstracts of the Papers Printed in the Philosophical Transactions of the Royal Society of London*. 3. The Royal Society London. 1837, pp. 49–51.

[15] RB Karabalin, SC Masmanidis, and ML Roukes. "Efficient parametric amplification in high and very high frequency piezoelectric nanoelectromechanical systems". In: *Applied Physics Letters* 97.18 (2010).

[16] Antonio Maffucci and Giovanni Miano. "Electrical Properties of Graphene for Interconnect Applications". In: *Applied Sciences* 4 (May 2014), pp. 305–317. DOI: 10.3390/app4020305.

Go to Contents

[17] Abraao C. Torres-Dias et al. "From mesoscale to nanoscale mechanics in single-wall carbon nanotubes". In: *Carbon* 123 (2017), pp. 145–150. DOI: https://doi.org/10.1016/j.carbon.2017.07.036. URL: https://www.sciencedirect.com/science/article/pii/S0008622317307194.

[18] S. Rathinavel, K. Priyadharshini, and Dhananjaya Panda. "A review on carbon nanotube: An overview of synthesis, properties, functionalization, characterization, and the application". In: *Materials Science and Engineering: B* 268 (2021), p. 115095. DOI: https://doi.org/10.1016/j.mseb.2021.115095. URL: https://www.sciencedirect.com/science/article/pii/S0921510721000556.

[19] Aravind Vijayaraghavan John E. Proctor Daniel Melendrez Armada. *An Introduction to Graphene and Carbon Nanotubes*. Boca Raton: CRC Press, 2017. DOI: 10.1201/9781315368191.

[20] Edward A. Laird et al. "Quantum transport in carbon nanotubes". In: *Reviews of Modern Physics* 87.3 (July 2015), pp. 703–764. DOI: 10.1103/revmodphys.87.703. URL: http://dx.doi.org/10.1103/RevModPhys.87.703.

[21] Noriaki Hamada, Shin-ichi Sawada, and Atsushi Oshiyama. "New one-dimensional conductors: Graphitic microtubules". In: *Phys. Rev. Lett.* 68 (10 Mar. 1992), pp. 1579–1581. DOI: 10.1103/PhysRevLett.68.1579. URL: https://link.aps.org/doi/10.1103/PhysRevLett.68.1579.

[22] Xinjian Zhou et al. "Band Structure, Phonon Scattering, and the Performance Limit of Single-Walled Carbon Nanotube Transistors". In: *Phys. Rev. Lett.* 95 (14 Sept. 2005), p. 146805. DOI: 10.1103/PhysRevLett.95.146805. URL: https://link.aps.org/doi/10.1103/PhysRevLett.95.146805.

[23] Pablo Jarillo-Herrero et al. "Electron-hole symmetry in a semiconducting carbon nanotube quantum dot". In: *Nature* (May 2004), pp. 389–392. DOI: 10.1038/nature02568. URL: http://dx.doi.org/10.1038/nature02568.

[24] Karim El Shabrawy et al. "Modeling SWCNT Bandgap and Effective Mass Variation Using a Monte Carlo Approach". In: *IEEE Transactions on Nanotechnology* 9.2 (2010), pp. 184–193. DOI: 10.1109/TNANO.2009.2028343.

[25] Ji Ung Lee. "Quasi-ballistic transport model for nanoscale MOSFETs: learnings from a diffusive conductor". In: *Japanese Journal of Applied Physics* 60.4

Go to Contents

(Mar. 2021), p. 044001. DOI: 10.35848/1347-4065/abeabd. URL: https://dx.doi.org/10.35848/1347-4065/abeabd.

[26] M. Büttiker. "Quantized transmission of a saddle-point constriction". In: *Phys. Rev. B* 41 (11 Apr. 1990), pp. 7906–7909. DOI: 10.1103/PhysRevB.41.7906. URL: https://link.aps.org/doi/10.1103/PhysRevB.41.7906.

[27] Antti-Pekka Jauho Hartmut Haug. *Quantum Kinetics in Transport and Optics of Semiconductors*. Springer Berlin, Heidelberg, 2008. DOI: 10.1007/978-3-540-73564-9.

[28] Kenji Natori. "Ballistic/quasi-ballistic transport in nanoscale transistor". In: *Applied Surface Science* 254.19 (2008), pp. 6194–6198. DOI: https://doi.org/10.1016/j.apsusc.2008.02.150. URL: https://www.sciencedirect.com/science/article/pii/S0169433208004698.

[29] L P Kouwenhoven, D G Austing, and S Tarucha. "Few-electron quantum dots". In: *Reports on Progress in Physics* 64.6 (June 2001), p. 701. DOI: 10.1088/0034-4885/64/6/201. URL: https://dx.doi.org/10.1088/0034-4885/64/6/201.

[30] R. Hanson et al. "Spins in few-electron quantum dots". In: *Reviews of Modern Physics* 79.4 (Oct. 2007), pp. 1217–1265. DOI: 10.1103/revmodphys.79.1217. URL: http://dx.doi.org/10.1103/RevModPhys.79.1217.

[31] A K Hüttel et al. "Nanoelectromechanics of suspended carbon nanotubes". In: *New Journal of Physics* 10.9 (Sept. 2008), p. 095003. DOI: 10.1088/1367-2630/10/9/095003. URL: https://dx.doi.org/10.1088/1367-2630/10/9/095003.

[32] Gary A Steele et al. "Strong coupling between single-electron tunneling and nanomechanical motion". In: *Science* 325.5944 (2009), pp. 1103–1107.

[33] Benjamin Lassagne et al. "Coupling mechanics to charge transport in carbon nanotube mechanical resonators". In: *Science* 325.5944 (2009), pp. 1107–1110. DOI: 10.1126/science.1174290.

[34] Marc Dequesnes, S V Rotkin, and N R Aluru. "Calculation of pull-in voltages for carbon-nanotube-based nanoelectromechanical switches". In: *Nanotechnology* 13.1 (Jan. 2002), p. 120. DOI: 10.1088/0957-4484/13/1/325. URL: https://dx.doi.org/10.1088/0957-4484/13/1/325.

Go to Contents

[35] HB Meerwaldt, Gary A Steele, and Herre SJ van der Zant. "Carbon nanotubes: Nonlinear high-Q resonators with strong coupling to single-electron tunneling". In: *Fluctuating Nonlinear Oscillators: From Nanomechanics to Quantum Superconducting Circuits* (2012), pp. 312–340.

[36] J. Moser et al. "Nanotube mechanical resonators with quality factors of up to 5 million". In: *Nature Nanotechnology* 9.12 (Oct. 2014), pp. 1007–1011. DOI: 10.1038/nnano.2014.234. URL: http://dx.doi.org/10.1038/nnano.2014.234.

[37] Ch. Laurent, E. Flahaut, and A. Peigney. "The weight and density of carbon nanotubes versus the number of walls and diameter". In: *Carbon* 48.10 (2010), pp. 2994–2996. DOI: https://doi.org/10.1016/j.carbon.2010.04.010. URL: https://www.sciencedirect.com/science/article/pii/S0008622310002617.

[38] Mukul Kumar and Yoshinori Ando. "Chemical Vapor Deposition of Carbon Nanotubes: A Review on Growth Mechanism and Mass Production". In: *Journal of nanoscience and nanotechnology* 10 (June 2010), pp. 3739–58. DOI: 10.1166/jnn.2010.2939.

[39] Ron Lifshitz and Michael C Cross. "Nonlinear dynamics of nanomechanical and micromechanical resonators". In: *Reviews of nonlinear dynamics and complexity* 1.1 (2008), pp. 1–52.

[40] Patrick Steger. "Towards a magnet-on-cantilever type Carbon Nanotube Force Sensor for Magnetic Resonance Force Microscopy". PhD thesis. Lancaster University, 2025. DOI: 10.17635/lancaster/thesis/2804.

[41] A. Eichler et al. "Symmetry breaking in a mechanical resonator made from a carbon nanotube". In: *Nature Communications* 4.1 (Nov. 2013). DOI: 10.1038/ncomms3843. URL: http://dx.doi.org/10.1038/ncomms3843.

[42] N. Hüttner et al. "Optomechanical Coupling and Damping of a Carbon Nanotube Quantum Dot". In: *Phys. Rev. Appl.* 20 (6 Dec. 2023), p. 064019. DOI: 10.1103/PhysRevApplied.20.064019. URL: https://link.aps.org/doi/10.1103/PhysRevApplied.20.064019.

[43] Andreas K Huttel et al. "Carbon nanotubes as ultrahigh quality factor mechanical resonators". In: *Nano letters* 9.7 (2009), pp. 2547–2552.

Go to Contents

[44] Alexander Eichler and Oded Zilberberg. *Classical and quantum parametric phenomena*. Oxford University Press, 2023.

[45] William B Case. "The pumping of a swing from the standing position". In: *American Journal of Physics* 64.3 (1996), pp. 215–219.

[46] Michael Fowler. *Classical Mechanics, Lecture 20.1: Introduction to parametric resonance*. Physics LibreTexts, 2024. URL: https://phys.libretexts.org/Bookshelves/Classical_Mechanics/Graduate_Classical_Mechanics_(Fowler)/20%3A_Parametric_Resonance/20.01%3A_Introduction_to_Parametric_Resonance.

[47] D. Rugar and P. Grütter. "Mechanical parametric amplification and thermomechanical noise squeezing". In: *Physical Review Letters* 67.6 (1991), pp. 699–702. DOI: 10.1103/PhysRevLett.67.699.

[48] BJ Alemán et al. "A carbon nanotube-based NEMS parametric amplifier for enhanced radio wave detection and electronic signal amplification". In: *Journal of Physics: Conference Series*. Vol. 302. 1. IOP Publishing. 2011, p. 012001.

[49] Chung Chiang Wu, Chang Hua Liu, and Zhaohui Zhong. "One-step direct transfer of pristine single-walled carbon nanotubes for functional nanoelectronics". In: *Nano letters* 10.3 (2010), pp. 1032–1036.

[50] Jonah Waissman et al. "Realization of pristine and locally tunable one-dimensional electron systems in carbon nanotubes". In: *Nature Nanotechnology* 8.8 (2013), pp. 569–574. DOI: 10.1038/nnano.2013.143.

[51] Stefan Blien et al. "Quartz Tuning-Fork Based Carbon Nanotube Transfer into Quantum Device Geometries". In: *physica status solidi (b)* 255 (2018). URL: https://api.semanticscholar.org/CorpusID:4826722.

[52] Deepanjan Das. "Exploiting quantum paraelectricity for advancing cryogenic quantum measurements". PhD thesis. Lancaster University, 2025.

[53] Sebastian Krinner et al. "Engineering cryogenic setups for 100-qubit scale superconducting circuit systems". In: *EPJ Quantum Technology* 6.1 (2019), p. 2.

[54] Visa Vesterinen et al. "A Josephson traveling wave parametric amplifier featuring superconducting nonlinear asymmetric inductive elements". In: *A Joseph-*

son traveling wave parametric amplifier featuring superconducting nonlinear asymmetric inductive elements. Mar. 2021. URL: https://march.aps.org/.

[55] N. E. Frattini et al. "3-wave mixing Josephson dipole element". In: *Applied Physics Letters* 110.22 (May 2017). DOI: 10.1063/1.4984142. URL: http://dx.doi.org/10.1063/1.4984142.

[56] Vera Sazonova et al. "A tunable carbon nanotube electromechanical oscillator". In: *Nature* 431.7006 (2004), pp. 284–287.

[57] B. Witkamp et al. "Self-detecting gate-tunable nanotube paddle resonators". In: *Applied Physics Letters* 93.11 (Sept. 2008). DOI: 10.1063/1.2985859. URL: http://dx.doi.org/10.1063/1.2985859.

[58] G. Yin, G. A. D. Briggs, and E. A. Laird. *A wide-band tunable phase shifter for radio-frequency reflectometry*. 2014. URL: https://arxiv.org/abs/1412.4200.

[59] Pham Cao Dai et al. "High Resolution Phase Shifter, Attenuator Based on Combination of Coupler and Digital Step Attenuator in 3.4-4.2GHz Frequency Range". In: *2019 3rd International Conference on Recent Advances in Signal Processing, Telecommunications Computing (SigTelCom)*. 2019, pp. 145–148. DOI: 10.1109/SIGTELCOM.2019.8696127.

[60] J. Moser et al. "Ultrasensitive force detection with a nanotube mechanical resonator". In: *Nature Nanotechnology* 8.7 (June 2013), pp. 493–496. DOI: 10.1038/nnano.2013.97. URL: http://dx.doi.org/10.1038/nnano.2013.97.

[61] A Eichler et al. "Strong coupling between mechanical modes in a nanotube resonator". In: *Physical review letters* 109.2 (2012), p. 025503.

[62] Yaxing Zhang et al. "Time-translation-symmetry breaking in a driven oscillator: From the quantum coherent to the incoherent regime". In: *Physical Review A* 96.5 (2017), p. 052124. DOI: 10.1103/PhysRevA.96.052124.

[63] Ida-Maria Svensson et al. "Period multiplication in a parametrically driven superconducting resonator". In: *Applied Physics Letters* 113.2 (2018), p. 022602. DOI: 10.1063/1.5026974.

[64] Vishal Ranjan et al. "Clean carbon nanotubes coupled to superconducting impedance-matching circuits". In: *Nature communications* 6.1 (2015), p. 7165.

Go to Contents

[65] Changyao Chen et al. "Performance of monolayer graphene nanomechanical resonators with electrical readout". In: *Nature nanotechnology* 4.12 (2009), pp. 861–867.

[66] G. Yin, G. A. D. Briggs, and E. A. Laird. *A wide-band tunable phase shifter for radio-frequency reflectometry*. 2014. arXiv: 1412.4200 [physics.ins-det]. URL: https://arxiv.org/abs/1412.4200.

Go to Contents